Copyright Undertaking

URBAN NAVIGATION USING 3D MAPPING-AIDED (3DMA) GNSS

HOI FUNG NG

PhD

The Hong Kong Polytechnic University

2025

The Hong Kong Polytechnic University

Department of Aeronautical and Aviation Engineering

Urban Navigation Using 3D Mapping-Aided (3DMA) GNSS

Hoi Fung NG

A thesis submitted in partial fulfilment of the
requirements for the degree of Doctor of Philosophy

Aug 2024

CERTIFICATE OF ORIGINALITY

I hereby declare that this thesis is my own work and that, to the best of my knowledge and belief, it reproduces no material previously published or written, nor material that has been accepted for the award of any other degree or diploma, except where due acknowledgement has been made in the text.

____________________________ (Signed)

NG Hoi Fung (Name of student)

Abstract

Localization and navigation rely on a global navigation satellite system (GNSS) to provide an absolute position. However, signal reflection and attenuation result in positioning performance degradation, which is common in urban canyons. Urban localization can be enhanced using the resources associated with 3D building models. Different 3D mapping-aided (3DMA) GNSS algorithms have been proposed, in which the 3D building models are used to aid the positioning. Recently, the candidate-based 3DMA GNSS framework was presented to examine the distributed particles, and the particles that best match the observed measurements, that is, the particles with the minimum cost, are identified as the receiver location. Such particle sampling approaches are inexpensive but incur a high computational load. Besides, the candidate-based 3DMA GNSS cannot provide reliable solutions for continuous positioning.

This study develops a novel 3DMA GNSS positioning framework for urban positioning. Based on the existing candidate-based 3DMA GNSS, the candidates are distributed effectively with a context-based algorithm. Furthermore, this study harnesses the benefits brought by the complementary nature of the different 3DMA GNSS algorithms and provides an integrated solution to maximize positioning performance. The third contribution of this study is to increase the robustness of the positioning by connecting multi-epoch solutions. This study achieves this by mathematically expressing the candidate-based 3DMA GNSS. The mathematically expressed model is then tightly integrated with Doppler measurements using factor graph optimization (FGO).

Designed experiments are conducted to validate the performance of the proposed positioning framework. The evaluation shows that the proposed positioning framework outperforms the conventional positioning methods. The proposed framework can provide accurate and reliable positioning for smartphones and consumer-grade GNSS receivers in urban canyons.

Publications and Activities Arising from the Thesis

There are 11 journal papers, 14 conference papers, and 1 book chapter authored or co-authored during his study. The following publications are directly related to this thesis:

Journal Papers

1. **Ng, H.-F.**, Zhong, Q., Groves, Paul, & Hsu, L.-T. (2024). Grid-based 3DMA GNSS with Clustering and Doppler Velocity using Factor Graph Optimisation. *NAVIGATION*. (Under review).

2. **Ng, H.-F.**, Zhang, G,& Hsu, L.-T.. (2023). Multi-Epoch Kriging-Based 3D Mapping-Aided GNSS and Doppler Measurement Fusion using Factor Graph Optimization. *NAVIGATION: Journal of the Institute of Navigation*, 70(4), navi.617. `https://doi.org/10.33012/navi.617`.

3. Hsu, L. T., Huang, F., **Ng, H.-F.**, Zhang, G., Zhong, Y., Bai, X., & Wen, W. (2023). Hong Kong UrbanNav: An Open-Source Multisensory Dataset for Benchmarking Urban Navigation Algorithms. *NAVIGATION: Journal of the Institute of Navigation*, 70(4), navi.602. `https://doi.org/10.330`

12/navi.602.

4. **Ng, H.-F.**, Hsu, L.-T., Lee, M. J. L., Feng, J., Naeimi, T., Beheshti, M., & Rizzo, J.-R. (2022). Real-Time Loosely Coupled 3DMA GNSS/Doppler Measurements Integration Using a Graph Optimization and Its Performance Assessments in Urban Canyons of New York. *Sensors*, 22(17), 6533. `https://doi.org/10.3390/s22176533`.

5. **Ng, H.-F.**, Zhang, G., Luo, Y., & Hsu, L.-T. (2021). Urban positioning: 3D mapping-aided GNSS using dual-frequency pseudorange measurements from smartphones. *NAVIGATION, Journal of the Institute of Navigation*, 68(4), 727-749. `https://doi.org/10.1002/navi.448`.

Conference Papers

1. **Ng, H.-F.**. (2022). Multi-Epoch Kriging-Based 3D Mapping Aided GNSS using Factor Graph Optimization. *Proceedings of the 35th International Technical Meeting of the Satellite Division of The Institute of Navigation (ION GNSS+ 2022)*, Denver, Colorado, 1706-1720. `https://doi.org/10.33012/2022.18497`. **(Student Paper Award in ION GNSS+ 2022). (Presenter)**.

2. **Ng, H.-F.**, Hsu, L.-T., Lee, M. J. L., Feng, J., Naeimi, T., Beheshti, M., & Rizzo, J.-R. (2022). Real-time State-of-the-art Snapshot 3DMA GNSS in New York City: A Case Study. *Proceedings of the 35th International Technical Meeting of the Satellite Division of The Institute of Navigation (ION GNSS+ 2022)*, Denver, Colorado, September 2022. **(Presenter)**.

3. **Ng, H.-F.**, Zhang, G., Wen, W., & Hsu, L.-T. (2021). 3D Mapping Aided GNSS Using Gauss-Newton Algorithm: An Example on GNSS Shadow Matching. *Proceedings of the 34th International Technical Meeting of the Satellite Division of The Institute of Navigation (ION GNSS+ 2021)*, St. Louis, Missouri, 1954-1960. `https://doi.org/10.33012/2021.17994`.

Book Chapter

1. Hsu, L.-T., Zhang, G, & **Ng, H.-F.**. (2024). Map-Aided GNSS Positioning. *Handbook of Wireless Positioning*. Springer, US. (Under review)

Activities/Achievements

1. September 2023: Session co-chairing for session “Applications of GNSS Measurements from Smartphones” in ION GNSS+ 2023, Denver, CO.

2. September 2022: ION GNSS+ Student Paper Award in ION GNSS+ 2022, paper title: ”Multi-Epoch Kriging-based 3D Mapping Aided GNSS Using Factor Graph Optimization”.

3. March 2022: Speaker for ION webinar talk titled ‘Urban positioning: 3D mapping-aided GNSS using dual-frequency pseudorange measurements from smartphones’.

Acknowledgements

Firstly, I would like to express my deepest gratitude to my supervisor, Dr. Li-Ta Hsu, for his invaluable guidance, unwavering support, and constant encouragement throughout the course of my doctoral studies. Their expertise, patience, and mentorship have been instrumental in shaping my research journey and academic growth.

I am also indebted to the members of my thesis committee, Professor NIU, Xiaoji from Wuhan University and Professor ZHANG, Baocheng from Chinese Academy of Sciences, for their insightful feedback, constructive criticism, and scholarly contributions that have enriched the quality of my work.

My sincere appreciation extends to the Department of Aeronautical and Aviation Engineering, for providing a conducive research environment and access to resources essential for conducting my research.

Also, I should give my hearty thanks to several individuals: Associate Professor Paul Groves from University College London provided me with the opportunity for a visiting study and collaborate; Dr. Guohao Zhang for his constructive advice and brilliant ideas in my research; and Dr. Bing Xu for his kind advice and for broadening the scope of my knowledge. I would also like to thank the Institute of Navigation (ION) for inviting me as the speaker for the webinar in March 2023

and the co-chair for ION GNSS+ 2023. Also, being awarded the best student paper in ION GNSS+ 2022 was a huge support for my work in my PhD study. I am profoundly thankful to my colleagues and fellow researchers of the Intelligent Positioning and Navigation Laboratory (IPNL), for their collaboration, camaraderie, and stimulating discussions, which have broadened my perspectives and enhanced my research experience.

I would like to acknowledge the financial support provided by the Hong Kong PhD Fellowship Scheme, which enabled me to pursue my doctoral studies and carry out my research endeavours.

Last but not least, I am grateful to all those who have directly or indirectly contributed to this thesis, whether through academic guidance, intellectual exchange, or moral support. Your contributions have been invaluable and deeply appreciated.

Contents

7 Kriging-based 3DMA GNSS using FGO 114

8 Conclusion 143

List of Figures

List of Tables

Chapter 1

Introduction

1.1 Motivation

Positioning and navigation are irreplaceable for our daily to locate ourselves and bring us to the destination safely. Positioning technologies diversely apply in intelligent transportation systems (ITS) and location-based services (LBS) to localize in absolute coordinate system [1]. Positioning technology requisites can be characterized from diverse perspectives, including considerations of accuracy, integrity, continuity, and availability [2]. Global navigation satellites system (GNSS) usually performs well in these aspects when operating in opensky environments with meter-level accuracy, it can provide absolute positioning under the global coordinate system for these applications [3]. Smartphones and low-cost GNSS receivers typically use multi-constellation capability to maximize the number of received satellites, enhancing the availability of GNSS positioning.

Demand for reliable and accurate positioning is increasing with the urbanization footprint. However, high rise buildings bottleneck GNSS to provide satisfactory performance with the conventional GNSS positioning strategies. GNSS signal transmission in urban canyons is often obstructed, reflected, or diffracted by building surfaces, deviating from a straightforward line-of-sight propagation. Phenomena of non-line-of-sight (NLOS) reception and multipath effect are two common errors when reflection occurs [4]. Two errors are named based on whether the LOS signal is blocked or not. NLOS reception refers to the case that only the reflected signal can reach the receiver. Multipath effect presents when both LOS and reflected signals are arriving the receiver.

The extra traveling distance of reflected signals introduces non-Gaussian errors to the measurements, degrading positioning performance. Assisted positioning approaches, such as GNSS aided by inertial or visual sensors, have been shown to improve performance in various scenarios, including urban environments. However, these aiding approaches primarily provide relative position updates, while absolute coordinate positioning via GNSS remains irreplaceable in such unfavorable conditions. Therefore, it is crucial to develop methods that offer more reliable positioning for performance improvement. Beyond excluding or mitigating unhealthy measurements, correcting these measurements holds significant potential for enhancing performance. 3D mapping-aided (3DMA) GNSS [5] uses 3D building models to significantly improve positioning accuracy.

Several 3DMA GNSS algorithms have been introduced in the last decade, benefitting from the extensive coverage of 3D city models available to researchers. 3DMA GNSS has been widely commercialized and even become a standard built-in function for smartphones [6]. 3DMA GNSS uses the context of 3D models to predict, detect, and even correct GNSS signal errors. 3DMA GNSS can be categorized into two main groups: shadow matching [7], [8] and ranging-based 3DMA

GNSS. Examples of ranging-based 3DMA GNSS include ray-tracing GNSS [9], [10], likelihood-based ranging 3DMA GNSS [11], and skymask 3DMA GNSS [12]. Errors raised by surrounding obstacles are strongly location-dependent, as reflections tend to occur in close proximity to the receivers. As a result, creating a universally applicable correction model for all environments is challenging. 3DMA GNSS positioning algorithms typically use the particle filter concept, aiming to identify a position that optimally matches with the modeled and received measurements. Meanwhile, corrections are applied to satellite visibility for those predicted as NLOS. The candidate-based positioning approach is first distributing several positioning hypothesis candidates and compare the predictions with observations. Shadow matching and ranging-based 3DMA GNSS use distinct features for positioning. The former relies on satellite visibilities as the matching feature, whereas the latter uses pseudorange measurements for matching.

Candidate-based 3DMA GNSS are commonly in single point positioning (SPP) basis. However, SPP is not robust enough for continuous positioning. Due to the high similarity of features and observation outliers, multimodal and drifting problems occur and degrade the positioning reliability over time. Temporal information engages to provide extra constraint to increase the robustness of positioning. Several studies extend the 3DMA GNSS positioning to multi-epoch approach using filtering basis, such as Kalman filter, particle filter, and grid filter. Factor graph optimization (FGO) is widely adopted in the robotics field and draws the attention of GNSS communities, but there is lack of discussion to extend 3DMA GNSS in multi-epoch solution using FGO.

This study is the pioneer on improving the accuracy and robustness of 3DMA GNSS positioning in several perspectives. This study first acknowledges the difficulties of GNSS positioning in urban areas and limitations of existing 3DMA GNSS algorithms via literature reviews in chapter 2. Then, the performance of a basic 3DMA GNSS positioning algorithm is presented in chapter 3, and results from actual recorded data are analysed to identify existing limitations. This study then adopts an L5-band GNSS signal to mitigate the multipath effect and provide a higher quality of NLOS measurements. Also, the uncertainty of the receiver clock estimation in the measurements modelling phase of candidate-based 3DMA GNSS is discussed, and a method to improve the estimation is proposed in chapter 4. Meanwhile, to improve the efficiency of the candidate sampling and propagation, dynamical candidate sampling is proposed chapter 5. After that, the candidate-based 3DMA GNSS is proposed to extend the positioning to a multi-epoch basis using FGO in loosely coupled (chapter 5), hybrid-coupled (chapter 6) and semi-tightly coupled (chapter 7) manners.

1.2 Problem Statements and Objectives

Though 3DMA GNSS shows a promising performance by using NLOS reception as a positioning feature and ensuring a sufficient number of effective satellites, there remain uncertainties and sufficient opportunities for performance improvement. This thesis aims to provide a more accurate and robust 3DMA GNSS positioning framework for low-cost receivers, such as smartphones. Improvement can be made in several perspectives, such as in measurement modelling and positioning phrases. Furthermore, the positioning can be extended to multi-epoch manner via incorporating relative position of consecutive epochs, such as Doppler measurements estimated velocity. And four related problems are identified as the key objectives to be achieved in this study.

1.2.1 Measurements quality enhancement via L5-band signal

In the measurement domain, 3DMA GNSS only uses NLOS reception as the positioning feature, leaving out the mitigation of Multipath effect. This gap occurs because the measurement error is signal-dependent in the receiver, requiring alternative approaches to address this error. Low-cost devices, such as smartphones, are newly capable of receiving the L5-band signal. The nature of the L5-band signal of a higher chipping rate provides excellent performance in excluding multipath error that exceeds one chip length. By this means, this study investigates the performance of L5-band signals for 3DMA GNSS positioning.

1.2.2 Receiver clock modelling over candidate-based approach

In the modeling of pseudorange measurements at each distributed candidate, estimates for atmospheric delays and satellite clock offset can be derived from the parameters provided in the ephemeris. Meanwhile, NLOS delays can be predicted by ranging-based 3DMA GNSS. However, uncertainty arises in estimating the receiver clock offset, which is a device-dependent term without external aiding. This is particularly impactful in low-cost receivers where clock stability may be compromised during continuous operation, significantly affecting positioning performance. Therefore, this study proposed an alternative way to better estimate the receiver clock offset and compared different receiver clock offset modelling methods.

1.2.3 Effective candidate-based 3DMA GNSS in position-domain

The main limitation of a candidate-based approach is its dependence on a relatively accurate initial location, essential for ensuring adequate sampling coverage around the actual location. Conversely, excessively distributed positioning hypothesis candidates can lead to a high computational load. Therefore, this study proposed an environment context-based candidate distribution approach to effectively distributing the sampling candidates.

Meanwhile, multimodal problems degrade the candidate-based 3DMA GNSS. Clustering using region growing is proposed in this study to identify potential multimodal existence and only select the high scores candidates or cluster for positioning and propagation of the sampling at next epoch. This can reduce the uncertainty of 3DMA GNSS positioning.

1.2.4 Multi-epoch 3DMA GNSS using factor graph optimization (FGO)

Multi-epoch positioning has to be considered to increase the robustness of 3DMA GNSS. FGO uses batch optimization concept to include as much as information, providing extra constraint to the position states estimation. There are lack of studies on multi-epoch 3DMA GNSS using FGO, and this study extends the single-epoch candidate-based 3DMA GNSS to a multi-epoch solution.

The optimization is done in both loosely and semi-tightly coupled manners. Loosely coupled FGO integrates position solution from candidate-based 3DMA GNSS and Doppler measurements estimated velocity.

Semi-tightly coupled FGO integrates cost function of 3DMA GNSS and Doppler measurements directly, this maximizes all available information to constraint the state estimation with all historical information as a batch to provide complete optimality. The cost function of 3DMA GNSS is a differentiable function that mathematically models the sampled locations and the likelihood scores of candidate-based 3DMA GNSS. Therefore, nonlinear least squares (NLS) can be adopted to estimate the position solution.

1.3 Thesis Outline

A reminder of this thesis is structured as follows:

Chapter 2 presents a comprehensive review of GNSS positioning algorithms. Requirements and difficulties of GNSS positioning in urban areas are first presented. Then, various conventional and advanced GNSS positioning techniques are reviewed. Finally, different NLOS reception and multipath effect mitigation techniques are discussed from several perspectives: hardware layer, measurement level, and 3DMA GNSS approaches.

Chapter 3 discusses the details of the basic candidate-based 3DMA GNSS. This chapter first explains the position sampling and measurement modelling of different 3DMA GNSS algorithms. Then, the integration of 3DMA GNSS algorithms is explained. Finally, the performance of the basic candidate-based 3DMA GNSS is accessed by actual data from designed experiments to highlight its limitations.

Chapter 4 improves the measurement modelling phase of the candidate-based 3DMA GNSS. Two main improvements have been made to address the limitations. The first improvement is using L5-band measurements in the positioning as dual-frequency 3DMA GNSS. The second improvement is proposing a receiver clock modelling approach for the pseudorange. The performance of the improvements is accessed by the actual recorded dataset of designed experiments in urban canyons.

Chapter 5 extends the candidate-based 3DMA GNSS from single-point positioning into a multi-epoch approach. Position solution from candidate-based 3DMA GNSS integrates with velocity estimated by Doppler measurements in a loosely coupled manner using FGO. Meanwhile, the candidate distribution is done effectively with a context-based distribution. Therefore, real-time positioning can be achieved. The performance of the loosely coupled integration is accessed by real-world datasets recorded in Hong Kong and New York City.

Chapter 6 improves the multi-epoch 3DMA GNSS in the position domain by using a region-growing method to identify the potential occurrence of multimodal and select the cluster using the position of the previous epoch and displacement. Then, the selected cluster and estimated velocity are inputted into FGO to estimate the optimal states of multiple epochs. As the selected cluster has a smaller position covariance than the estimated position without clustering, positions of other epochs with smaller covariance can mitigate the solution of solution solution-shifted epoch to a correct position.

Chapter 7 advanced the integration of the 3DMA GNSS into FGO, and all candidates were modelled as a differentiable continuous function and inputted to the FGO. The modelled continuous function returns the actual cost when inputting a desired location. Therefore, the higher resolution information can better constrain the position estimation. This study uses actual recorded datasets in the vehicular and pedestrian scenarios as the showcase for performance evaluation.

Chapter 8 concludes the thesis and discusses the remaining issues and future work.

1.4 Research Contribution to Research Community

The proposed research topic is divided into five main phases, and each phases are summarized into academic articles. Each milestone and corresponding publications are summarized in Figure 1.1.

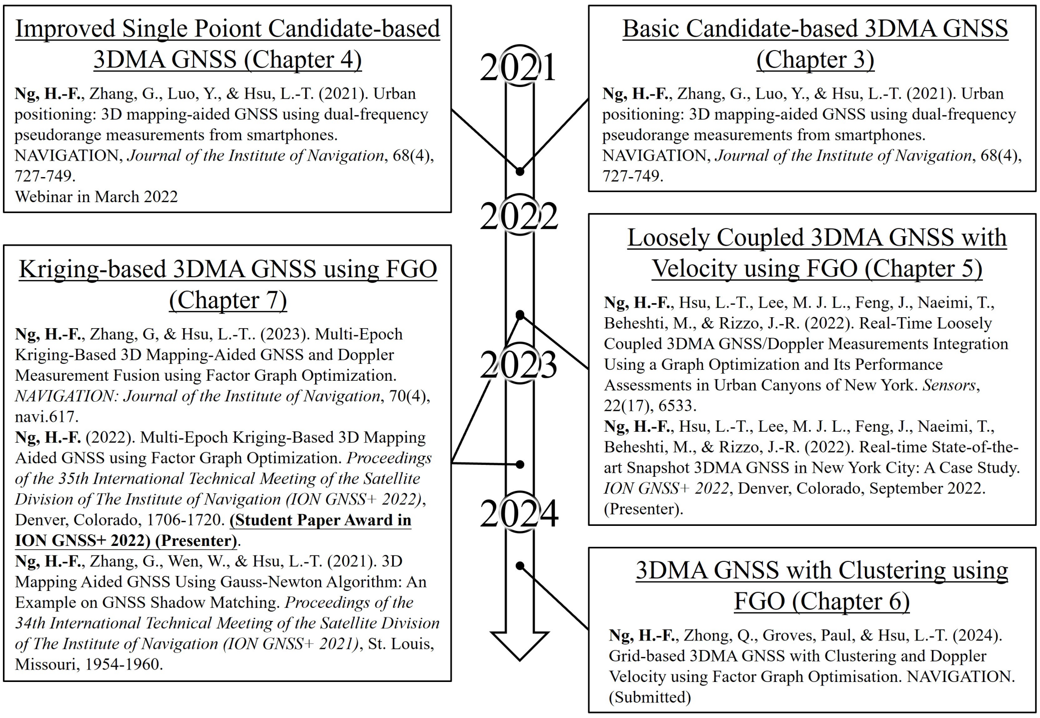

Improved Single Poiont Candidate-based 3DMA GNSS (Chapter 4)

Ng, H.-F., Zhang, G., Luo, Y., & Hsu, L.-T. (2021). Urban positioning: 3D mapping-aided GNSS using dual-frequency pseudorange measurements from smartphones. NAVIGATION, *Journal of the Institute of Navigation*, 68(4), 727-749.
Webinar in March 2022

Basic Candidate-based 3DMA GNSS (Chapter 3)

Ng, H.-F., Zhang, G., Luo, Y., & Hsu, L.-T. (2021). Urban positioning: 3D mapping-aided GNSS using dual-frequency pseudorange measurements from smartphones. NAVIGATION, *Journal of the Institute of Navigation*, 68(4), 727-749.

Loosely Coupled 3DMA GNSS with Velocity using FGO (Chapter 5)

Ng, H.-F., Hsu, L.-T., Lee, M. J. L., Feng, J., Naeimi, T., Beheshti, M., & Rizzo, J.-R. (2022). Real-Time Loosely Coupled 3DMA GNSS/Doppler Measurements Integration Using a Graph Optimization and Its Performance Assessments in Urban Canyons of New York. *Sensors*, 22(17), 6533.
Ng, H.-F., Hsu, L.-T., Lee, M. J. L., Feng, J., Naeimi, T., Beheshti, M., & Rizzo, J.-R. (2022). Real-time State-of-the-art Snapshot 3DMA GNSS in New York City: A Case Study. *ION GNSS+ 2022*, Denver, Colorado, September 2022. (Presenter).

Kriging-based 3DMA GNSS using FGO (Chapter 7)

Ng, H.-F., Zhang, G, & Hsu, L.-T.. (2023). Multi-Epoch Kriging-Based 3D Mapping-Aided GNSS and Doppler Measurement Fusion using Factor Graph Optimization. *NAVIGATION: Journal of the Institute of Navigation*, 70(4), navi.617.
Ng, H.-F. (2022). Multi-Epoch Kriging-Based 3D Mapping Aided GNSS using Factor Graph Optimization. *Proceedings of the 35th International Technical Meeting of the Satellite Division of The Institute of Navigation (ION GNSS+ 2022)*, Denver, Colorado, 1706-1720. **(Student Paper Award in ION GNSS+ 2022) (Presenter)**.
Ng, H.-F., Zhang, G., Wen, W., & Hsu, L.-T. (2021). 3D Mapping Aided GNSS Using Gauss-Newton Algorithm: An Example on GNSS Shadow Matching. *Proceedings of the 34th International Technical Meeting of the Satellite Division of The Institute of Navigation (ION GNSS+ 2021)*, St. Louis, Missouri, 1954-1960.

3DMA GNSS with Clustering using FGO (Chapter 6)

Ng, H.-F., Zhong, Q., Groves, Paul, & Hsu, L.-T. (2024). Grid-based 3DMA GNSS with Clustering and Doppler Velocity using Factor Graph Optimisation. NAVIGATION. (Submitted)

Figure 1.1: Milestones and the corresponding publications of this thesis.

Chapter 2

Background

2.1 Positioning in GNSS-Challenging Environments

Sufficient numbers of LOS satellite are the key for reliable GNSS positioning. Highrise buildings with highly reflectivity surface materials obstruct the GNSS signal transmitted to the receiver, affecting the number and the geometry of the visible satellites. As a result, the performance of GNSS positioning degrades when receiver operates in harsh conditions, such as urban canyons surrounded by tall buildings.

Building blockage of GNSS signal causes the first difficulties on a limited number and poor geometry of the available satellites. Poor geometry results in high dilution of precision (DOP) value. DOP value is higher at the lateral direction of the street because the building geometries are usually distributed at this direction, while a wider sky visibility is parallel to the longitudinal direction of the street. Satellites located in the longitudinal direction of the street are generally the LOS ones, providing better positioning accuracy at this direction.

Satellites distributed along the lateral side of the street, where buildings are located, are frequently blocked or received as reflected signals. This leads to the second challenge of NLOS reception and the multipath effect of the GNSS signals. The reflections violate the LOS signal assumption of GNSS. The additional travel distance of the signal introduces noise to the position estimation, resulting in errors of degraded position achieving 50 m or more [13]. Error behaviors and naming are different for the reflection occurs, it is depending on the status of the LOS signal. NLOS reception occurs when only reflection signal is received by the antenna. While multipath effect refers to the case of both LOS and reflected signals arrive the antenna. They are highly spatial correlated compared to atmospheric delays, where the error sources (blockage and reflecting point) are close to the receiver. When the receiver updates to another location, satellite visibility and ranging delays are totally different.

NLOS reception and multipath effect demonstrate distinct behaviors in terms of signal strength and ranging errors. In NLOS reception, the reflected signal travels an extra distance, leading to a positive ranging error. Simultaneously, when the signal bounces over a building surface, it results in weaker signal strength when arriving at the antenna.

The error associated with the multipath effect is influenced not only by the geometrical error of the reflection but also by the interference within the receiver's correlation process. In cases where the receiver receives multiple signals, several correlation peaks form inside the correlator [4]. Feeding both direct and reflected signals into the correlator can lead to constructive or destructive interference, impacting the equalization of power between the early and late channels. Constructive interference results in positive errors for in-phase reflection, while out-of-phase reflection leads to negative errors. Therefore, the multipath error can be either positive or negative for pseudorange measurements, depending on whether constructive or destructive interference occurs. Similarly, signal strength becomes stronger and weaker for multipath effect during constructive and destructive interference, respectively.

Another signal transmission error is 'diffraction' [14]. Similar to NLOS reception, the signal is attenuated over the building edge. The diffracted signal also travels with an extra delay distance, but this distance is much smaller than that of reflection. Identifying this error is challenging due to its relatively small magnitude, and it only occurs when the signal travels close to the building edge.

Furthermore, low-cost GNSS receivers often have highly sensitive antenna, resulting in measurements with very low carrier-to-noise ratio densities due to the low-cost hardware and baseband processing algorithm designs. These low-quality measurements may not be excluded from positioning algorithms, significantly deteriorating the positioning performance as unhealthy measurements.

2.2 GNSS positioning in general scenarios

Traditional GNSS positioning relies on pseudorange measurements and applies the least squares (LS) method as a SPP basis. However, LS estimation is not robust in handling outliers [15]. To enhance robustness, mass-market products often fuse GNSS positioning with navigation filter, such as the Kalman filter (KF) [16]. However, positioning performance of the KF-based approach may degrade in the presence of non-Gaussian measurement errors [17]. Errors can propagate through the measurements and covariance updates, implying that KF and EKF do not ensure the optimality of the estimated results.

The particle filter can effectively distribute and sample the candidates [18], [19]. Moreover, a grid filter was used to distribute positioning candidates evenly [20]. However, the accuracy of the initial location is important for the distribution of hypothesis positions. Like the KF-based approach, particle and grid filters do not guarantee result robustness.

Factor graph optimization (FGO) is extensively adopted in the robotics and autonomous driving fields due to its inherent robustness [17]. It offers two main benefits among different optimization methods. Firstly, it uses data as a batch and incorporates historical information, improving robustness. Additionally, FGO maintains a reasonable computational load during optimization. Secondly, it provides a flexible optimization architecture that can be easily expanded in scale and factor types. A comprehensive study comparing FGO and EKF in GNSS/INS integration [17]. Results show that FGO outperforms EKF in terms of accuracy and robustness for both loosely-coupled (LC) and tightly-coupled (TC) integration. FGO has demonstrated revolutionary positioning performance in sensor fusion [21], centimeter-level positioning with RTK GNSS [22], and collaborative positioning [23].

It is worth noting that a sliding window-based FGO optimizes in both the forward direction (as filtering) and the backward direction (as smoothing), whereas EKF only performs filtering in the forward direction. For a fair comparison, the EKF should be implemented in a window-based setting, with state updates within the window iteratively calculated.

After applying model corrections, there are still several meters of common errors present, contributing to the user equivalent range error budget [24]. These remaining errors can degrade positioning accuracy. However, since these errors are spatially correlated, such as the atmospheric delays from the same satellite, their magnitudes are similar within the same area. To mitigate this, differencing observations across receivers or base stations with known locations can be empolyed, a technique known as differential GNSS (DGNSS) [3]. In open areas, DGNSS can achieve positioning solution within 1 to 2 meters of error.

The mentioned approaches use pseudorange measurements for positioning but introduce noise that limits resolution to the meter level [3]. To achieve centimeter-level accuracy, real time kinematic (RTK) GNSS positioning is employed, extending the concept of DGNSS by applying the differential technique to carrier phase measurements. Then resolves the ambiguities in carrier phase measurements to get the fixed solution [25], [26]. An alternative method is precise point positioning (PPP), which uses precise orbit and clock ephemerides, along with linear combined multiple-frequency measurements [26], to provide precise locations in centimeter-level positioning accuracy. PPP expands the estimation state to comprehensively model the entire system and converges all unknowns over continuous operation [27], [28]. Although advancements such as the instantaneous PPP-WAR technique [29] relaxing convergence time requirements, carrier phase measurements are still susceptible to multipath errors and cycle slip problems, presenting difficulties for these techniques in urban canyons.

Although quality control procedures can be implemented to detect, identify, and adapt to outliers, they may still persist in the position estimation process, potentially deteriorating performance. Alternative approaches must be developed and implemented to improve positioning reliability.

2.3 NLOS reception and multipath mitigation techniques for GNSS challenging environments

Strategies for addressing NLOS reception and multipath effects can be categorized into identification, mitigation, and correction. These strategies can be implemented at several levels, including hardware, measurement, and additional aiding resources. This subsection introduces techniques for addressing NLOS reception and multipath effects from these perspectives.

2.3.1 Hardware design perspective

Various hardware solutions can aid in identifying satellite blockage. Using hardware offers the advantage of real-time, local recognition of the real-world context using recognition algorithms to classify image regions into skies and obstacles. This approach uses the known positions of satellites and obstacles to determine which satellites are blocked. Therefore, aided positioning with hardware outperforms in identifying dynamic obstacles, such as moving vehicles.

A method using a sky-pointing fisheye camera for NLOS signal detection through image recognition has been introduced [30], [31]. In this approach, a fisheye camera is installed on the roof of a vehicle, pointing toward the sky. During the online positioning stage, the fisheye camera captures the environment as an image. An image recognition algorithm is then employed to classify areas in the image into skies and obstacles. This information is fused with heading information to determine the angular positions of obstacles. By projecting satellites onto the image, this method can identify NLOS satellites, which are then excluded from the positioning process.

Another approach is using 3D light detection and ranging (LiDAR). The NLOS signals can be detected [32] and corrected based on scanned surrounding building distance and NLOS propagation model [33]. In study [32], a LiDAR is used to scan the point cloud of real environments. An object detection algorithm is then applied to identify a double-deck bus, and its dimensions are extended to create a realistic representation if detected. After that, the obstacle is transformed and projected onto GNSS skyplot for NLOS exclusion. Study [33] extends the usage of LiDAR to detect and correct the NLOS reception. This study proposes a LiDAR-based point cloud segmentation method to detect the top boundary of the building. The top boundary information can be used to identify NLOS reception, and using the distance to the building, the NLOS correction can be estimated by the NLOS error model instead of excluding it.

These studies show excellent performance in identifying NLOS satellites, especially in identifying signal blockages based on the actual environments. However, these approaches require extra equipment and increased power consumption, making them impractical for hand-held devices.

2.3.2 Measurement level

The consistency-check method [34] is used to detect and isolate the unhealthy pseudorange measurements, achieving a satisfactory positioning result. It recursively performs a consistency test on residuals of the LS solution and eliminates the largest residual measurement until the test passes or the number of residuals is less than a certain threshold. However, its performance may degrade in the dense urban scenario with severe NLOS reception. Multiple NLOS receptions as the outliers may lead to fault consistency issues, degrading the correctness of fault detection and exclusion [35]. Meanwhile, aggressively excluding measurements can lead to bad satellite geometry or an insufficient number satellites for positioning.

Employing multi-frequency GNSS measurements proves to be an effective way in mitigating the multipath effect, especially with the growing popularity of L5-band signals for civilian use. GNSS L5-band measurements are commonly available in smartphones and low-cost consumer-level receivers in recent years. Studies show that the multi-constellation dual-frequency measurements can provide more accurate clocks and orbital data for smartphones [36]. Usually, they are capable of receiving the L1 C/A, B1I, and E1 signals from GPS/QZSS, BDS, and Galileo, respectively. The latest receiver employing the lower L-band signal (1176.45 MHz) can receive more signals in addition to the preceding signals, such as the L5 signal of GPS/QZSS [37], [38], the E5a signal of Galileo [39] and the B2a signal of BeiDou-3 [40]. The combination of GPS/ Galileo /BDS can achieve a satisfactory satellite geometric distribution for positioning [41]. GNSS L5-band signal has excellent potential to contribute to civilian positioning applications.

GNSS L5-band signals are less affected by the multipath effect compared to the commonly used L1 C/A signals. This is attributed to the design of the L5-band signal, which features a higher chipping rate and shorter chip length than the open-service civil L1-band signal [42]. Owing to the property of the spreading code, when the multipath error exceeds one chip length, the amplitude of the auto-correlation between the incoming multipath code signal and the local replica is significantly reduced [3]. Therefore, the accuracy of the code tracking error discriminated by a commonly used three-channel correlator in terms of the LOS signal can be efficiently improved as its autocorrelation function is unlikely to be distorted by the multipath effect. Moreover, the L5-band signal benefits from a smaller chip length than that of the L1 C/A signal. The L5-band signal includes a smaller multipath error than the latter. The code Doppler frequency can be measured to be closer to the truth. As a result, according to the theory for the design of the receiver, both the pseudorange and the carrier phase measurements can be improved [43].

The research attempts to explore methods to optimize the usage of L5-band measurements for enhancing positioning accuracy. The benefits of harnessing the L5 signal-to-noise ratio for multipath reflectometry are thoroughly examined [44]. The signals vary in wavelength and demonstrate distinct ionospheric delays [45]. Therefore, a study explores using the linear combination of dual-frequency signals to eliminate the ionospheric delay [46]. Additionally, some studies combine triple-frequency measurements on L1/L2/L5 to enhance positioning performance for single-point positioning [47] and advanced receiver autonomous integrity monitoring [48].

Furthermore, in the presence of multipath, GNSS signals with varying wavelengths exhibit distinct behaviors in terms of signal-to-noise ratio. This characteristic has been applied to detect the multipath effect for geodetic GNSS receivers in urban areas [49]. A study [50] introduced a novel integrated positioning algorithm that using GNSS L1/L5 bands, featuring outlier isolation designed specifically for dual-frequency enabled receivers for urban positioning.

L5 signals also play a crucial role in achieving centimeter-level positioning accuracy, as demonstrated in techniques like precise point positioning (PPP) [51] and real-time kinematic (RTK) GNSS [25]. PPP applies triple-frequency measurements to accelerate the convergence process [52], [53]. The advantages of the L5 signal have also been employed by multi-frequency geodetic receiver [54] to enhance PPP [55] or RTK positioning [56].

L5 signals serve to reduce multipath effects and isolate errors in NLOS reception [6]. Consequently, algorithms have a significant potential to estimate NLOS delays with greater precision using these improved NLOS measurements.

2.3.3 Handling NLOS reception with 3DMA GNSS

NLOS reception and multipath are highly spatial correlated with the surrounding buildings, making it essential to use extra resources for environmental perception to detect any NLOS signal transmission. 3D building models digitally formalize the entity of the city infrastructures. With the widespread digitalization of smart cities, 3D building models are widely accessible for major cities globally, such as in Hong Kong, China [57], [58], New York City, US [59], Tokyo, Japan[60], London, UK [61], Schiphol, Netherlands [62], Delft, Netherlands [63], and Daejeon, Korea [64].

The available 3D building model makes it possible to aid the urban positioning, namely 3D mapping aided (3DMA) GNSS [5]. 3DMA GNSS can be used in a low-cost receiver as a software-based approach to enhance positioning capabilities. It predicts satellite visibility and transmission path propagation, which can be divided into two primary categories: shadow matching (SM) [7], [8] and ranging-based 3DMA GNSS, such as likelihood-based ranging (LBR) [11], ray-tracing GNSS [9], [10], and skymask 3DMA (SKY) [12].

3DMA GNSS demonstrates a strong capability for detecting NLOS receptions using georeferenced building models. Consequently, it can accurately predict the actual locations of blockages and reflections based on the specified positions of the desired location and satellites.

2.3.3.1 Digitalization of cities

Various technologies facilitate the straightforward acquisition of 3D building models by integrating satellite imagery and airborne LiDAR data [65]. While satellite images offer 2D building outlines, airborne LiDAR provides detailed building heights, resulting in comprehensive 3D models. The establishment of large-scale 3D building models is thoroughly reviewed in [66], this enables us to rapidly generate 3D building models with extensive coverage. Additionally, an increasing number of open-source building models are freely available on the market. Crowdsourcing also contributes to open data initiatives, such as OpenStreetMap (OSM) [67], which collects user-generated street maps, including 2D building contours with details like the number of floors or absolute height.

In practical implementation, the 3D building models are usually pre-processed remotely and the information is stored in the device for online applications. The 'Skymask' represents a processed format for satellite visibility prediction, consisting of a skyplot overlaid with projected building boundaries for a specific location. The azimuth angle starts from the north direction, rotating clockwise; the elevation angle begins from the horizon at 0°. If the satellite's elevation angle is lower than that of the building boundary (at the same azimuth angle), the signal is presumed to be obstructed by buildings, indicating a NLOS signal. The area of interest (AOI) covered by the skymask is typically subdivided into a grid of points. In [12], the grid's horizontal position resolution is set at 2 meters, while the azimuth is resolved in 1-degree increments, and the elevation in 0.1-degree increments. In 3DMA GNSS, it is assumed that the candidate always remains at ground level, specifically at mean-sea-level (MSL). Consequently, the height of the skymask position is referenced to the MSL datum, which can be obtained from sources such as the data provided by the Hong Kong Lands Department [68].

2.3.3.2 NLOS reception exclusion

An existing study uses the 3D building model to exclude the NLOS satellites, and the weighted least-squares (WLS) solution was enhanced [69], [70].

2.3.3.3 Shadow Matching

Evaluation in [71] reveals limitation in satellite visibility, with satellite blockage simulated by 3D building models indicating that positioning uncertainty is typically larger in the lateral direction of the street compared to the longitudinal direction. Hence, it is important to ensure reliable positioning t accurately determine the user's precise location on the correct side of the street. Shadow matching was developed to facilitate this demand [7], [8]. It uses building boundaries extracted from the 3D city model and satellite positions obtained from the ephemeris to estimate satellite visibility at given location. The shadow matching technique uses the building boundaries [71], specifically the highest elevation angle of the surrounded building on each azimuth angle, extracted from the 3D city model. It also incorporates the position of the satellite obtained from the ephemeris to predict the satellite visibility at a specific location. Shadow matching operates under the assumption that the received satellites are in LOS, while any non-received satellites listed in the ephemeris are considered NLOS. By comparing predictions and observations within a scoring framework, candidates are scored accordingly. Consequently, the user's position can be determined based on the candidate location with satellite visibility that best matches the measurements. It can effectively enhance positioning accuracy along lateral streets by offering more distinctive building boundary features in that direction. However, its effectiveness is somewhat diminished along longitudinal streets, primarily because of the similarity in building geometry along this direction.

The fundamental concept behind the scoring scheme in shadow matching is assessing the consistency between LOS and NLOS predictions and the actual reception status of the signal. At its core, the scoring mechanism employs an exclusive NOR (XNOR) logic gate, where a score is assigned to the LOS-predicted satellite that is indeed received, and conversely. The table of the scoring scheme is shown in Figure 2.1(a). However, the effectiveness of shadow matching is compromised in scenarios involving NLOS reception. When an NLOS signal is mistakenly identified as a LOS one and included in the matching process, it can significantly degrade the performance of the algorithm. To address this, the received signals are categorized into strong and weak signals based on their signal strength, using a threshold determined through experience. Weak signals, indicative of uncertainty, are assigned lower scores within the scoring scheme, as shown in Figure 2.1(b). Furthermore, a novel weighting scheme is proposed, using the C/N_0 values to estimate the LOS probability for matching [8]. In this approach, C/N_0 value are incorporated into a probability function to estimate the probability of LOS. This probability is then used to compare the LOS and NLOS predictions, providing a measure of visibility consistency.

Another study uses an intelligent classifier [72] to identify the NLOS-received

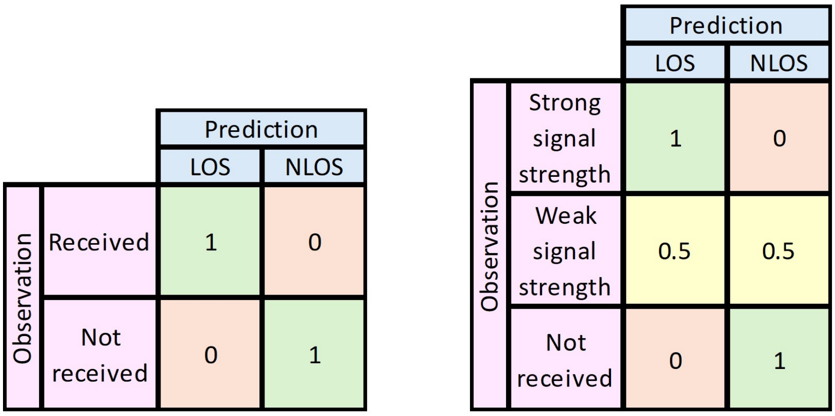

		Prediction	
		LOS	NLOS
Observation	Received	1	0
	Not received	0	1

(a)

		Prediction	
		LOS	NLOS
Observation	Strong signal strength	1	0
	Weak signal strength	0.5	0.5
	Not received	0	1

(b)

Figure 2.1: Scoring matrix for the matching process of shadow matching [8].

satellites in shadow matching [73]. This study uses different LOS/NLOS labels with different GNSS features to train a machine learning classifier, specifically a support vector machine (SVM). During the online positioning stage, the C/N_0 value is fed into the SVM to calculate the LOS probability. Furthermore, the concept of key satellites is introduced, which are satellites positioned angularly close to building boundaries. The visibility of key satellites fluctuates depending on nearby locations. Therefore, these key satellites can be used to assess the confidence level of shadow matching, indicating how accurately the available satellites align with the building boundaries.

2.3.3.4 Ranging-based 3DMA GNSS

Since shadow matching offers only a partial solution, the ranging-based 3DMA GNSS method is demonstrated to focus on the use of pseudoranges to improve the performance in the longitudinal-street direction. The ranging-based 3DMA GNSS method predicts satellite visibility, estimates reflection delays, and simulates GNSS pseudorange at each sample location. Similar to shadow matching, the user's location is determined based on the sample location with the highest similarity between simulated and received pseudorange. Reflection delays are only available if the satellite is classified as NLOS at a particular sample location. Strategies for reflection delay estimation can be divided geometrically and statistically.

Ray-tracing GNSS [9], [10] determines the reflecting point geometrically by validating the transmission paths over building surfaces and calculating the extra travelling distance as the NLOS delays. Studies use particle filters to match the C/N_0 [74] and pseudorange [75] to determine the user's location. However, the ray-tracing technique requires an enormous computational load, especially in densely urbanized areas with numerous buildings. Different studies try to reduce the computational load, making the algorithm suitable for practical implementation. Study [76] employs an off-site approach to compute reflection delays, storing them in the device for online application. Additionally, another study uses graphical processing unit (GPU) to accelerate simulations [77], [78]. Study [12] determines the reflecting point effectively on an enhanced skymask and calculates delays using a set of trigonometric functions.

In contrast, the likelihood-based ranging 3DMA GNSS adopts a statistical methodology to remap NLOS pseudorange errors into LOS measurements [20]. It uses a skew–normal distribution to model the NLOS delay measurements, subsequently remapping these errors to LOS measurements using a normal distribution. Given that healthy LOS satellites are typically distributed along the longitudinal direction of streets, the ranging-based 3DMA GNSS is better at determining the user's location in this direction.

The integration of ranging-based 3DMA GNSS and GNSS shadow matching offers complementary benefits owing to the distinct distributions of buildings.

This integrated approach aims to harness these benefits and enhance overall performance [20], [79]. Although the overall positioning accuracy is improved to approximately 10 m in dense urban environments, the snapshot-based approach exhibits reduced robustness in continuous positioning. Multi-modal and solution drifting issues are the main limitations that affect positioning performance.

2.3.3.5 Multi-epoch 3DMA GNSS

Many navigation applications require continuous operation, especially for pedestrians carrying smartphones while walking along streets. To enhance 3DMA GNSS, researchers have explored incorporating temporal links between solution epochs. Several research groups have investigated the use of filtering techniques to implement 3DMA GNSS with inter-epoch connections.

For example, the Kalman filter (KF) and extended Kalman filter (EKF) have been employed to recursively update the current state by predicting based on past estimations and the errors of current measurements [16]. A study uses EKF to integrate shadow matching with INS measurements [80]. Additionally, the particle filter has been employed to efficiently distribute and sample the candidates [19], [75]. Moreover, a grid filter was used to evenly distribute positioning candidates [20].

Furthermore, machine learning techniques have been used to estimate the most likely paths on a map, optimizing position estimation [81]. It used machine learning to predict signal status changes, corresponding to intelligent signal status estimation. The result indicated that these techniques could enhance position estimation accuracy.

These studies have demonstrated that filtering techniques can enhance positioning performance by providing smoother and more accurate results. However, there is a risk of accumulating measurement errors during the propagation stage, leading to degradation in the reliability of positioning performance over time.

2.3.3.6 Precise positioning with 3DMA GNSS

Carrier phase measurements are easily interfered with by both NLOS reception and multipath effects. Using 3D models presents a promising solution for identifying and excluding these unhealthy measurements from RTK or PPP GNSS positioning.

An innovative approach known as the continuous-LOS method [82] has been developed. This method assumes that the continuously tracked pseudorange and carrier phase measurements indicate good quality of the measurements, thereby enhancing positioning accuracy by only relying on healthy measurements. The results show the significance of selecting healthy satellites, particularly those with continuous LOS satellites, for GNSS RTK positioning. By using 3D models, it predicts satellite visibility and establishes a threshold for continuous LOS duration, varying by the satellite system (e.g., 6 seconds for GPS, GLONASS, and QZSS, and 15 seconds for Beidou). Only satellites continuously predicted as LOS for longer than the specified threshold duration are employed for RTK GNSS, leading to an increase in RTK fixing rate from 1.2% to 7.7%. Notably, the 3D model-based prediction achieves an 88% correctness in predicting continuous LOS signals.

Furthermore, study [83] has demonstrated the potential of 3D maps in enhancing RTK GNSS by selectively using LOS signals. Through a sampling approach within a designated area, the study exclusively incorporates LOS satellites for RTK GNSS positioning. Results validate that approximate positions within a range of 5 m to 15 m from the actual antenna location can still yield accurate fixed positions by RTK GNSS positioning. Expanding on this finding, study [84] introduces the application of the 3DMA position hypothesis GNSS method to RTK GNSS positioning, named 3DMA GNSS RTK. This approach proposes a method for selecting the optimal healthy satellites for RTK GNSS positioning. By sampling positions within the AOI and selecting only LOS satellites for RTK GNSS positioning, likelihood scores for each sampled position are determined by evaluating the residual of the double-differenced carrier phase with estimated ambiguities. Finally, LOS satellites at the weighted average position are employed to compute the optimal RTK GNSS solution.

For UAV applications, using 3D maps can optimize path planning to avoid GNSS challenging areas and maximizing RTK GNSS performance [85]. This study uses buildings and vegetation within the AOI to construct a GPS geometry map. This map contains site-specific predictions of satellite visibility and PDOP. Subsequently, this information is integrated into the flight planner to navigate away from GNSS challenging environments characterized by high PDOP values. In cases where avoidance is not feasible, blocked satellites are identified using obstruction adaptive elevation masks (OAEMs) and subsequently excluded from RTK GNSS positioning. These OAEMs are adaptive elevation angle masks that delineate obstructions from various directions, using georeferenced 3D point clouds obtained from terrestrial laser scanners (TLS).

Chapter 3

Basic Candidate-Based 3DMA GNSS

3DMA GNSS can identify the locations of blockage and reflection. However, as the actual location of the receiver is unknown, the 3D building model cannot correct the measurements directly. Therefore, 3DMA GNSS positioning usually applies filtering techniques to estimate the position. Candidate-based 3DMA GNSS positioning aims to find a position with the highest similarity between the modelled and received measurements. It can be expressed mathematically,

$$\mathbf{x}_k^* = \arg\min_{\mathbf{x}} \left\| \hat{\mathbf{y}}_k \left(\mathbf{x} \right) - \mathbf{y}_k \right\| \tag{3.1}$$

where $\mathbf{x}$ and $\mathbf{x}_k^*$ are desire and estimated state, respectively. $\hat{\mathbf{y}}_k \left(\mathbf{x} \right)$ is the predicted measurements at state $\mathbf{x}$ at epoch k. $\mathbf{y}_k$ is the received measurements at epoch k. Components included in the state diverse for measurements, such as state estimation for pseudorange consists of receiver's position, $\mathbf{r}_k$, and clock offset, δt_k, as,

$\mathbf{x}_k = [\mathbf{x}_k, \delta t_k]^\intercal$.

A flowchart of a basic candidate-based 3DMA GNSS positioning process is shown in Figure 3.1. The implementation follows the author's work presented in [86], and this thesis builds upon that work. Initially, position hypothesis candidates are distributed around the initial location. Then, GNSS measurements are simulated for each candidate and compared with observations to calculate likelihood scores. Finally, the candidate with the highest similarity between simulation and measurement is identified as the receiver location.

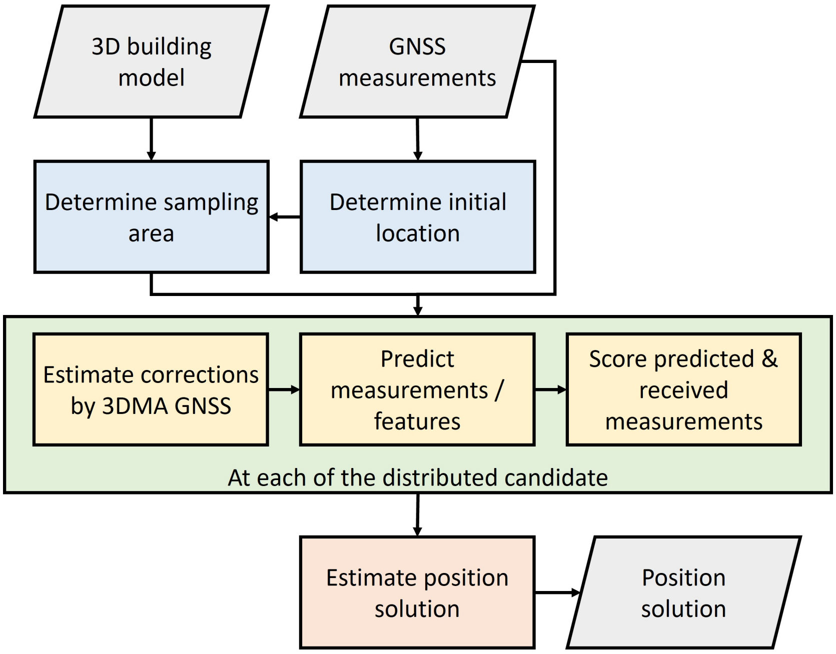

Figure 3.1: System flowchart on the candidate-based 3DMA GNSS.

3.1 Initializing candidates

In practical implementation, a database of skymasks is generated in a grid format evenly distributed within the AOI. Therefore, the sampling of positions is also evenly separated so that it is easy to look up in the database. Initially, a set of positioning hypothesis candidates at epoch k, $\{\mathbf{r}_{k,j}\}$, is distributed around the initial location, $\mathbf{r}_{k,0}$, with a determined sampling radius, r_k. It can be expressed as,

$$\{\mathbf{r}_{k,j}\} = \{\mathbf{r}| \, \|\mathbf{r} - \mathbf{r}_{k,0}\| < r_k\} \tag{3.2}$$

where $\|\cdot\|$ is the Euclidean distance between locations.

Sampling radius, r_k, is determined based on experience and should be larger than the position error of the initial location to ensure that the candidate distribution covers the receiver location. Various approaches can be selected as the initial location, $\mathbf{r}_{k,0}$. The most common approach is to use the WLS, as in study [79], or the device solution, as in study [12], [73]. Alternatively, the position of the previous epoch can serve as the initial location and the sampling radius is doubled, as demonstrated in study [20].

3.2 Sampling candidates

The sampling process consists modelling the measurements and scoring each candidate. Measurements are modelled based on different 3DMA GNSS algorithms for each distributed candidate, with the modelling based on visibility predictions at the corresponding location. Then, a score is given to each candidate based on the similarity or consistency between the modelled and received measurements.

3.2.1 Shadow matching

Shadow matching [7], [87] compares the visibility consistency between received satellites and predictions at a given position based on the building model. It compares the received satellite signals and visibility predictions on each positioning hypothesis candidate to locate the position with the highest similarity as the solution [71]. The implementation of the shadow matching used is based on [11]. The satellite visibility is estimated for each satellite on each candidate's skymask. The probability of satellite i at candidate j is predicted to be direct LOS using skymask, $p\left(LOS|BB\right)_j^i$, where BB stands for 'building boundary', is calculated using the following formula,

$$p\left(LOS|BB\right)_j^i = \begin{cases} 0.8 & \text{LOS} \\ 0.2 & \text{NLOS} \end{cases} \tag{3.3}$$

the applied values in this study are determined empirically, which account for the prediction uncertainties, such as the accuracy of the 3D building model or signal diffraction by obstacles not accounted for in the model. Besides, the probability of each signal to be directed to LOS is predicted by using C/N_0 measurement, $p\left(LOS|C/N_0\right)^i$ is given by the following formula,

$$p\left(LOS|C/N_0\right)^i = \begin{cases} p_{0-min} & (C/N_0) \leq s_{min} \\ a_0 + a_1(C/N_0) + a_2[(C/N_0)]^2 & s_{min} < (C/N_0) < s_{max} \\ p_{0-max} & (C/N_0) \geq s_{max} \end{cases} \tag{3.4}$$

where p_{0-min}, s_{min}, p_{0-max}, s_{max}, a_0, a_1, and a_2 refer to the empirically determined constants, which follows the values used in [20]. Therefore, the score of the matching between the predicted and measured satellite visibility can be calculated as,

$$P_j^i = 1 - p\left(LOS|BB\right)_j^i - p\left(LOS|C/N_0\right)^i + 2p\left(LOS|BB\right)_j^i p\left(LOS|C/N_0\right)^i \tag{3.5}$$

Finally, the score of shadow matching on a candidate can be obtained by the product of all satellites' matching scores,

$$\Lambda_{j,SM} = \prod_i P_j^i \tag{3.6}$$

3.2.2 Ranging-based 3DMA GNSS

The ranging-based method models the pseudorange of satellite i at candidate j, as $\hat{\rho}_j^i$, and compares it with the measured pseudorange, $\tilde{\rho}^i$. In theory, the candidate near the ground truth (GT) should obtain a smaller difference between the modelled and measured pseudorange, that is $\hat{\rho}_{GT} \approx \tilde{\rho}$. The modelled pseudorange can be expressed as follows:

$$\hat{\rho}_j^i = \|\mathbf{r}_j - \mathbf{r}^i\| + \mathrm{c}(\delta t_j - \delta t^i) + I_j^{i,\mathrm{L1}} \left(\frac{\lambda^{i,f}}{\lambda^{i,\mathrm{L1}}}\right)^2 + T_j^i + \varepsilon_{j,\mathrm{NLOS}}^i + \varepsilon_j^i \tag{3.7}$$

where $\|\mathbf{r}_j - \mathbf{r}^i\|$ represents the true range with Sagnac effect [16], calculated using the given satellite ECEF position, $\mathbf{r}^i$, and candidate ECEF position, $\mathbf{r}_j$; c denotes the speed of light; δt_j indicates the time delay of the receiver clock to the corresponding satellite constellation; δt^i is the satellite clock delay provided by the ephemeris data; $I_j^{i,\mathrm{L1}}$ refers to the modelled ionospheric delay for the L1-band signal [88]. Since the ionospheric error varies due to the different wavelengths for

L1- and other signals, a constant is needed to tune this error, calculated based on the wavelengths of the L1-band, $\lambda^{i,\mathrm{L1}}$, and corresponding frequency band, f, as $\lambda^{i,f}$, of corresponding satellite, that is, $\left(\lambda^{i,f}/\lambda^{i,\mathrm{L1}}\right)^2$. T_j^i represents the modelled tropospheric delay [89]. It is worth noting that the corrections provided by tropospheric and ionospheric models can be replaced by satellite-based augmentation system (SBAS) messages, which can improve the modelling of pseudorange [90]. However, this study uses conventional methods for simplicity. $\varepsilon^i_{j,\mathrm{NLOS}}$ refers to the reflection delay for the NLOS reception. ε^i_j denotes the thermal noise of the receiver. Moreover, the receiver clock bias δt_j introduces significant uncertainty to the pseudorange modelling process. This bias can be estimated using the weighted least squares (WLS) method or eliminated through the single difference (SD) technique.

The difference between the modelled and received pseudoranges is computed as,

$$\Delta\boldsymbol{\rho}_{j,*} = \tilde{\boldsymbol{\rho}} - \hat{\boldsymbol{\rho}}_{j,*} = [\tilde{\rho}^1 - \hat{\rho}^1_{j,*}, \hat{\rho}^2_{j,*}, ..., \tilde{\rho}^i - \hat{\rho}^i_{j,*}]^{\mathrm{T}} \tag{3.8}$$

where $*$ represents the type of the ranging-based 3DMA GNSS. For example, the subscript 'SKY' stands for skymask 3DMA, while 'LBR' denotes likelihood-based ranging. It is noted that 3DMA GNSS assumes no NLOS delay if the satellite is predicted as LOS, for example, $\varepsilon^i_{j,\mathrm{NLOS}} = 0$, and no NLOS delay correction is applied.

The pseudorange difference is then used to calculate the score for the candidate, $\Lambda_{j,*}$, which is expressed as,

$$\Lambda_{j,*} = \exp\left(-\boldsymbol{\Delta\rho}^{\mathrm{T}}_{j,*}\mathbf{Q}^{-1}\boldsymbol{\Delta\rho}_{j,*}\right) \tag{3.9}$$

where **Q** refers to a diagonal matrix containing the uncertainty for each satellite,

$$\mathbf{Q} = \mathrm{diag}([\tau^1, \tau^2, ...\tau^i]) \tag{3.10}$$

where τ^i represents the measurement uncertainty of the satellite i. In this study, the uncertainty is calculated based on the carrier-to-noise ratio, $(C/N_0)^i$, and elevation angle θ^i [91], expressed as follows:

$$\tau_1^i = \begin{cases} \dfrac{1}{\sin^2\theta^i}\left(10^{-\frac{(C/N_0)^i - \mathrm{T}}{\mathrm{a}}}\left(\left(\dfrac{\mathrm{A}}{10^{-\frac{\mathrm{F}-\mathrm{T}}{\mathrm{a}}}} - 1\right)\dfrac{(C/N_0)^i - \mathrm{T}}{\mathrm{F}-\mathrm{T}} + 1\right)\right) & (C/N_0)^i < \mathrm{T} \\ 1 & (C/N_0)^i > \mathrm{T} \end{cases} \tag{3.11}$$

where T, F, A, and a refer to the empirical constants used to control the model performance, respectively.

If the satellite is predicted as NLOS at the corresponding candidate location, ranging correction is provided by ranging-based 3DMA GNSS to model the pseudorange measurement. Several ranging-based 3DMA GNSS methods can estimate the reflection delay, as presented in previous section, such as likelihood-based ranging (LBR) [20], ray-tracing GNSS [9], [10], and skymask 3DMA (SKY) [12]. This study mainly focuses on LBR [20] and SKY [12] due to their computational efficiency. The modelled pseudorange with NLOS error $\varepsilon^i_{j,\mathrm{NLOS}}$ is given by the following formula:

$$\hat{\rho}^i_{j,\mathrm{NLOS}} = \hat{\rho}^i_j + \varepsilon^i_{j,\mathrm{NLOS}} \tag{3.12}$$

ranging-based 3DMA GNSS algorithms try to estimate or eliminate $\varepsilon^i_{j,\mathrm{NLOS}}$ for pseudorange modelling.

3.2.2.1 Likelihood-Based Ranging

Likelihood-Based ranging (LBR) [11] eliminates the NLOS delays in pseudorange difference, where NLOS pseudorange difference should be dominated by the NLOS delay error, $\varepsilon_n^{refl(i)}$. Equation 3.12 can yield to,

$$\Delta\rho_{j,\mathrm{NLOS}}^i = \tilde{\rho}^i - \hat{\rho}_{j,\mathrm{NLOS}}^i = \tilde{\rho}^i - \left(\hat{\rho}_j^i + \varepsilon_{j,\mathrm{NLOS}}^i\right) \approx -\varepsilon_{j,\mathrm{NLOS}}^i \tag{3.13}$$

A reference satellite is first selected by a scoring algorithm,

$$s^i = \frac{1}{n_{j'}} \sum_{j'} \left(\theta^i - BB_{j',\psi^i}\right) \times (C/N_0)^i \tag{3.14}$$

where $\frac{1}{n_{j'}} \sum_{j'} \left(\theta^i - BB_{j',\psi^i}\right)$ is the average value of the elevation angle difference between satellite and skymask at corresponding azimuth angle. j' denotes the candidate j and its immediate neighbours, $j' = j, 2, \cdots, n_{j'}$. Immediate neighbours refer to the candidate locations that are less than 1.5 times the grid spacing. The satellite with the highest score, s^i, is selected as the reference satellite.

After that, the standard deviation of all errors except for the NLOS reflection delay is computed using a function based on C/N_0,

$$\sigma^i = \sqrt{\mathrm{a} \times 10^{-(C/N_0)^i/10} + \mathrm{b}} \tag{3.15}$$

where a and b refer to the empirically determined constant. The parameters tuning follows in [20] used.

Satellite visibility is first classified at each positioning candidate using the corresponding skymask. Pseudorange difference of LOS predicted satellite is modelled by a normal distribution with a mean of μ_L. While pseudorange difference of NLOS predicted satellite, $\Delta\rho^i_{j,\mathrm{NLOS}}$, is remapped using a skew-normal distribution to determine the cumulative probability of F_{NLOS}. The skew-normal distribution represents using three parameters, which are location, ξ, scale, ω, and shape, α. These parameters are obtained by using the following formula:

$$\xi = \mu_L + \mu_N - \sqrt{\frac{2\sigma_N^2\left(\sigma_i^2+\sigma_r^2+\sigma_N^2\right)}{\pi\left(\sigma_i^2+\sigma_r^2\right)+(\pi-2)\,\sigma_N^2}} \tag{3.16}$$

$$\omega = \sqrt{\frac{\left(\sigma_i^2+\sigma_r^2+\sigma_N^2\right)^2}{\sigma_i^2+\sigma_r^2+\left(1-\frac{2}{\pi}\sigma_N^2\right)}} \tag{3.17}$$

$$\alpha = \sqrt{\frac{\sigma_N^2}{\sigma_N^2+\sigma_r^2}} \tag{3.18}$$

where μ_N and σ_N denote empirical tuned constants on mean and standard deviation of NLOS reflection delay, respectively. μ_L referees to the mean of LOS pseudorange difference, and σ_r denotes the error standard deviation of the reference satellite. The cumulative probability of NLOS pseudorange difference, F_{NLOS}, can be obtained by substituting the values in (Equation 3.16)-(3.18) into,

$$F_{\mathrm{NLOS}} = \frac{1}{2}\left[1+\operatorname{erf}\left(\frac{\Delta\rho^i_{j,\mathrm{NLOS}}-\xi}{\omega\sqrt{2}}\right)\right] - 2\mathrm{T}\left(\frac{\Delta\rho^i_{j,\mathrm{NLOS}}-\xi}{\omega},\alpha\right) \tag{3.19}$$

where integral of the normal distribution, erf$(\cdot)$, and Owen's T function, $\mathrm{T}(\cdot)$, can be calculated by the following formula,

$$\operatorname{erf}(x) = \frac{2}{\sqrt{\pi}}\int_0^x \exp -t^2\,dt \tag{3.20}$$

and

$$\mathrm{T}\left(x\right)=\frac{2}{2\pi}\int_{0}^{\alpha}\frac{\exp\left(-\frac{1}{2}x^{2}\left(1+t^{2}\right)\right)}{1+t^{2}}\,dt \tag{3.21}$$

, respectively.

Finally, NLOS measurement can be remapped to the corresponding direct LOS error distribution of zero-mean Gaussian distribution by CDF. The remapped pseudorange difference, $\Delta\hat{\rho}^{i}_{j,\mathrm{LBR}}$, can be obtained from F_{NLOS} by solving:

$$F_{\mathrm{NLOS}}=\frac{1}{2}\left[1+\mathrm{erf}\left(\frac{\Delta\rho^{i}_{j,\mathrm{LBR}}}{\sqrt{2(\sigma_{i}^{2}+\sigma_{r}^{2})}}\right)\right] \tag{3.22}$$

where F_{NLOS} at the left-hand side refers to the NLOS CDF, while the right-hand side includes the corresponding LOS CDF, which makes the LOS and NLOS measurements comparable in the same hypothesis for positioning. As a result, the NLOS pseudorange difference becomes NLOS error-free, as $\Delta\rho^{i}_{j,\mathrm{LBR}}$. Estimated pseudorange difference is substituted back to Equation 3.8 to calculate the likelihood score of the candidate.

3.2.2.2 Skymask 3DMA GNSS

Skymask 3DMA [12] is a simplified version of ray-tracing GNSS [9], [10], which reduces the computational load of ray-tracing GNSS while maintaining an almost identical accuracy. Skymask 3DMA utilizes the ‘enhanced skymask’, which also consists of the building height information and azimuth angle of the reflecting planes (AARP) associated with each azimuth angle. Consequently, the reflecting point can be detected by using the AARP value and building height information.

Skymask 3DMA requires the NLOS predicted satellite’s azimuth and elevation angles, which are ψ_j^i and θ_j^i, respectively, which enhanced the skymask of the candidate of BB_j. Then, the reflecting point azimuth and elevation angles can be obtained by using the AARP value. With the building height information on the corresponding azimuth and elevation angle of the reflecting point, the position of the reflecting point can be obtained as well. Therefore, the reflection delay, $\varepsilon_{j,\mathrm{NLOS}}^i$, can be calculated by subtracting the distance between the satellite and the candidate from the total distance of the reflection path. Therefore, the modelled pseudorange of skymask 3DMA, $\rho_{j,SKY}^i$, can be obtained. It is worth noting that only the LOS and NLOS with reflection found satellites are going to score the candidate, that is, $i \in \{\text{LOS,NLOS with reflection}\}$. The NLOS reflection delay, $\varepsilon_{j,NLOS}^i$, can be obtained by Equation (2), notated as $\varepsilon_n^{refl(i)}$, in [12] after locating the reflection point which is determined by the enhanced skymask at the candidate and AARP of the surrounding potential reflector. The pseudorange difference of $\Delta\rho_{j,SKY}$, weighted root mean square error of $\delta\rho_{j,SKY}$ and the score for the candidate of $\Lambda_{j,SKY}$ can be obtained by Equation 3.8 and Equation 3.9, respectively.

3.2.3 Integration of 3DMA GNSS algorithms

After obtaining the likelihood scores from two ranging-based 3DMA GNSS algorithms, which are $\Lambda_{j,\mathrm{LBR}}$ and $\Lambda_{j,\mathrm{SKY}}$. Their pseudorange differences integrate complementarily based on the status of finding the exact reflecting point,

$$\hat{\rho}_{j,\mathrm{RNG}}^i = \begin{cases} \hat{\rho}_{j,\mathrm{LBR}}^i & \text{if no reflection is found by SKY} \\ \hat{\rho}_{j,\mathrm{SKY}}^i & \text{if a reflection is found by SKY} \end{cases} \tag{3.23}$$

The pseudorange difference for LOS predicted satellite is identical for both SKY and LBR methods at the corresponding candidate, as no NLOS delay correction is required. As a result, pseudorange difference of integrated ranging-based 3DMA, RNG, at candidate, $\boldsymbol{\Delta\rho}_{j,\mathrm{RNG}}$, can be obtained using Equation 3.8. And the likelihood score, $\Lambda_{j,\mathrm{RNG}}$, can be obtained using Equation 3.9.

Integration of SM and RNG is based on their likelihood scores, $\Lambda_{j,\mathrm{SM}}$ and $\Lambda_{j,\mathrm{RNG}}$, respectively. The integrated score, $\Lambda_{j,\mathrm{ALL}}$, is the square root of their product, as,

$$\Lambda_{j,\mathrm{ALL}} = \sqrt{\Lambda_{j,\mathrm{SM}} \times \Lambda_{j,\mathrm{RNG}}} \tag{3.24}$$

3.3 Solution estimation

The position solution is calculated by the weighted average of the scored positioning candidates. The score is given by the corresponding algorithm or integration method, $*$,

$$\mathbf{r}_{*} = \frac{\sum_j \mathbf{r}_j \Lambda_{j,*}}{\sum_j \Lambda_{j,*}} \tag{3.25}$$

3.4 Results evaluation

A vehicular case recorded in Hong Kong is selected to demonstrate the positioning performance of basic candidate-based 3DMA GNSS compared to conventional positioning approaches. The experiment setup follows the open-sourced dataset [92]. Ground truth reference of the dynamic experiment is provided by the NovAtel SPAN-CPT [93], a GNSS RTK/INS (fiber-optic gyroscopes, FOG) integrated navigation system. SPAN-CPT is connected to a GNSS signal splitter for a common-ground signal reception environment to other geodetic- and commercial-grade GNSS receivers.

Comparison of the positioning performance includes both conventional and candidate-based 3DMA GNSS, including:

1. NMEA: Device outputted solution in NMEA formatted string.
2. WLS: Conventional solutions using weighted least squares approach processed by open sourced library [94].
3. Cand-3DMA: candidate-based 3DMA GNSS.

Candidate sampling for the 3DMA GNSS is initial by the WLS solution as the center and the sampling radius is 40 m.

The positioning result of the vehicular experiment is shown in Table 3.1 and Figure 3.2. The device solution (NMEA) performs the best in general, as it incorporates different positioning techniques other than only GNSS. Such as the commercial GNSS receiver supports the satellite-based augmentation system (SBAS) for correcting satellite- and atmospheric-related errors. On the other hand, the smartphone positioning service, known as fused location provider, powered by Google is using different sensors and even 3DMA GNSS [6]. These factors result in the excellent positioning performance for the device outputted solution.

Table 3.1: Positioning result of the vehicular experiment with a commercial-grade receiver. (Unit: meter)

Algorithm	50^{th} percentile	RMSE	90^{th} percentile	95^{th} percentile
NMEA	2.71	3.87	5.38	7.45
WLS	5.71	12.18	17.75	30.29
3DMA GNSS	5.86	11.47	19.15	23.48

Table 3.1: Positioning result of the vehicular experiment with a commercial-grade receiver. (Unit: meter)

EKF	5.10	10.71	16.29	25.52

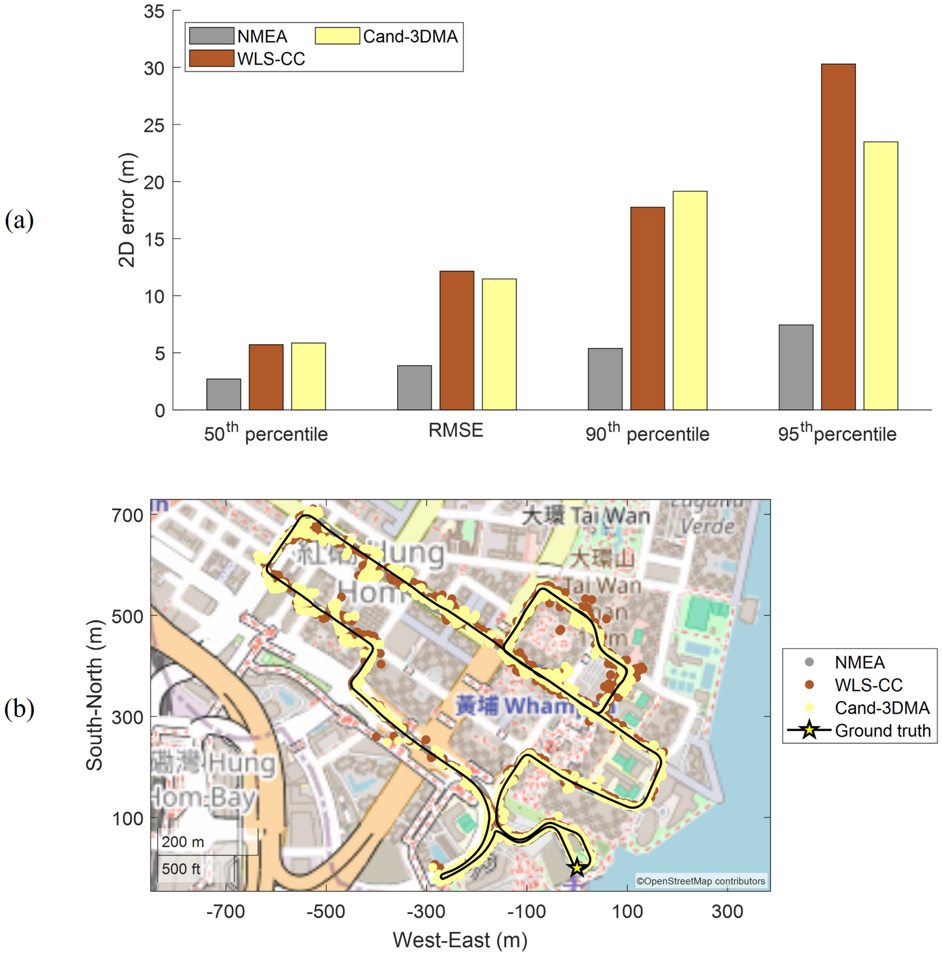

Figure 3.2: (a) Root mean square error (RMSE), 50th, 90th, and 95th percentile of the horizontal radial positioning error for the vehicular experiment across different algorithms. (b) Map plot on the positioning trajectories.

Conventional positioning error is significant that the position RMSE achieves 12.18 m and the 95-th percent of errors achieve 30.29 m. This large positioning error is mainly attributed to the NLOS reception effect in the urban canyons. Figure 3.3 (a) and (b) show the labelled pseudorange residual and signal strength on

LOS and NLOS based on the ground truth information, respectively. The labelled information shows that the signal strength of the NLOS satellite is weaker than that of the LOS one. Meanwhile, the pseudorange error is larger for the NLOS received signals, this degrades the positioning performance of the WLS.

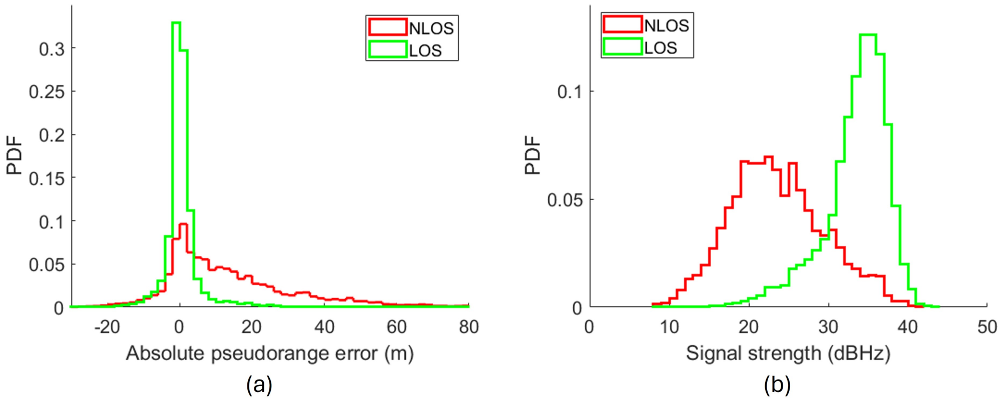

Figure 3.3: LOS and NLOS labelled (a) pseudorange residual and (b) Signal strength.

Meanwhile, 3DMA GNSS outperforms the conventional GNSS positioning approach, the position RMSE is 11.47 m. Especially when the experiment vehicle gets into the deep urban, WLS positioned the vehicle on the wrong street, but 3DMA GNSS is on the correct street.

However, several limitations of 3DMA GNSS can lead to degradation in the positioning performance; they can be separated into several aspects. Firstly, in the system initialization, candidate distribution and sampling of 3DMA GNSS are independent for each epoch. Positioning performance is subjected to the candidate distribution that is initialized by WLS. When positioning errors of WLS exceed the sampling radius, distributed candidates do not cover the actual location of the receiver. Thus, this error makes it impossible for 3DMA GNSS to locate the correct location.

Furthermore, positioning uncertainty increased due to the lack of identifiable features from GNSS measurements and surrounding building geometries. Multimodal and solution shifting are often found in the scoring surface of candidates, examples are shown in Figure 3.4(a) and (b), respectively. Multimodal, often termed as a local minimum or ambiguity problem, commonly occurs when there are limited matching features available. This leads to the emergence of multiple clusters of position hypothesis candidates with high similarity or likelihood scores. When a weighted average is employed to calculate the position solution, it tends to reside within a low-scoring region between clusters, as the estimated solution of the purple circle in Figure 3.4(a).

Solution shifting refers to the phenomenon where a position solution, influenced by numerous low-scoring candidates through weighted averaging, deviates from high-scoring regions. This issue can arise due to inaccuracies in satellite visibility predictions, erroneous measurements like multipath interference, and insufficient LOS satellites. It is important to note that this error may also manifest in the presence of multimodality. However, employing outlier detection techniques or restricting the selection to candidates with higher scores during solution computation can help alleviate some of these errors.

The integration of measurements across multiple epochs aims to enlarge the correct peak in the likelihood surface while diminishing the scores associated with incorrect peaks and their surrounding areas. Consequently, both multimodality and solution shifting effects are mitigated. However, this approach depends on knowledge of the receiver's motion between epochs, necessitating the availability of velocity measurements. Therefore, temporal velocity information becomes

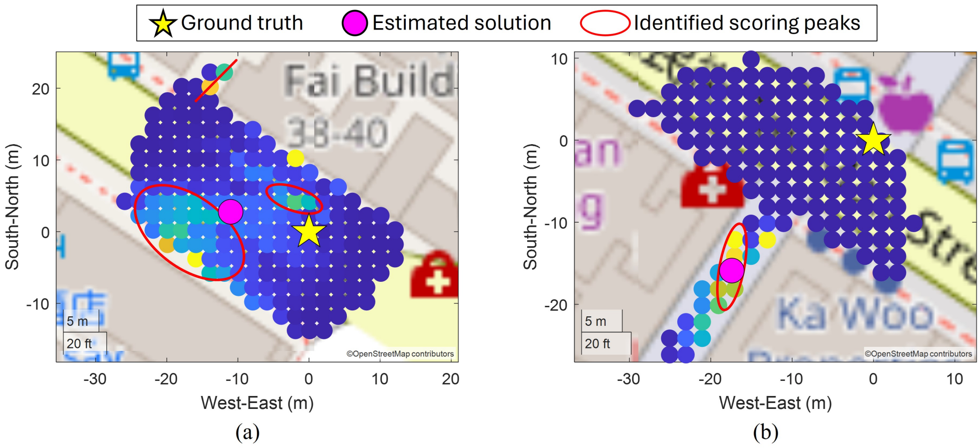

Figure 3.4: Selected example on (a) multimodal and (b) solution shifting cases.

crucial, which can be obtained through GNSS Doppler (or pseudorange rate) measurements.

Lastly, positioning epoch-wise independently results in non-smooth position estimates. From the map plot shown in Figure 3.5, the trajectory of 3DMA GNSS is not smooth with some position outliers. Therefore, connecting consecutive epochs solutions is required to improve the performance. Two benefits can be provided by integrating the velocity information, the first is mitigating the impact of position outliers, and the second advantage is providing a smoother trajectory.

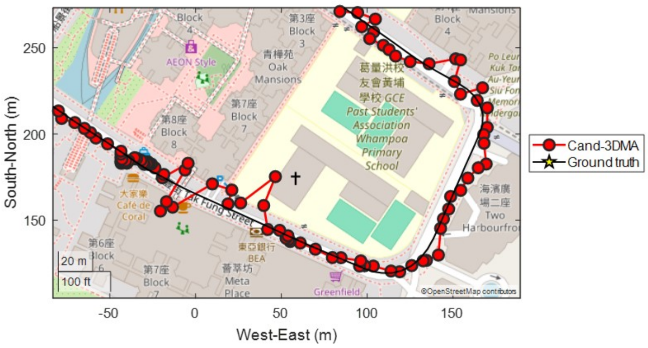

Figure 3.5: Partial positioning results of single-epoch candidate-based 3DMA GNSS.

3.5 Summary

This section presents the steps for the basic candidate-based 3DMA GNSS. The performance of candidate-based 3DMA GNSS is shown using an actual vehicular experiment recorded in Hong Kong. The positioning results show that 3DMA GNSS outperforms the conventional WLS, where position RMSE are 11.47 and 12.18 respectively.

However, some issues were identified that cause limitations or degradation in the performance of 3DMA GNSS, which can be divided into several stages. In the system initialization, candidate distribution initialized by WLS results in the distributed candidates not covering the actual location when the positioning error exceeds the sampling radius. Meanwhile, multimodal and solution shifting are found in the scoring process due to the high similarity of the building geometries or lack of distinguishing features from GNSS measurements. Lastly, independently estimating position results decreases the overall robustness and non-smoothing trajectory.

Improvement for the candidate-based 3DMA GNSS can be made in different aspects. Integrating velocity information or Doppler frequency (or Pseudorange rate) measurements to connect consecutive epochs can increase the positioning robustness. Besides, increased positioning robustness can decrease the positioning uncertainty, and the radius for candidate sampling can also be reduced to lower the computational load. Distributing candidates based on the surrounding environment can also improve the sampling efficiency. Furthermore, candidate-based 3DMA GNSS requires extra unique features for the scoring process, and this can be improved by adopting the second frequency measurements. The remaining parts are going to propose different strategies to address these limitations of candidate-based 3DMA GNSS.

Chapter 4

Improved Single Point Candidate-Based 3DMA GNSS

Chapter 3 identifies the limitations of the basic candidate-based 3DMA GNSS. Measurement and its modelling process is one of the possible improvements for the candidate-based 3DMA GNSS. This section focuses on improving the candidate-based 3DMA GNSS in this aspect. Two contributions are made in this section, introducing dual-frequency pseudorange measurements and receiver clock offset modelling.

4.1 L1- and L5-Band Measurements

C/N_0 of GNSS signals is affected differently by multipath interference, depending on their wavelengths. This property has been leveraged as a distinguishing feature to detect the multipath effect in geodetic GNSS receivers operating in urban areas [49]. L5-band measurements provide a higher accuracy on the code and carrier phase measurement [95], [96], due to its natures of a higher chipping rate and shorter wavelength [42]. As a result, it is believed that using L5-band measurements can reduce the impact of the multipath effect. Meanwhile, L5-band measurement can provide a higher accuracy for NLOS-received satellites that can isolate the NLOS reflection delays.

To maximize the satellite geometry and measurement quality of L5-band measurements, this study replaces the L1-band measurements on pseudorange, $\tilde{\rho}$, and carrier-to-noise ratio, C/N_0, with L5-band when it is available. The measured pseudorange, $\tilde{\rho}$, and carrier-to-noise ratio, C/N_0, for satellite i, are notated as ρ and $(C/N_0)^i$, respectively. They are given by,

$$\tilde{\rho}^i = \begin{cases} \rho^{i,L1} & \text{if satellite}i\text{only receives L1 band} \\ \rho^{i,L5} & \text{if satellite}i\text{receives both L1 and L5 band} \end{cases} \tag{4.1}$$

$$(C/N_0)^i = \begin{cases} (C/N_0)^{i,L1} & \text{if satellite } i \text{ only receives L1 band} \\ (C/N_0)^{i,L5} & \text{if satellite } i \text{ receives both L1 and L5 band} \end{cases} \tag{4.2}$$

Given that the chip length of the L5-band signal is ten times shorter than that of the L1-band signal, resulting in multipath errors on the L5-band measurement being ten times smaller than those on the L1-band measurement [50], this study adjust the weighting model accordingly with a tuning factor of 10 for L5-band measurements [50]. For the measurement uncertainty, τ^i, if the associated measurement is in the L5-band, the weighting is adjusted with a tuning factor of 10

[50],

$$\tau^i = \begin{cases} \tau_1^i & \text{L1 band} \\ \frac{1}{10}\left(\tau_1^i - 1\right) + 1 & \text{L5 band} \end{cases} \tag{4.3}$$

The multipath effect on L5-band measurements is significantly reduced compared to L1-band measurements due to the shorter chip length of L5 signals, which is one-tenth of the chip length of L1 signals. Therefore, the weighting assigned to L5-band measurements is increased by a factor of ten compared to L1-band measurements. Assuming identical tracking algorithms for both L1 and L5 signals, such as a non-coherent early-late power delay lock loop (DLL) discriminator, and considering thermal noise power for code-based measurements, the noise is expected to be proportional to the code length [3]. With L5 signals having a code length one-tenth that of L1 signals, the maximum noise is assumed to be ten times smaller for L5 measurements.

4.2 Receiver clock bias modelling

The receiver clock bias, δt_j, modelling significantly contributes to the uncertainty in pseudorange measurement modelling. Two commonly employed approaches to address this issue are outlined in the following sub-sections. These two common methods are extensively compared and discussed in section 4.3 to select the best receiver clock bias modelling for positioning in urban areas.

4.2.1 Single difference (SD)

Single differencing (SD) of pseudorange measurements between two satellites of the same constellation theoretically eliminates the receiver clock bias from the resulting SD measurement. Ideally, if the inter-constellation clock offset is known, only one reference satellite is needed. However, careful selection of the reference satellite is important for SD. If errors, particularly multipath and NLOS errors in urban environments, exist within the reference satellite, they will be propagated to the SD measurement. Typically, the preferred approach involves selecting the satellite with the highest elevation angle to minimize the multipath effect. Nevertheless, in dense urban settings, even the LOS satellite with the highest elevation angle may be susceptible to multipath effects. Hence, two popular methods for reference satellite selection are employed: 1) Using an algorithm considering factors such as CN0, elevation angle, and surrounding buildings to score each satellite [11], [20]. Only the satellite with the highest score is chosen as the reference satellite and is used for all sampling candidates. 2) selecting the reference satellite based on each position hypothesized candidate, allowing for variability across different candidates [12]. Note that the selected reference satellite is not limited to only GPS for the method with inter-constellation offset compensation. The single differenced pseudorange difference for i-th satellite can be expressed as,

$$\Delta\rho_j^i = \left(\tilde{\rho}^i - \tilde{\rho}^{r(i)}\right) - \left(\hat{\rho}_j^i - \hat{\rho}^{r(i)_j}\right) \tag{4.4}$$

where $*^{r(i)}$ refers to the reference satellite for the i-th satellite.

4.2.2 Weighted least squares (WLS)

In contrast to the SD method, the WLS approach does not rely on a single reference satellite. However, it is subjected to errors from all the measurements used, potentially affecting the estimation accuracy. In study [9], a receiver clock bias was estimated and applied uniformly across all positioning hypothesis candidates. Nonetheless, if this estimation is inaccurate, the simulated pseudorange is not precise for all candidates, rendering the ranging-based 3DMA GNSS less robust.

Therefore, this study proposes estimating the receiver clock delay using WLS based on the geolocation of each candidate, with the WLS only estimating the receiver clock bias. The state vector, including the receiver clock bias for different constellations, $\mathbf{x}_{\delta t_j}$, can be calculated using the following formula:

$$\mathbf{x}_{\delta t_j} = \left(\mathbf{A}^{\mathrm{T}}\mathbf{Q}^{-1}\mathbf{A}\right)^{-1}\mathbf{A}^{\mathrm{T}}\mathbf{Q}^{-1}\left(\tilde{\boldsymbol{\rho}} - \hat{\boldsymbol{\rho}}_j\right) \tag{4.5}$$

where the receiver clock delay vector $\mathbf{x}_{\delta t_j} = [\delta t_{j,GPS}, \delta t_{j,\delta GAL}, \delta t_{j,\delta GLO}, \delta t_{j,\delta BDS}]^{\mathrm{T}}$. $\delta t_{j,GPS}$ denotes the GPS receiver clock delay at candidate j; $\delta t_{j,\delta GAL}$, $\delta t_{j,\delta GLO}$, and $\delta t_{j,\delta BDS}$ represent the inter-constellation delay of Galileo, GLONASS, and Beidou between GPS, respectively. This study only uses the predicted LOS satellites on each candidate along with their corresponding pseudorange to estimate the receiver clock delay. $\mathbf{A}$ refers to the design matrix consisting flags indicating the availability of satellites from each constellation,

$$\mathbf{A} = \mathrm{c} \cdot \begin{bmatrix} 1 & b^1_{GAL} & b^1_{GLO} & b^1_{BDS} \\ \vdots & \vdots & \vdots & \vdots \\ 1 & b^i_{GAL} & b^i_{GLO} & b^i_{BDS} \end{bmatrix} \tag{4.6}$$

where c refers to the constant on the speed of light; b_*^i represents the flag to decide whether the satellite of i belongs to the $*$ constellation or not. If satellite i belongs to the $*$ constellation, value 1 is assigned; otherwise, 0 is assigned.

Available satellites are considered as one single constellation if inter-constellation bias is available. Therefore, **A** becomes a single column vector filled with the speed of light, c, with the size same as $\tilde{\boldsymbol{\rho}}$ or $\hat{\boldsymbol{\rho}}_j$.

4.3 Designed Experiments

4.3.1 Experiment Setup

Several designed experiments were conducted in urban canyons in Hong Kong using a dual-frequency L1- and L5-band measurements enabled smartphone, which is Xiaomi Mi 8. The smartphone supports GPS (L1 and L5), GALILEO (E1 and E5a), GLONASS (G1), and Beidou (B1I). Information on the designed experiments is summarized in Figure 4.1 and Table 4.1. The ground truth was manually labeled based on Google Earth, with an accuracy of approximately 1 meter in our experience. The ratio of building height to street width is calculated using $(building\_height)/(street\_width)$. A higher value indicates a narrower street surrounded by taller buildings, indicating a more challenging environment for GNSS positioning.

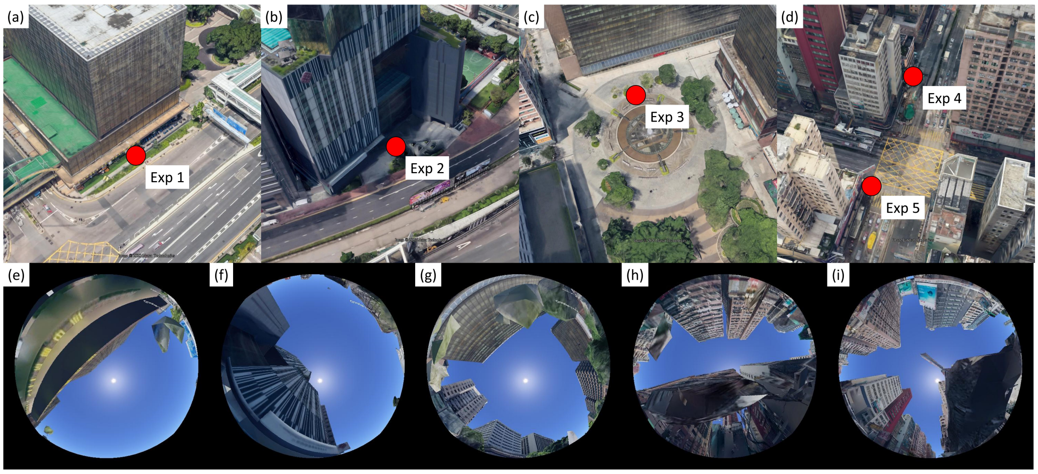

Figure 4.1: (a)-(d) Location of experiment 1 to 5, respectively. (e)-(i) Sky-pointing fisheye camera image of experiment 1 to 5, respectively.

Table 4.1: Experiment information.

Test	Environment	NLOS Reception	Multipath Effect	Mean Elevation Angle (degree)	STD Elevation Angle (degree)	Building Height to Street Width Ratio	Average No. of Satellite	Average No. of L5 Signal	No. of epoch (1Hz)
1	One side building	Light	Severe	38.07	40.01	0.93	13	2	600
2	One side building	Light	Severe	38.41	34.17	2.3	16	1	600
3	Sub-urban	Moderate	Moderate	42.60	17.52	0.68	16	6	1080
4	Deep urban	Severe	Severe	61.71	24.59	2.77	34	6	600
5	Deep urban	Severe	Severe	48.76	19.75	2.61	32	8	600

This study evaluates the measurement quality and positioning performance of a total of seven different 3DMA GNSS algorithms, Table 4.2 summarizes their information. The score mentioned above can be utilized to calculate the positioning by replacing $\Lambda_{j,*}$ in Equation 3.25.

Table 4.2: Summary on the information of different 3DMA GNSS algorihtms

3DMA GNSS algorithm	Abbreviation	Symbol of the score at j-th candidate, $\Lambda_{j,*}$	Related section or equation
1. Shadow matching [8]	SM	$\Lambda_{j,SM}$	
2. Skymask 3DMA [12]	SKY	$\Lambda_{j,SKY}$	
3. Likelihood-based ranging GNSS [11]	LBR	$\Lambda_{j,LBR}$	
4. Ranging-based 3DMA (RNG), integrate SKY and LBR	RNG	$\Lambda_{j,RNG}$	
5. Integrate SKY and SM	SKY+SM	$\Lambda_{j,SKY+SM}$	$\sqrt{\Lambda_{j,SKY} \times \Lambda_{j,SM}}$
6. Integrate LBR and SM	LBR+SM	$\Lambda_{j,LBR+SM}$	$\sqrt{\Lambda_{j,LBR} \times \Lambda_{j,SM}}$
7. Integrate all 3DMA GNSS algorithms	SKY+LBR+SM	$\Lambda_{j,SKY+LBR+SM}$	$\sqrt{\Lambda_{j,RNG} \times \Lambda_{j,SM}}$

The subsection 4.3.2 provides an analysis the quality of the L1- and L5-band pseudorange measurements for 3DMA GNSS used. In subsection 4.3.3, the performance of the methods in estimating receiver clock bias is discussed, while subsection 4.3.4 evaluates the results of 3DMA GNSS positioning. Evaluation criteria for positioning performance include root-mean-square (RMS) error, mean value, standard deviation (STD), maximum value (Max), and minimum value (Min).

4.3.2 Pseudorange quality of L1- and L5-band signals

Experiment 3 is selected as the example of pseudorange quality evaluation based on the L1- and L5-pseudorange differences. Pseudorange difference is calculated with Equation 3.8 at the ground truth (GT) location with tropospheric and ionospheric corrections, notated as $\boldsymbol{\Delta\rho}_{GT,SKY}$, that yields to $\boldsymbol{\Delta\rho}_{GT,SKY} = \tilde{\boldsymbol{\rho}} - \hat{\boldsymbol{\rho}}_{GT,SKY}$. The Figure 4.2 shows the satellites that receive both L1- and L5-band pseudorange measurements. In Figure 4.2, each entry's upper and lower rows depict the L1- and L5-band pseudorange differences for each satellite, respectively. The initial entry labelled 'Weighted AVG' denotes the weighted average pseudorange difference of all available satellites. The upper row presents the weighted average L1-band pseudorange difference, while the lower row illustrates the L5-band measurements replacing the L1-band ones. The receiver clock bias is estimated by using the weighted least-square with inter-constellation correction, as shown in subsection 4.2.2. Therefore, $\mathbf{A}$ is a single-column vector with c. The inter-constellation bias is calculated using the data recorded before the time span of the actual experiment, and it is assumed that it is unchanged over the experiment. The tropospheric and ionospheric corrections are provided by the reference station SatRef [57] by the Lands Department of Hong Kong, and noted that the pseudorange error in urban canyons should be dominated by NLOS reflection.

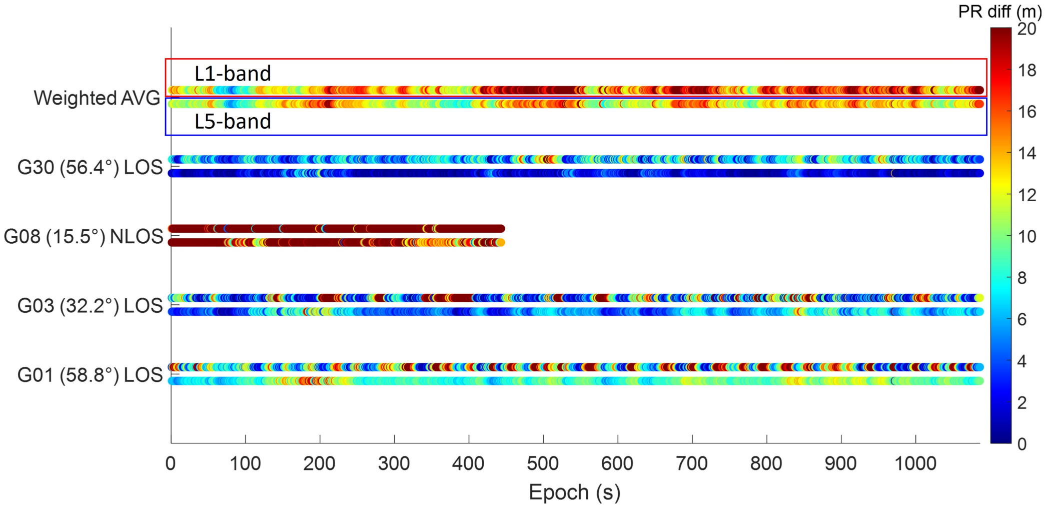

Figure 4.2: The L1- and L5-band pseudorange differences between simulated pseudoranges, as per Equation 3.8, are displayed for satellite G01, G03, G08, and G30, along with the weighted average (Weighted AVG) of all available satellites at the ground truth for Experiment 3. In each entry, the L1- and L5-band pseudorange differences are separated: the upper row is highlighted in red, while the lower row is outlined in blue. The Y-axis label indicates the satellite's ID, with the elevation angle provided within brackets, and the satellite visibility labelled as either LOS or NLOS. The color axis is confined within the range of 20m.

Figure 4.2 illustrates that the pseudorange difference using L5-band measurement is smaller than that of the L1-band, particularly noticeable for satellites with low elevation angles, such as satellite G03 and G08. Additionally, ray-tracing simulations are conducted at the ground truth location, as shown in Figure 4.3.

The simulation suggests that satellite G03 is affected by multipath. Interestingly, both G30 and G01 exhibit similar patterns to G03, although single reflections cannot be identified through ray tracing. Therefore, the analysis primarily focuses on discussing the results based on G03. Figure 4.4(a) shows the pseudorange error calculated using the double-differencing method, as explained in

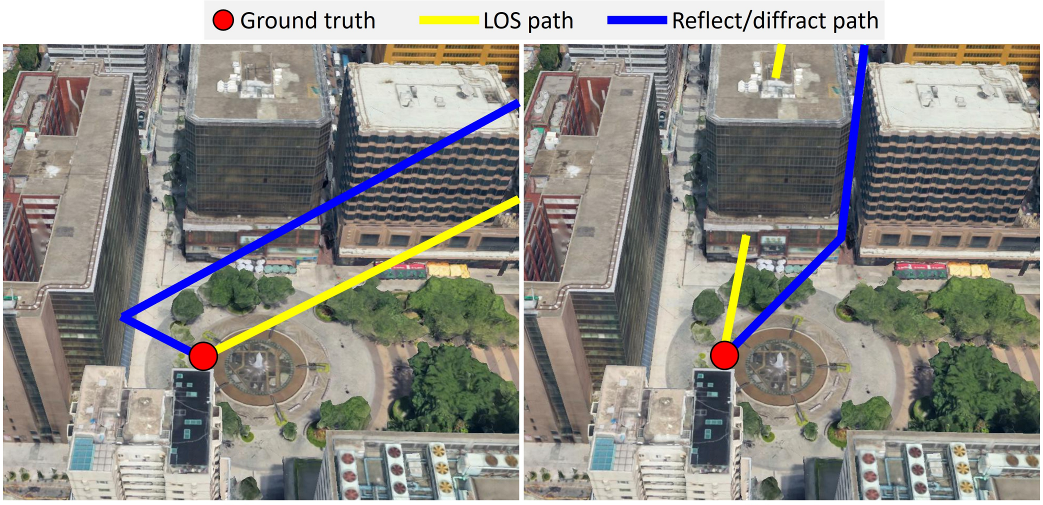

(a) G03

(b) G08

Figure 4.3: Ray-tracing results for satellite (a) G03, a multipath satellite, LOS path is not blocked, and reflection path is found; and (b) G08, an NLOS diffracted satellite, LOS path is blocked, and diffraction path is found. Red point illustrates the ground truth; the yellow line shows the LOS path; and the blue line represents the reflection/diffraction path.

Section 2.3.2 of our previous work in [97]. As previously discussed, the L5 signal operates at a higher chipping rate of 10.23 Mchip/s with a shorter wavelength, which aids in reducing waveform distortion in the correlator. Therefore, the L5 signal can achieve a higher level of accuracy in code measurements when both L1 and L5 correlators share the same early-late spacing. This characteristic is particularly beneficial in environments with numerous reflective obstacles, such as those encountered in Experiment 3, as it enables the L5 signal to effectively mitigate the multipath effect and improve positioning accuracy. Comparing the pseudorange errors, the average error for L1 is 6.32m with a standard deviation of 15.53m, whereas for L5, the average error is 1.46m with a standard deviation of 1.86m. The maximum difference between the pseudorange errors of L1 and L5 occurs at epoch 970, with the differences of 69.49m. At this epoch, the pseudorange error for L1 is 71.57m, while for L5, it is 2.08m. Throughout the entire experiment, the curves in blue representing the L5 pseudorange error exhibit less fluctuation compared to those related to L1 in red, indicating that the L5 pseudorange quality is generally better in this experiment. From the probability density distribution of L1 and L5 for satellite G03 in Figure 4.4(b), it is proven that the L5 signal demonstrates higher precision in pseudorange measurements compared to L1. As shown in Figure 4.5, the cumulative distribution function (CDF) of L1- and L5-band pseudorange errors, based on the data collected in all the experiments, further supports this observation. The 1-sigma pseudorange error of L5- and L1-band signals is approximately 11m and 20m, respectively. Considering the overall data distribution, it can be noted that 90% of the L1 signal falls within 58.3m, while the L5 signal stays within 26.8m. This confirms that the L5 pseudorange measurement is less influenced by multipath compared to L1. This characteristic is advantageous for ranging-based 3DMA GNSS, as it contributes to a more concentrated likelihood distribution of the candidates, owing to the higher consistency between the modelled and observed pseudorange.

In contrast, the G08 satellite is identified as an NLOS diffracted signal, as depicted on the right side of Figure 4.3. This explains the large pseudorange error observed for G08. It is important to note that this study assumes all NLOS receptions are reflected signals and only applies reflection correction to these satellites. However, it is important to differentiate between diffraction and reflection delays and apply distinct strategies to address these effects separately [14]. In the case of G08, its diffraction path passes through a narrow gap between two buildings, where multiple reflections may occur on these surfaces. Additionally, G08 is a satellite with a low elevation angle of about 15°, and the average C/N_0 for L1-

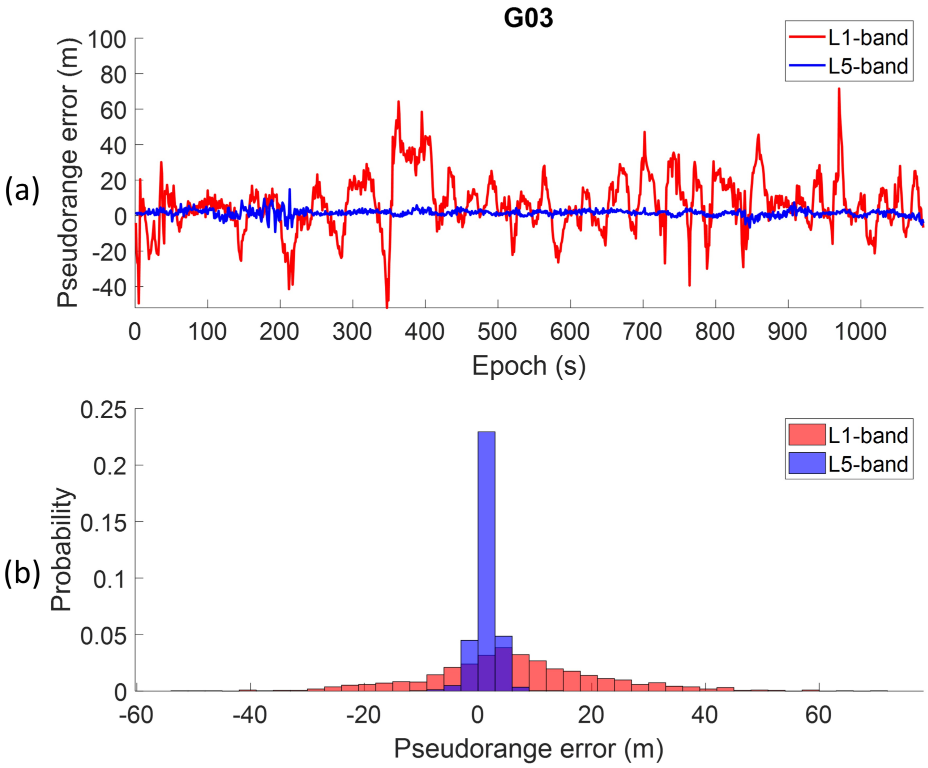

Figure 4.4: Multipath labelled satellite G03 (a) pseudorange error in the entire experiment; (b) probability density function (PDF) plot.

and L5-band measurements is 12.8 dB-Hz and 10.6 dB-Hz, respectively. Due to the low-cost design approaches, commercial receivers are typically easier to receive these complex reflected/diffracted signals. The range measurement with very weak C/N_0 can partially reflect the actual reflection interference experienced by the signal. Therefore, we cannot conclusively state that the L5 measurement of G08 has higher quality.

4.3.3 Receiver clock offset modelling

This study also discusses different receiver clock offset modelling methods in predicting the psuedorange at candidate locations. The estimation methods compared

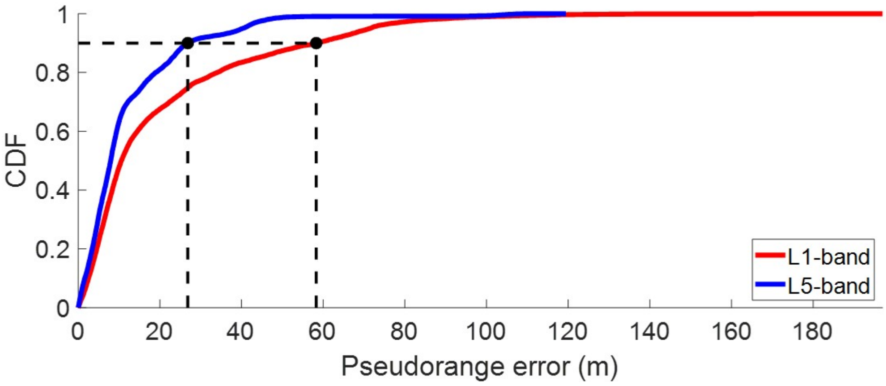

Figure 4.5: Cumulative distribution function (CDF) of L1- and L5-band pseudorange error by using the data collected in all experiments.

are:

1. SD-IC: The single difference method introduced in subsection 4.2.1. The reference satellite is selected by using a scoring algorithm ((14) in study [11]) and used for all candidates, same as [11] proposed.
2. P-SD-IC: The single difference method introduced in subsection 4.2.1. The reference satellite is selected for each candidate with the highest elevation angle [12].
3. WLS-IC: The WLS method introduced in Section subsection 4.2.2. All available satellites are used to calculate the receiver clock error [9].
4. P-WLS-IC: The proposed particle-based WLS introduced in subsection 4.2.2. Only LOS satellites are used to estimate the receiver clock error. The receiver clock offset is calculated by Equation 4.5 and Equation 4.6. Inter-constellation clock offsets are used. Hence, **A** refers to a single column vector with c.

5. P-WLS: The proposed particle-based WLS introduced in subsection 4.2.2. Only LOS satellites are used to estimate the receiver clock error. The receiver clock bias is estimated by using Equation 4.5 and Equation 4.6.

The clock offset of inter-constellations proves to be highly beneficial for improving the estimation accuracy of the receiver clock bias. Especially in scenarios where only a few satellites are received for a specific constellation with a low elevation angle, estimating an erroneous receiver clock bias for that constellation becomes a risk. To address this issue, the inter-constellation offset (IC) is estimated using measurements from the reference station 'SatRef' [57] established by the Lands Department of Hong Kong. Table 4.3 presents the RMS positioning error of Experiment 3, showcasing the effectiveness of different receiver clock error estimation methods with both L1- and L5-band measurements.

Table 4.3: 3DMA GNSS Positioning RMS error of Experiment 3 based on different receiver clock error estimation methods.

Method	Inter-constellation clock offset	Satellite selection	Candidate based	Positioning RMSE results (meter)			Average RMSE (meter)
				SKY	LBR	SKY+LBR	
1. SD-IC	√	All		12.55	12.86	10.50	11.97
2. P-SD-IC	√	LOS only	√	14.07	16.04	13.83	14.65
3. WLS-IC	√	All		11.70	12.23	11.35	11.76
4. P-WLS-IC	√	LOS only	√	12.16	11.82	10.64	11.54
5. P-WLS		LOS only	√	14.41	15.73	11.13	13.76

Method 3 yields the best positioning results for SKY, followed by Method 4 with an additional 0.46 m RMSE. Meanwhile Method 4 achieves the best positioning results for LBR. For SKY+LBR, Method 1 achieves the best positioning result, followed by Method 4 with an additional 0.1 m RMSE. When considering the average RMSE of SKY, LBR, and SKY+LBR, Methods 1, 3, and 4 all result in RMSE values within 12 m. Overall, WLS proves to be more effective for achieving better positioning results compared to SD. These findings highlight the significance of utilizing inter-constellation clock offset for improved receiver error estimation and positioning accuracy.

The RMSE values of Methods 1 and 4 are similar, but their STD and Max values exhibit differences, as shown in Table 4.4. The STD of SD is approximately 5 m, whereas that of WLS is about 4 m for SKY, indicating that WLS offers a more consistent positioning performance. This can be attributed to the fact that SD relies on a single satellite to eliminate receiver clock error through differencing with all other satellites. As a result, if an error exists in the selected reference satellite, it will accumulate across other satellites as well. On the other hand, WLS estimates the clock error using all LOS satellites, allowing errors within one satellite to be mitigated by the presence of other healthy measurements. Additionally, compared to SD on LBR, the STD error is found to be smaller by 2 m with WLS. A similar observation is found in the maximum error, where SKY with SD yields around 57 m, whereas WLS results in 42 m.

Table 4.4: Statistics of the 3DMA GNSS positioning results using Method 1 and 4 for Experiment 3. (Unit: meter)

	Method 1: SD-IC			Method 4: P-WLS-IC		
	SKY	LBR	SKY+LBR	SKY	LBR	SKY+LBR
RMS	12.55	12.86	10.50	12.16	11.82	10.64

Table 4.4: Statistics of the 3DMA GNSS positioning results using Method 1 and 4 for Experiment 3. (Unit: meter)

Mean	11.38	11.45	9.79	11.52	11.38	10.14
STD	5.30	5.86	3.80	3.90	3.21	3.24
Max	56.80	53.03	52.90	42.39	36.74	32.72
Min	4.04	4.72	0.80	1.28	6.06	0.93

An epoch in Experiment 3 is selected for a deeper analysis, as illustrated in Figure 4.6(a)-(f). Additionally, Figure 4.6(g) displays the skymask along with the CN0 value of each satellite. Observing the positioning heatmap, it's evident that SD exhibits a larger positioning error at several epochs.

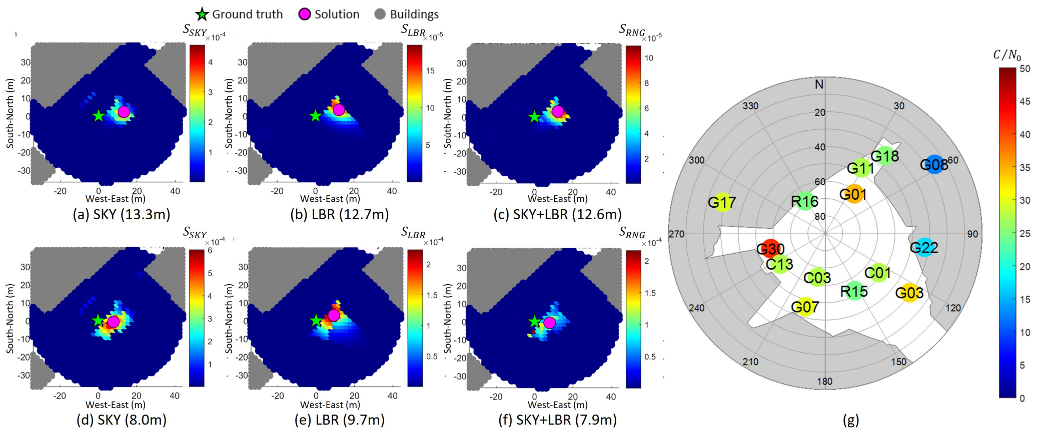

(a) SKY (13.3m) (b) LBR (12.7m) (c) SKY+LBR (12.6m)

(d) SKY (8.0m) (e) LBR (9.7m) (f) SKY+LBR (7.9m) (g)

Figure 4.6: (a)-(c) Heatmap of SKY, LBR, and SKY+LBR using Method 1, respectively. (d)-(f) Heatmap of SKY, LBR, and SKY+LBR using Method 4, respectively. (g) the skymask with satellite, colour points represent the C/N_0 value for the corresponding satellite.

Form Figure 4.6, it is noticeable that higher score particles in the SD heatmaps from (a) to (c) are more concentrated around their solution compared to the particle-based WLS ones from (d) to (f). Generally, the size of the candidate area for SD, indicated by the light blue to red regions, is smaller than that of WLS. The major axis length is approximately 10m for SD and 20m for WLS. This suggests a stable and accurate 3DMA GNSS solution for both methods [73]. However, high-score particles in SD tend to shift away from the true location compared to WLS. This error may originate from the reference satellite chosen for SD. In this study, G01 is selected as the master satellite as it has the highest elevation angle and C/N_0 across all received satellites, as shown in Figure 4.6. Although G01 has a relatively high elevation angle of more than 60°, its C/N_0 value is only about 35 dB-Hz. While ray-tracing for G01 did not identify any reflected path, there could be some multipath with destructive interference affecting the signal, leading to an estimation error for Method 1. Additionally, G01 does not have a very high elevation angle.

Figure 4.5 shows the CDF on different receiver clock error estimation methods influence the positioning error. The results indicate that methods 1, 3, and 4 generally outperform the others across most of the ranging-based 3DMA algorithms. Upon closer examination of the zoom-in plot (subfigure in Figure 4.5(d)), it becomes evident that Method 3 and 4, which involve the WLS method with inter-constellation clock offset correction, exhibit superior performance in the position domain.

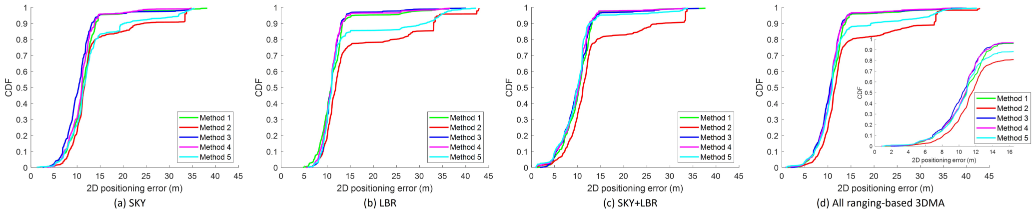

(a) SKY
(b) LBR
(c) SKY+LBR
(d) All ranging-based 3DMA

Figure 4.7: The CDF plots illustrating the 2D positioning error resulting from different receiver clock error estimation methods contribute to (a) skymask 3dma (SKY); (b) likelihood-based ranging GNSS (LBR); (c) integration of SKY and LBR (SKY+LBR); (d) combination of all ranging-based 3DMA GNSS (SKY, LBR, and SKY+LBR).

Based on the findings from Sections 4.3.2 and 4.3.3,

1. L5-band measurements have a better measurement quality and potentially

enhance the performance of 3DMA GNSS positioning, particularly in urban environments.

2. Using inter-constellation clock corrections improves the accuracy of receiver clock delay estimation, especially for ranging-based 3DMA GNSS.
3. Method 4, employing a particle-based WLS approach, demonstrates greater robustness in receiver clock bias estimation compared to other methods.

These conclusions highlight the significance of using L5-band measurements and employing effective receiver clock delay estimation methods for improved 3DMA GNSS positioning performance.

4.3.4 Positioning results

Summarized findings in subsection 4.3.3 reveal that using L5-band measurements alongside the proposed P-WLS-IC (Method 4) is anticipated to yield enhanced performance. Therefore, the positioning outcomes of the 3DMA GNSS methods are assessed using this setup. The positioning metrics for all experiments are consolidated in Table 4.5, accompanied by a graphical representation provided in Figure 4.8. Based on the short conclusions drawn above, the L5-band measurements plus the proposed P-WLS-IC (Method 4) should be able to obtain better performance. Therefore, the positioning results of 3DMA GNSS methods are evaluated based on this configuration. The positioning statistics of all experiments are summarized in Table 4.5, and a graphical view is illustrated in Figure 4.8.

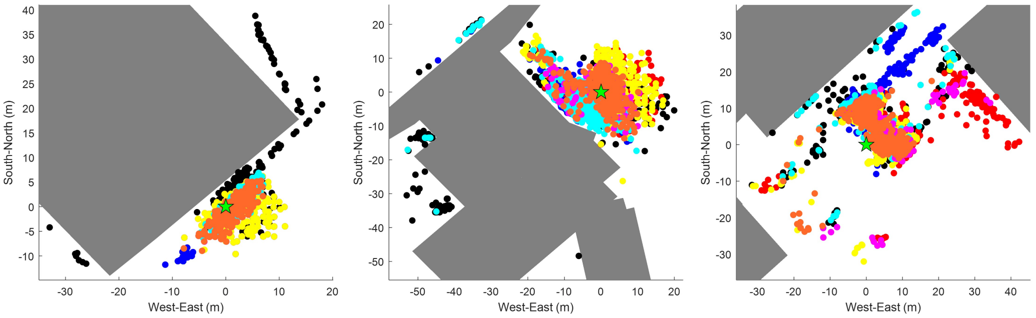

(a) Exp 1 (b) Exp 2 (c) Exp 3

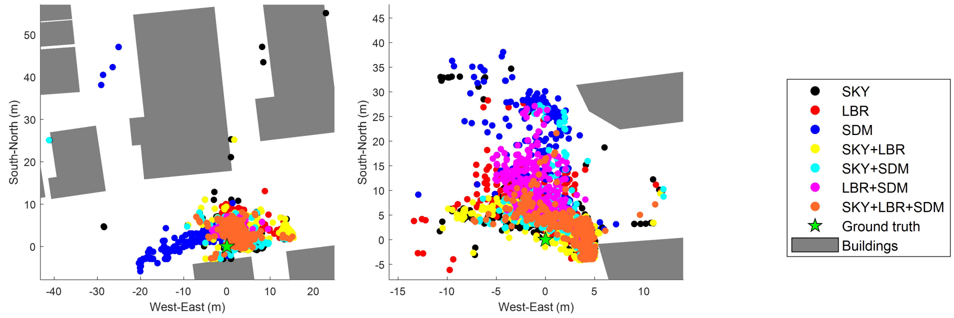

(d) Exp 4 (e) Exp 5

Figure 4.8: (a) - (e) Positioning results on Experiment 1 - 5, respectively. These 3DMA GNSS results use both L1- and L5-band measurements.

Table 4.5: Summary on the 3DMA GNSS results using L1- and L5-band measurements. (Unit: meter)

Experiment		SKY	LBR	SM	SKY +LBR	SKY +SM	LBR +SM	SKY +LBR +SM
1	RMS	19.73	3.85	12.84	3.85	4.89	3.72	3.73
	Mean	15.74	3.37	12.83	3.37	3.30	3.08	3.08
	STD	11.91	1.86	0.46	1.86	3.61	2.09	2.10
	Max	33.44	17.87	16.35	17.87	33.25	9.92	9.92
	Min	0.23	0.23	11.76	0.23	0.25	0.33	0.33
2	RMS	39.90	8.56	9.26	9.76	12.13	5.47	5.83
	Mean	34.52	7.80	7.94	8.44	8.42	4.61	4.71
	STD	20.02	3.54	4.77	4.91	8.74	2.94	3.44
	Max	64.00	21.75	45.50	26.93	57.17	15.99	22.26
	Min	0.50	1.52	0.52	1.91	0.51	0.45	0.45
3	RMS	12.16	11.82	16.09	10.64	10.76	9.69	9.17
	Mean	11.52	11.38	13.07	10.14	10.19	9.46	8.62
	STD	3.90	3.21	9.38	3.24	3.45	2.07	3.11

Table 4.5: Summary on the 3DMA GNSS results using L1- and L5-band measurements. (Unit: meter)

	Max	42.39	36.74	38.74	32.72	39.50	26.10	28.52
	Min	1.28	6.06	0.79	0.93	1.86	3.75	0.99
4	RMS	7.65	5.72	10.21	6.37	5.12	4.19	4.28
	Mean	5.86	5.12	7.56	5.31	4.40	4.08	3.87
	STD	4.92	2.54	6.86	3.53	2.61	0.94	1.83
	Max	59.64	15.74	53.34	25.25	48.23	10.34	15.34
	Min	0.39	2.00	0.12	0.44	0.20	3.01	0.23
5	RMS	7.74	9.09	22.89	5.54	7.39	11.59	5.53
	Mean	6.04	8.10	21.64	5.15	6.07	10.55	5.14
	STD	4.84	4.12	7.45	2.05	4.21	4.80	2.03
	Max	34.88	28.87	38.33	15.00	27.30	27.16	21.66
	Min	0.80	0.18	4.80	0.20	1.20	3.01	1.57

The positioning results show that the integrated solution (SKY+LBR+SM) consistently maintains an RMSE within 10m across various scenarios. Even in highly dense urban environments such as Experiments 4 and 5, this integrated approach achieves an impressive RMSE of 5m. Additionally, it is noteworthy that the SKY+LBR+SM algorithm outperforms other configurations in Experiments 1, 3, and 5 in terms of RMSE. However, in Experiments 2 and 4, the LBR+SM combination yields slightly better positioning results compared to the proposed SKY+LBR+SM approach.

In Experiment 5, the standalone positioning solutions yield RMSE values of about 8m, 9m, and 23m for SKY, LBR, and SM, respectively. However, after integration, both SKY+LBR and SKY+LBR+SM configurations achieve RMSE values within 5m. To illustrate the effectiveness of integrating SKY and LBR, the positioning heatmap for one of the epochs is shown in Figure 4.9. Initially, the high-scoring particles from SKY, LBR, and SM tend to shift away from the true location towards the intersection center. However, after integration, only the high-scoring candidate common to both SKY and LBR remains. In Figure 4.9(d), the combined SKY and LBR solution demonstrates significant improvement, with candidates near the true location maintaining high scores. Despite a large reddish area in the LBR heatmap, only candidates close to the truth location retain high scores after integration with SKY. This integration results in a positioning error of 4.7m, a substantial enhancement compared to SKY and LBR alone. Furthermore, the SM solution initially places the position on the opposite side of the street with an error of 28.3m. However, after integration with the ranging-based 3DMA algorithm, the positioning error decreases to 4.6m, as depicted in Figure 4.9(e). This integration process, using different algorithms, preserves commonly high-scoring candidates while deweighting others, thereby enhancing the positioning accuracy.

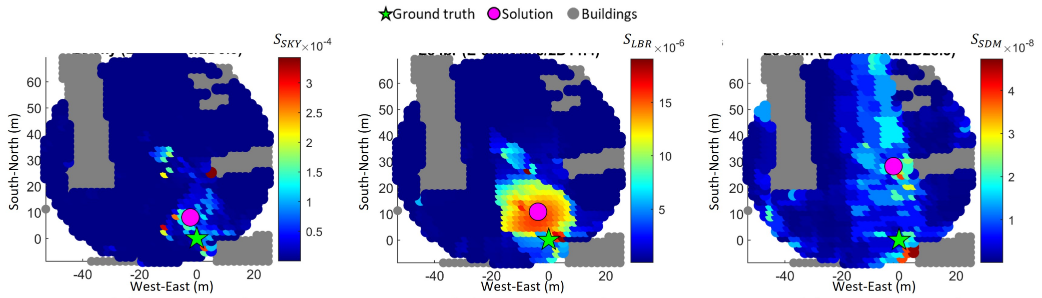

(a) SKY (8.3m) (b) LBR (11.4m) (c) SDM (28.3m)

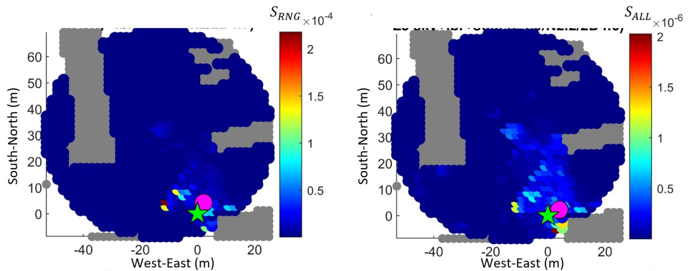

(d) SKY+LBR (4.7m) (e) SKY+LBR+SDM (4.6m)

Figure 4.9: Heatmap of Experiment 5 showing the positioning results in (a) SKY, (b) LBR, (c) SM, (d) SKY+LBR (RNG), and (e) SKY+LBR+SM. The green star marks the truth location, while the purple point indicates the positioning solution of the respective algorithm. The value inside the bracket indicates the 2D positioning error.

However, integration can sometimes lead to worse results if the standalone solutions exhibit drift. For instance, consider an epoch in Experiment 1, illustrated in Figure 4.10. The heatmap for SKY in (a) shows a noticeable shift from the ground truth, resulting in a positioning error exceeding 20m. This shift occurs because SKY only uses corrected NLOS satellites for positioning, and in this case, no correction is available for the NLOS satellites. Therefore, SKY can only rely on LOS satellites for positioning. Conversely, the heatmap for LBR in (b) concentrates around the ground truth, showcasing its excellent performance. When integrated with SKY in (d) as SKY+LBR, the combination benefits from LBR's accuracy, yielding a good positioning result. However, when integrated with SM, the heatmap becomes more scattered, as seen in (e), as SM's heatmap in (c) is dispersed along the building edge. Consequently, although the positioning result of SKY+LBR+SM is 2.7m, the high score area in the heatmap is larger than that of SKY+LBR.

The heatmap of the positioning results show that integration does not consistently lead to improved outcomes, as observed in Experiment 2. This experiment, conducted in an area with single-sided buildings, lacked corrections for NLOS satellites, limiting SKY uses only LOS satellites for positioning. As a result, the achieved positioning RMSE is approximately 40m, indicating notably poor performance. This negatively impacts the integration with other algorithms. Integration of SKY with LBR results in a larger positioning RMSE compared to LBR alone. Even when combined with SM (SKY+LBR+SM), the positioning RMSE remains high at about 5.83m. In contrast, the RMSE for LBR+SM is 5.47m, indicating a 0.4m improvement, highlighting the added uncertainty from SKY when integrated with other solutions.

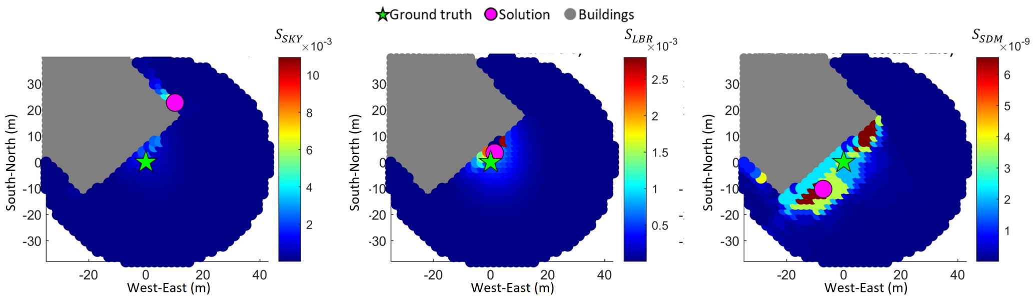

(a) SKY (24.9m) (b) LBR (3.8m) (c) SDM (12.5m)

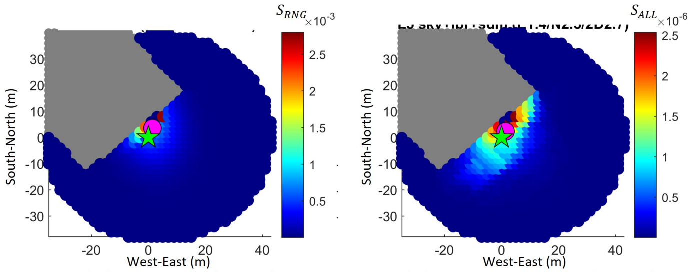

(d) SKY+LBR (3.8m) (e) SKY+LBR+SDM (2.7m)

Figure 4.10: Heatmaps for Experiment 1 in (a) SKY, (b) LBR, (c) SM, (d) SKY+LBR (RNG), and (e) SKY+LBR+SM. The green star represents the truth location, and the purple point refers to the positioning solution of the respective algorithm. The value inside the bracket denotes the 2D positioning error.

4.4 Summary

This section presents the integration of L5-band measurements into ranging-based 3DMA GNSS algorithms, alongside the estimation of receiver clock bias using a particle-based WLS method. Additionally, this section integrated shadow matching with two ranging-based 3DMA GNSS approaches: likelihood-based ranging and skymask-based methods. Through experiments conducted in urban canyons of Hong Kong, the L1-L5 3DMA GNSS demonstrated a stable positioning performance with an average accuracy of within 10m. Using L5-band measurements resulted in a noticeable improvement in positioning accuracy by reducing the pseudorange difference. As smartphones increasingly support the L5-band signal, it represents a promising avenue for future developments in urban positioning.

In regard to computational load, the current processing of 3DMA GNSS involves candidate distribution for positioning. The effectiveness of this process hinges on the precision of the initial positioning, which dictates how candidates are distributed. Ensuring that the distributed candidates adequately encompass the truth location is essential for achieving optimal solutions. In principle, computations performed for candidates located far from the truth are unnecessary. Hence, there is a need for an optimal method to determine the solution.

Chapter 5

Loosely Coupled 3DMA GNSS with Velocity using FGO

5.1 Real-Time 3D Mapping-Aided (3DMA) GNSS-Positioning System

This section proposes a loosely coupled 3DMA GNSS and velocity-positioning system using FGO. The flowchart is shown in Figure 5.1.

During the online positioning stage, 3DMA GNSS evenly disperses hypothesis positioning candidates around the initial position. Subsequently, simulated measurements are generated for comparison with the received measurements for each candidate. To enhance computational efficiency, this study integrates shadow matching and likelihood-based ranging 3DMA GNSS methodologies.

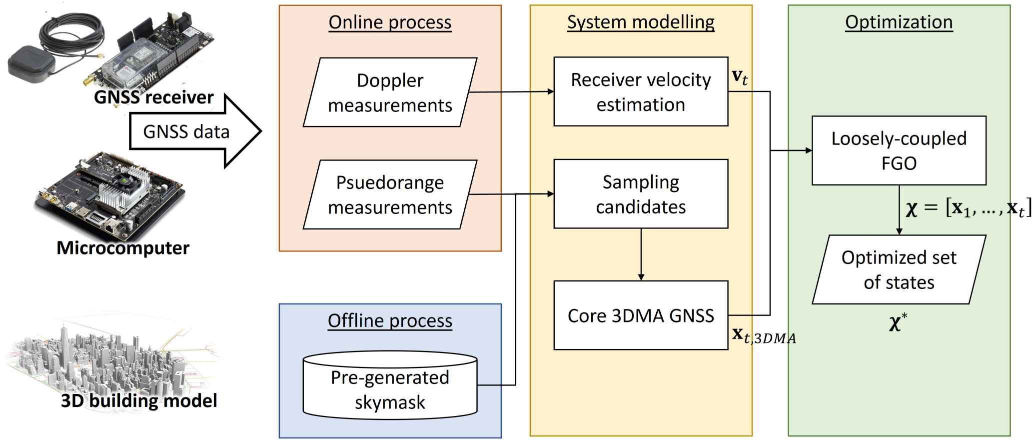

Figure 5.1: System flowchart on the proposed system.

5.2 Effective candidate distribution based on environmental context

Efficiently sampling the positioning hypothesis candidates is crucial for the performance of 3DMA GNSS. It is essential that the sampling area adequately covers the receiver location to achieve optimal performance. Increasing the sampling radius ensures coverage of the receiver location, but this also introduces a significant computational burden for low-end microcomputers, making it impractical for real-time applications. The computational time required is directly proportional to the number of sampled candidates and received satellites, and it must be within the required output rate. Therefore, this study proposes the use of surrounding skymasks and principal component analysis (PCA) to determine street direction and distribute sampling candidates effectively.

Candidate distribution is initiated with WLS for the first epoch, followed by using the previous epoch's FGO solution as the initial position once it becomes available. An initial circle with a sampling radius, says 50 m, denoted as R, is established empirically to estimate the surrounding environment through weighted averaging of the skymask, $\bar{SM}^{\psi}$.

$$\bar{SM}^{\psi} = \frac{1}{\sum_j \omega_j} \sum_j \omega_j \mathbf{SM}_j^{\psi} \text{ where } \mathbf{r}_j \in \{\|\mathbf{r} - \mathbf{r}_{init}\| < R\} \tag{5.1}$$

where $\mathbf{SM}_j^{\psi}$ represents the skymask at location $\mathbf{r}_j$ within the sampling radius R based on the initial location, $\mathbf{r}_{init}$. ψ is an array index representing the azimuth angle ranging from 0° to 359°. $w_j = \|\mathbf{r}_j - \mathbf{r}_{init}\|^{-2}$ denotes the weighting of location $\mathbf{r}_j$ based on the inverse of the distance between the initial location, $\mathbf{r}_{init}$.

The averaged skymask is then transformed into vectors in the Earth-Centered-Earth-Fixed (ECEF) frame using the transformation matrix, **R**, expressed as,

$$\mathbf{q}^{\psi} = \mathbf{R} \cdot [\sin\psi \cdot \cos\bar{SM}^{\psi}, \cos\psi \cdot \sin\bar{SM}^{\psi}] \tag{5.2}$$

where **R** is the transformation matrix that converts the vector from the local frame to the ECEF frame. Therefore, the variance-covariance matrix, **Q**, is expressed as,

$$\mathbf{Q} = \mathbf{q}^T \mathbf{q} \tag{5.3}$$

Therefore, the eigenvalues, $\lambda = \begin{bmatrix} \lambda_1 & 0 \\ 0 & \lambda_2 \end{bmatrix}$, and eigenvectors, $\mathbf{V} = \begin{bmatrix} \mathbf{v}_1 & \mathbf{v}_2 \end{bmatrix}$, can be obtained from the variance-covariance matrix, **Q**. Note that the eigenvalues and eigenvectors are sorted in descending order, where λ_1 and $\mathbf{v}_1$ denote the largest eigenvalues and eigenvectors. The eigenvector associated with a larger eigenvalue can be interpreted as representing the longitudinal direction of the street.

As a result, the initial circle can be filtered with an ellipsoid based on determined eigenvalues and eigenvectors. The length of the semi-major and semi-minor axes are denoted as R and $R \cdot {}^{\lambda_2}/_{\lambda_1}$, respectively. The direction of the semi-major and semi-minor axes are represented by v_1 and v_2, respectively.

$$\mathbf{r}_j = \left\{ \mathbf{r}_k \in \frac{(d_k \cdot \mathbf{v}_1)^2}{R^2} + \frac{(d_k \cdot \mathbf{v}_2)^2}{(R \times {}^{\lambda_2}/_{\lambda_1})^2} < 1 \right\} \tag{5.4}$$

where $d_k = \|\mathbf{r}_k - \mathbf{r}_{init}\|$ is the vector between the candidate's position, $\mathbf{r}_k$, and initial location, $\mathbf{r}_{init}$.

The distributed candidates are an ellipsoid with a semi-major axis of 50 m. The separation for each candidate is 4 m. The above settings are determined empirically and suitable for real-time processing on a low-end microcomputer used in this study. A semi-major axis of 50 m can cover the position error of the initial position in most cases. In comparison, separation with 4 m can reduce the number of distributed candidates while maintaining an acceptable accuracy level.

The proposed distribution method effectively distributes the position hypothesis candidates based on the surrounding environment. Figure 5.2 shows two typical cases observed in urban canyons. In road intersections, where two eigenvalues are nearly the same (Figure 5.2(b)), the candidate distribution forms almost a circle that covers the entire intersection, as shown in Figure 5.2(a). In contrast, when the initial location is situated on a straight street, with one eigenvalue significantly larger than the other (Figure 5.2(d)), the candidates are mostly distributed along the same street rather than extending to the next block.

Preventing candidate distribution on the next block has the potential to mitigate the local minima issue arising from the high similarity of building geometry, as shown in Figure 5.3. Local minima are situated on the next street (highlighted

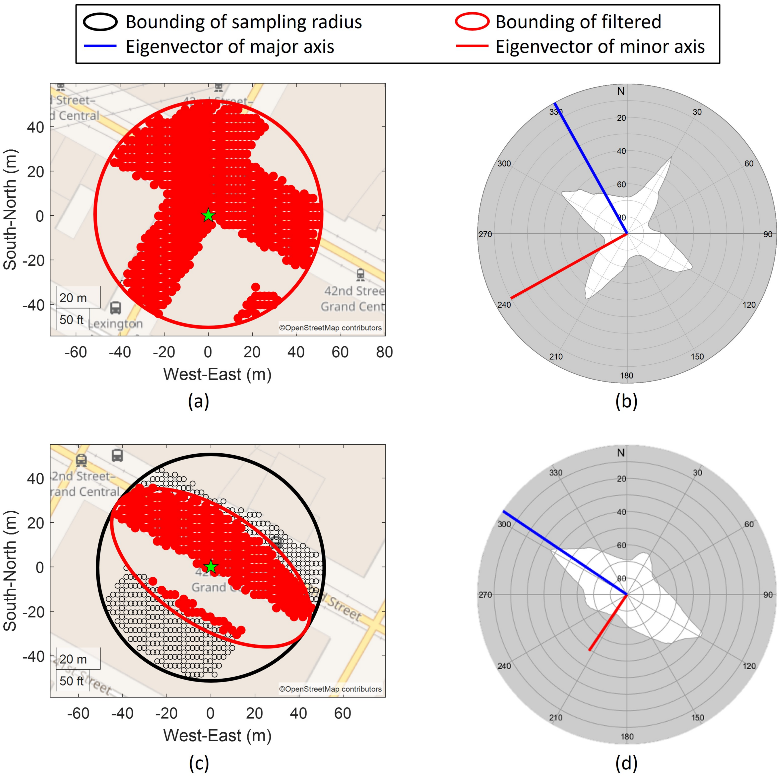

Figure 5.2: Typical cases of candidate sampling in urban environments on intersection (a,b) and straight street (c,d). Note that the eigenvectors (red and blue lines in (b,d) are projected back to azimuth and elevation angle (local frame) for illustration here.

in red near the upper right corner). However, by implementing the proposed skymask context-based candidate sampling strategy, this local minima issue can be alleviated. Furthermore, since the candidates distributed fall mainly in the same direction on the street, the initial location should be on the correct street to prevent accidentally determining the wrong block of the street.

In conclusion, the skymask context-based candidate sampling method effectively distributes position candidates, offering two key advantages. Firstly, it reduces computational load by adjusting the number of distributed candidates ac-

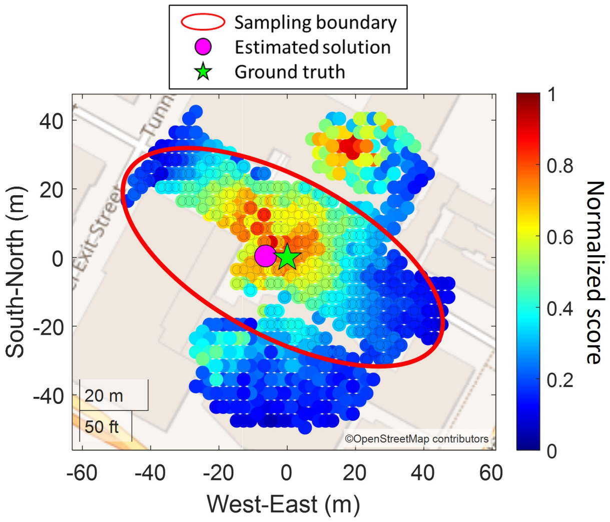

Figure 5.3: Example of skymask context−based candidates sampling.

cording to the surrounding environment. Secondly, it ensures that candidates are predominantly distributed along the same street, potentially eliminating local minima issues on adjacent streets.

5.3 Loosely-Coupled Factor Graph Optimization (LC-FGO)

This study also optimized the position solution from the candidate with context-based 3DMA GNSS as a batch through the formation of a graphical optimization framework. This framework is associated with FGO, which connects the solutions of two consecutive epochs with velocity. The overall structure of the FGO process is shown in Figure 5.4.

The error factor of 3DMA GNSS estimates the distance between the position

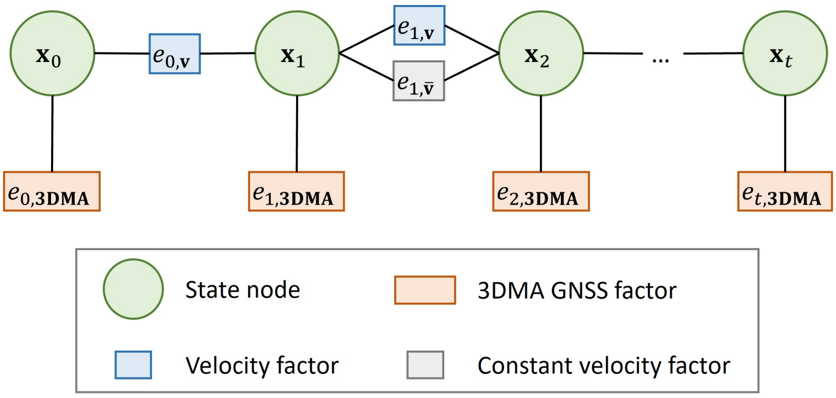

Figure 5.4: Structure of the proposed loosely-coupled 3DMA GNSS and velocity via FGO.

solution from 3DMA GNSS, $\mathbf{r}_{k,3DMA}$, and optimized state, $\mathbf{r}_k$, is given by,

$$\|e_{k,3DMA}\|^2_{\mathbf{\Sigma}^2_{k,3DMA}} = \|\mathbf{r}_k - \mathbf{r}_{k,3DMA}\|^2_{\mathbf{\Sigma}^2_{k,3DMA}} \tag{5.5}$$

where $\mathbf{\Sigma}^2_{3DMA} = \alpha \times diag([\sigma^2_{3DMA,x}, \sigma^2_{3DMA,y}, \sigma^2_{3DMA,z}])$ is a diagonal variance matrix of the 3DMA GNSS. Constant $\alpha = 1$ is an empirically determined tuning factor for the 3DMA GNSS error factor. The variance at each axis is calculated as the distance variation between the 3DMA GNSS solution and candidates with the highest 10% likelihood score, divided by the separation of candidates, γ, expressed as,

$$\mathbf{\Sigma}^2_{k,3DMA} = \frac{1}{\gamma} Var(\|\mathbf{r}_{k,3DMA} - \mathbf{r}_{k,10\%}\|) \tag{5.6}$$

where $\mathbf{r}_{k,10\%}$ represents the position of candidates with the highest 10% likelihood score. $\|\cdot\|$ denotes the Euclidean distance between two positions.

Receiver velocity, $\mathbf{v}_k$, and clock drift, $\dot{\delta t}_k$, are estimated using the Doppler measurements of every satellite i at epoch k, $\dot{\boldsymbol{\rho}}_k = [\dot{\rho}^1_k, \dot{\rho}^2_k, \cdots, \dot{\rho}^i_k]$, through the least-squares (LS) method [22]. The error factor on motion propagation estimates the difference between the displacement of consecutive epochs and the estimated velocity. It can be expressed as,

$$\|e_{k,\mathbf{v}}\|^2_{\boldsymbol{\Sigma}^2_{k,\mathbf{v}}} = \|\Delta t \times \mathbf{v}_k - (\mathbf{r}_{k+1} - \mathbf{r}_k)\|^2_{\boldsymbol{\Sigma}^2_{k,\mathbf{v}}} \tag{5.7}$$

where Δt is the time difference between epoch k and $k{+}1$. $\boldsymbol{\Sigma}^2_{k,\mathbf{v}} = \beta \times diag([\sigma^2_{k,\mathbf{v},x}, \sigma^2_{k,\mathbf{v},y}, \sigma^2_{k,\mathbf{v},z}])$ is a diagonal covariance matrix associated with the velocity $\mathbf{v}_k$ at x-, y-, and z-axis, respectively. Here, the constant $\beta = 5.2$ serves as an empirically determined tuning factor for the motion propagation error factor. Parameters α and β are determined empirically based on an open-source dataset [92] that covers various typical urban canyon scenarios. All results in this section are based on the same set of parameters. Increasing the tuning factor β brings the integrated result closer to 3DMA GNSS. Conversely, decreasing the factor below 5.0 results in much smoother optimized results, but makes it easier to observe a drift if an incorrect velocity is estimated.

A constant velocity motion model [98] is integrated into this graph structure to offer a smoothed trajectory estimation. Assuming users' motions are minimal with negligible acceleration, this factor aims to minimize the error between the position change between two epochs and the averaged velocity estimated via Doppler measurements. The output rate of the measurement and estimated velocity will affect the optimization especially a rapid steering change, this study set the output rate 1 Hz which should be sufficient for the. The model us represented as,

$$\|e_{k,\bar{\mathbf{v}}}\|^2_{\boldsymbol{\Sigma}^2_{k,\bar{\mathbf{v}}}} = \left\| \frac{\Delta t}{2}(\mathbf{v}_k + \mathbf{v}_{k+1}) - (\mathbf{r}_{k+1} - \mathbf{r}_k) \right\|^2_{\boldsymbol{\Sigma}^2_{k,\bar{\mathbf{v}}}} \tag{5.8}$$

where $\mathbf{\Sigma}_{k,\bar{\mathbf{v}}}^2 = \frac{1}{2}(\mathbf{\Sigma}_{k,\mathbf{v}}^2 + \mathbf{\Sigma}_{k+1,\mathbf{v}}^2)$ is the averaged diagonal covariance matrix at epochs k and $k+1$.

The cost function for estimating the position in the proposed loosely-coupled 3DMA GNSS through FGO is formulated as,

$$\chi^* = \arg\min_{\mathbf{x}} \sum_k \|e_{k,3DMA}\|^2_{\mathbf{\Sigma}^2_{k,3DMA}} + \|e_{k,\mathbf{v}}\|^2_{\mathbf{\Sigma}^2_{k,\mathbf{v}}} + \|e_{k,\bar{\mathbf{v}}}\|^2_{\mathbf{\Sigma}^2_{k,\bar{\mathbf{v}}}} \tag{5.9}$$

where $\chi = [\mathbf{x}_1, \mathbf{x}_2, \ldots, \mathbf{x}_k]$ represents the states set of the receiver, where χ^* denotes the optimal states set. To ensure computational efficiency, a sliding window for FGO is set at 200 s, determined empirically.

5.4 Experiments and Results

5.4.1 Experiments Setup

A commercial-grade receiver, u-blox ZED-F9P, was connected to a microcomputer, Nvidia Jetson TX2. Four satellite constellations with a single frequency were enabled during the experiments: GPS L1, GLONASS G1, Galileo E1, and Beidou B1. The output rate of the recorded data is 1 Hz, which is sufficient for Doppler measurements and estimated velocity to reflect the steering change. A modified open-source library RTKLIB [94] is adopted for the GNSS-related processes. Google Ceres Solver [99] is used for the nonlinear least squares (NLS) and FGO processes. Several experiments were conducted on the lower east side of NYC (Murray Hill, Manhattan). During these experiments, two team members followed fixed navigation routes resembling commuting between an origin (NYU Medical Center, New York City) and specific target destinations (storefronts) within a 1-mile radius. A total of 11 trips were made and used for analysis.

The ground-truth reference trajectory was obtained through post-processing. Pedestrian subjects gathering the data walked along straight lines, making efforts to maintain a steady course without deviation. Starting points, endpoints, and intermediate locations were manually labelled. Additionally, a smartphone was used during the experiment to capture device location data. This data was employed to interpolate longitudinal speed and to project vectors between the starting and ending locations.

5.4.2 Experiment Results

The evaluation aimed to compare the proposed algorithms in both real-time and post-processing scenarios, alongside several conventional solutions:

1. NMEA: receiver output solution.
2. WLS: weighted least squares method [94], uses pseudorange to estimate receiver location.
3. 3DMA GNSS: snapshot state-of-the-art 3DMA GNSS with positioning hypothesis candidates [79].
4. LC-FGO (proposed): real-time forward (instantaneous) processed loosely-coupled FGO solution with integrated 3DMA GNSS and velocity.
5. LC-FGO-PP (proposed): combined (forward and backward) processed loosely-coupled FGO solution with integrated 3DMA GNSS and velocity.

The optimization framework was conducted within the Earth-Centered-Earth-Fixed (ECEF) coordinate system. The comparison is segmented into root-meansquared error (RMSE) and standard deviation (STD) positioning errors in meters. It's important to note that both LC-FGO and LC-FGO-PP share the same graph structure. The distinction lies in LC-FGO-PP, which incorporates historical and future factors and is optimized in a combined forward and backward directions.

A total of 11 experimental navigation trips were conducted in New York City. The positioning results of these trips are summarized in Table 5.1. Overall, the candidate-based 3DMA GNSS consistently outperformed the conventional WLS method. Furthermore, the integration of velocity and optimization in the forward direction led to improved positioning accuracy. When optimizing in a combined directions manner, positioning accuracy further increased. Additionally, in most cases, FGO yielded better results compared to the receiver's output solution (NMEA). Considering the overall performance across different experiments, the RMSE and STD of 3DMA GNSS were 25.34 m and 19.46 m, respectively. Meanwhile, LC-FGO achieved an RMSE of 21.05 m and an STD of 14.60 m. LC-FGO-PP, with stronger constraints between epochs, achieved an RMSE of 15.97 m and an STD of 12.48 m. Both FGO methods demonstrated smaller RMSE values, indicating better overall performance compared to 3DMA GNSS. Additionally, the lower STD values suggest increased robustness. For further analysis, two trips out of the eleven are selected, representing both a good and bad case, respectively.

Table 5.1: Statistics on positioning results of all experiments. (Unit: m)

Navigation Trips	Epochs (s)	Algorithm	RMSE (m)	STD (m)
1	952	1. NMEA	31.09	14.47
		2. WLS	38.30	20.00
		3. 3DMA GNSS	19.70	15.51
		4. LC-FGO	24.66	14.95
		5. LC-FGO-PP	15.54	12.25

Table 5.1: Statistics on positioning results of all experiments. (Unit: m)

2	979	1. NMEA	74.81	31.57
		2. WLS	59.15	26.94
		3. 3DMA GNSS	29.14	16.75
		4. LC-FGO	33.56	17.13
		5. LC-FGO-PP	24.66	13.08
3	574	1. NMEA	19.87	7.35
		2. WLS	62.66	38.62
		3. 3DMA GNSS	27.62	16.40
		4. LC-FGO	22.98	11.04
		5. LC-FGO-PP	21.38	9.51
4	607	1. NMEA	17.20	11.08
		2. WLS	91.98	54.99
		3. 3DMA GNSS	21.08	12.26
		4. LC-FGO	13.01	6.48
		5. LC-FGO-PP	14.09	6.85
5	599	1. NMEA	29.01	7.43
		2. WLS	30.34	10.46
		3. 3DMA GNSS	22.64	13.21
		4. LC-FGO	20.38	10.25
		5. LC-FGO-PP	18.90	11.18
6	934	1. NMEA	36.89	18.01
		2. WLS	39.17	19.54
		3. 3DMA GNSS	18.27	11.28
		4. LC-FGO	15.32	10.44
		5. LC-FGO-PP	14.56	8.73
7	885	1. NMEA	33.36	15.61
		2. WLS	44.25	25.89
		3. 3DMA GNSS	18.64	11.27
		4. LC-FGO	25.17	11.03
		5. LC-FGO-PP	12.17	6.08
8	513	1. NMEA	39.09	11.05
		2. WLS	36.43	15.94
		3. 3DMA GNSS	16.55	9.46
		4. LC-FGO	21.30	8.36
		5. LC-FGO-PP	14.22	7.47
9	878	1. NMEA	24.17	10.38
		2. WLS	40.86	21.21
		3. 3DMA GNSS	41.50	26.91
		4. LC-FGO	44.62	29.99

Table 5.1: Statistics on positioning results of all experiments. (Unit: m)

		5. LC-FGO-PP	37.67	24.91
10	742	1. NMEA	36.01	16.88
		2. WLS	49.43	31.11
		3. 3DMA GNSS	26.72	15.29
		4. LC-FGO	25.49	13.08
		5. LC-FGO-PP	20.46	11.15
11	733	1. NMEA	46.78	18.12
		2. WLS	62.33	37.96
		3. 3DMA GNSS	36.85	28.13
		4. LC-FGO	37.82	27.85
		5. LC-FGO-PP	32.13	26.08

Trip 6 achieves a good positioning performance. commences in an area characterized by relatively unobstructed sky visibility and progresses along a straight path into a densely built urban canyon. These visual representations are Figure 5.5.

In this experiment, it's evident that 3DMA GNSS outperforms WLS significantly, with positioning RMSE values of 18.27 m and 39.17 m, respectively. Figure 5.5(c) shows that many WLS solutions were situated either across the street or on the wrong side entirely. 3DMA GNSS can accurately rectify the solution, correcting it back on the correct street. Further integration with Doppler measurements estimated velocity yields even more promising results, notably between epochs 200 s and 600 s, where the positioning error is notably reduced. The forward LC-FGO and combined FGO (LC-FGO-PP) yield RMSE results of 15.32 m and 14.56 m, respectively.

In contrast, Trip 2 performs worse than Trip 6. It begins in a deep urban canyon, with a walk along the street leading to a relatively open area, in stark contrast to Trip 6. The map and error plots of this experiment are depicted in Figure 5.6.

Similar to Trip 6, both 3DMA GNSS and the two LC-FGO algorithms outperform WLS. The RMSE of WLS, 3DMA GNSS, LC-FGO, and LC-FGO-PP

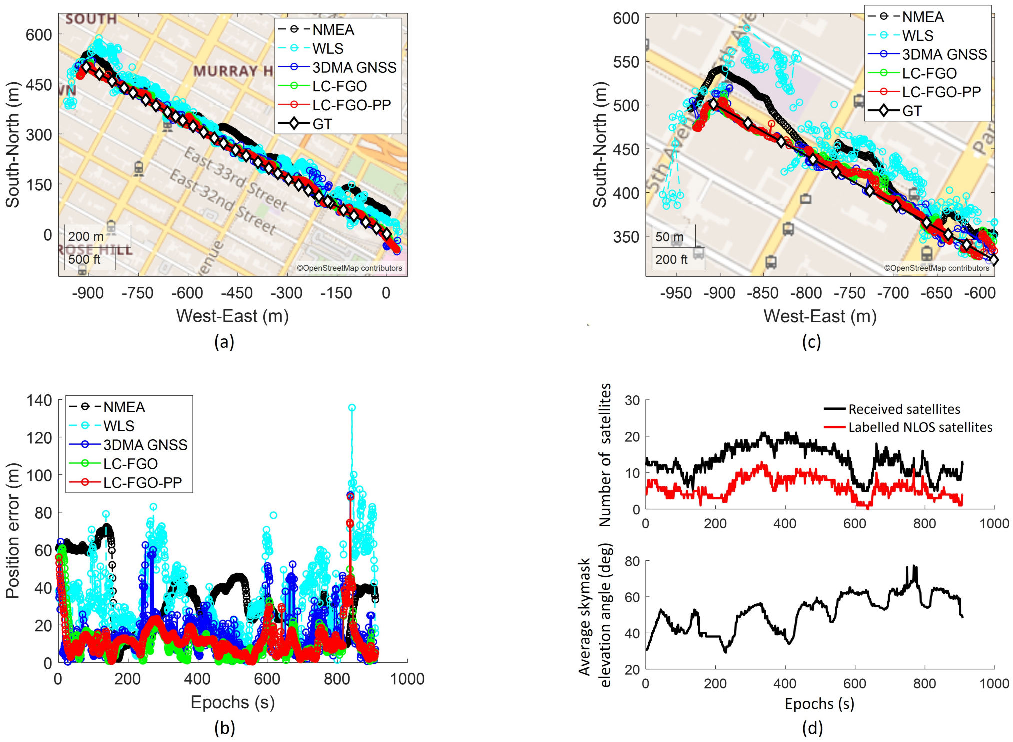

Figure 5.5: (a) map plot, (b) positioning errors, (c) magnified map plot of last 300 epochs, and (d) number of received satellites and average skymask elevation angle of good positioning trip (Trip 6).

are 59.15 m, 29.14 m, 33.56 m, and 24.66 m, respectively. However, LC-FGO performs worse than 3DMA GNSS. The overall positioning error is larger than that in Trip 6 because the environment is more complex. The average skymask elevation angle is higher in Trip 2, resulting in a more severe NLOS reception that mostly occupies a large portion of the total received satellites. The main error comes from the last 200 epochs, where the performance of 3DMA GNSS fluctuates during this period. 3DMA GNSS is a snapshot estimation, and each epoch's performance is independent of the others. However, FGO is different, especially for the forward FGO. The fluctuation of the forward FGO accumulates errors in batch optimization. Therefore, future estimation is affected. However, the com-

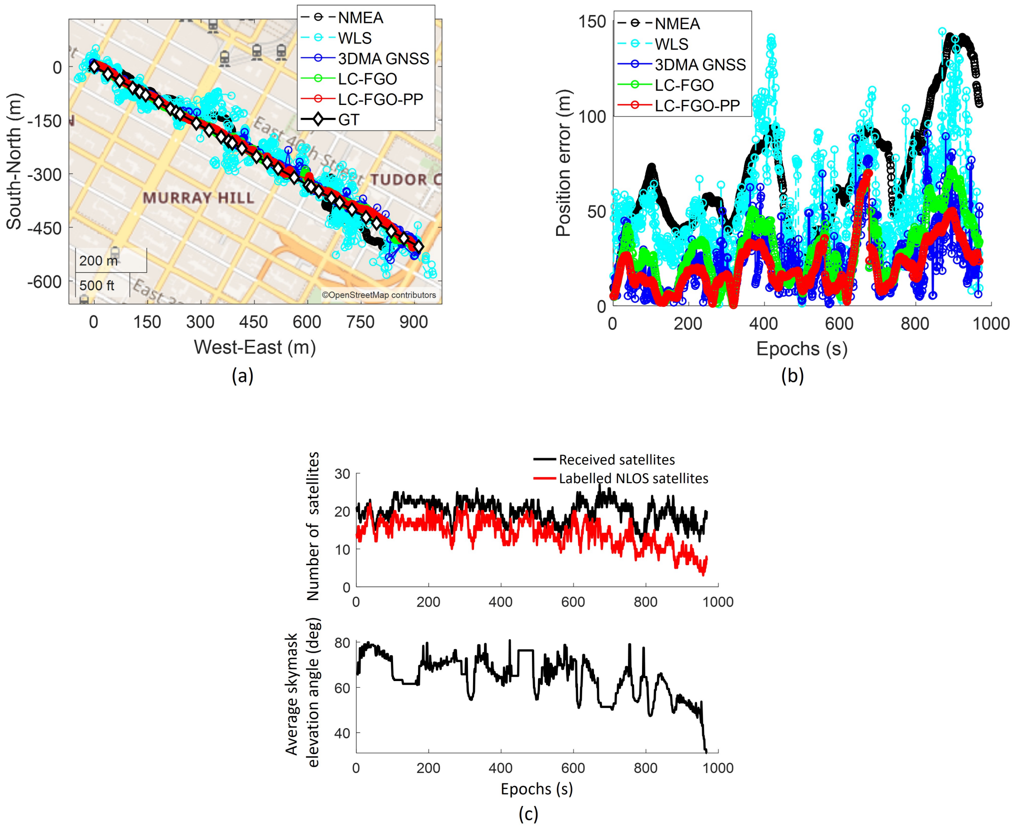

(a)

(b)

(c)

Figure 5.6: (a) map plot, (b) positioning errors, and (c) number of received satellites and average skymask elevation angle of bad positioning trip (Trip 2).

bined FGO, LC-FGO-PP, has a much stronger constraint that attempts to optimize the solution in both directions. As a result, the positioning error can be suppressed. These different natures of 3DMA GNSS and FGO result in performance variation. Therefore, to improve the performance of LC-FGO, marginalization analysis must be conducted to determine the acceptable error of this graphical problem. We must adaptively select the existing trustworthy information in the sliding window.

Towards the end of the experiment, certain 3DMA GNSS solutions inaccurately predicted the position of the next block, as depicted in Figure 5.7(a). This error occurred because the receiver was positioned in a relatively open area. The PCA analysis of the average skymask showed similar eigenvalues, indicating a lack of distinct major or minor axes. As a result, candidates were distributed in a full circle, leading to solutions being estimated at local minima, as illustrated in Figure 5.7(b). To address this issue, candidates may need to be distributed based on the user's average historical motion. However, pedestrian motion is not as consistent as that of a vehicle, making it difficult to accurately capture rapid motion changes through candidate distribution based on average motion alone. An alternative approach could involve the detection of instant motion changes using an inertial measurement unit (IMU), which could be integrated into the camera or platform more broadly.

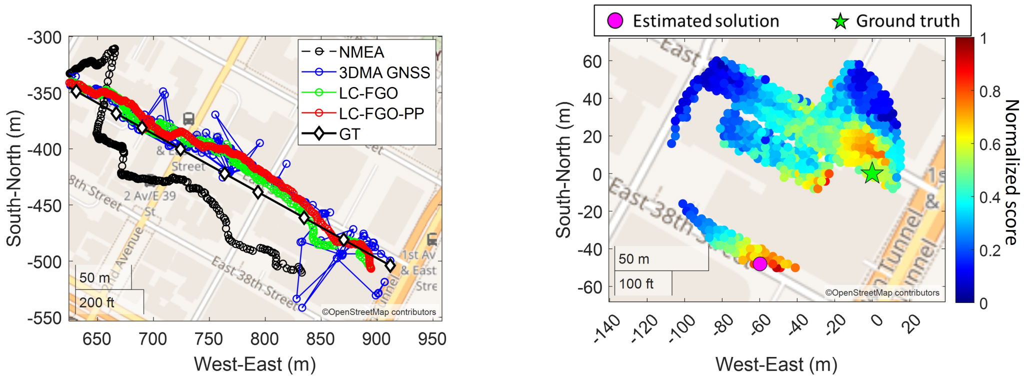

(a)

(b)

Figure 5.7: (a) Close-up map plot near the end of Trip 2. (b) Snapshot of an epoch with large position error due to local minima issues.

Trip 5 is selected to compare the positioning performance of EKF and different FGO processing strategies. The RMSE values for EKF, LC-FGO, and LC-FGO-PP are 22.38 m, 20.38 m, and 18.90 m, respectively. LC-FGO is comparable to EKF, as both are filtering approaches, but LC-FGO outperforms EKF by 2 m. This demonstrates that FGO provides more accurate positioning than EKF. It is worth noting that the implementation processes of FGO and EKF may differ, particularly in the initialization of state and covariance. For a fully fair comparison, the propagated state and covariance from EKF should be included as prior factors in the FGO optimization. Nonetheless, based on the author's observations, FGO still outperforms EKF even when these prior factors are added.

Additionally, this section also presents a vehicular case study conducted in Hong Kong using the same receiver. The experiment covers various scenarios encountered in an urban environment, ranging from open-sky areas to deep urban canyons. The data for this experiment can be accessed in [92]. Similar to the pedestrian experiments, the data is collected using the same model of receiver, which is u-blox ZED-F9P equipped with a patch antenna. The reference trajectory is provided by NovAtel SPAN-CPT [93], which integrates GNSS RTK/INS (fiber-optic gyroscopes, FOG). Positioning statistics are shown in Table 5.2, while map plots and error analyses are presented in Figure 5.8. The vehicular case study explores a wider range of scenarios across different environmental complexities and velocities, as illustrated in Figure 5.8 (c) and (d), respectively. Urban scenarios with average skymask elevation angles ranging from approximately 20 degrees to nearly 80 degrees are examined, alongside velocities from 0 m/s up to about 12 m/s.

Table 5.2: Statistics of vehicle-mounted trip results.

Algorithm	RMSE (m)	STD (m)
1. WLS	14.92	9.20
2. 3DMA GNSS	7.94	4.85
3. LC-FGO	8.09	4.55
4. LC-FGO-PP	5.80	2.95

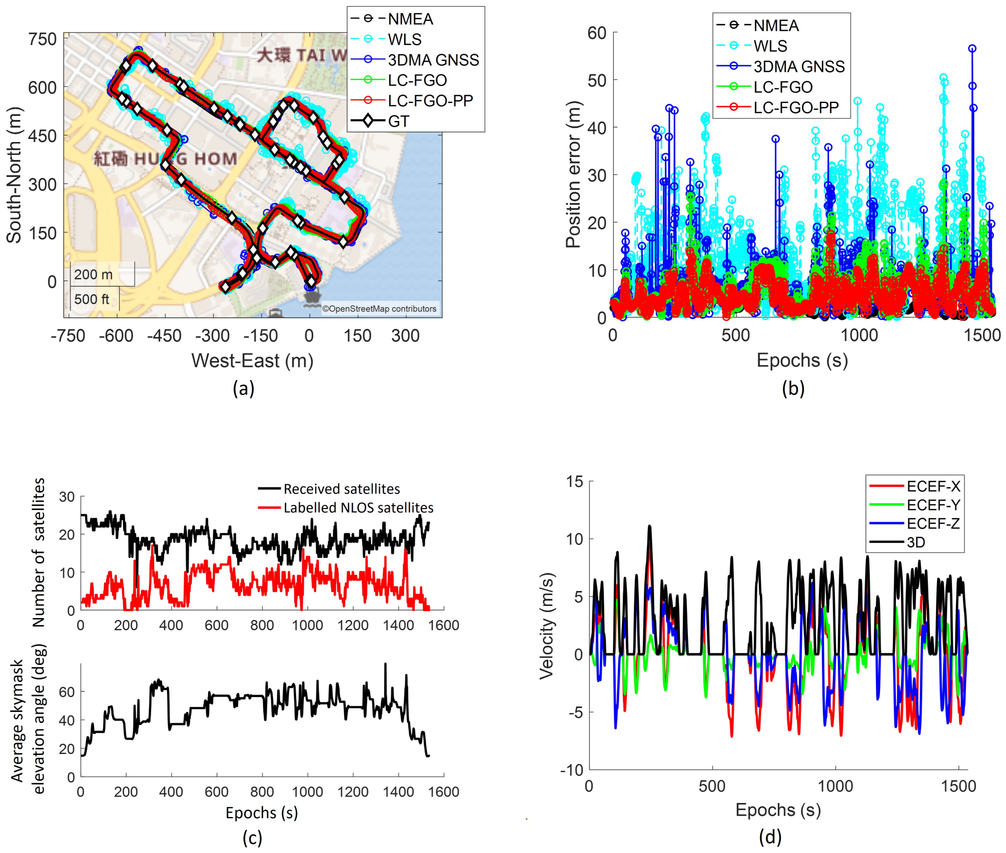

Figure 5.8: (a) zoom−in map plot near the end of Trip 2. (b) one of the epochs with large position error due to local minima problem.

In this scenario, both 3DMA GNSS and FGO demonstrated superior performance compared to WLS. The RMSE values for WLS, 3DMA GNSS, LC-FGO, and LC-FGO-PP are 14.92 m, 7.94 m, 8.09 m, and 5.80 m, respectively. Overall, the positioning accuracy exceeded that observed in New York. This exceptional performance can be attributed to two primary factors. Firstly, there was a notable difference in the local environments between New York and Hong Kong. The testing areas in New York were more urbanized, as evidenced by the average skymask elevation angles at ground truth locations, which were 58.6 degrees and 46.9

degrees for New York and Hong Kong, respectively. Secondly, the measurement noise was significantly higher in New York, likely due to variations in motion [100]. The vehicular experiment in Hong Kong experienced higher dynamic motion, and its measurements were less affected by multipath effects, resulting in better positioning performance. The pseudorange error is labelled using the double differencing technique [97] for a good case in the New York dataset (Trip 6) and Hong Kong, as illustrated in Figure 5.9. The double difference [97] requires measurements from the reference station. It involves differencing the pseudorange of satellites commonly received by both the rover and reference stations. This process eliminates common clock and atmospheric errors. The geometric distance, r, is calculated using the satellite position determined from the ephemeris, the surveyed location of the reference station, and our labelled ground truth. The reference station is located in an open-sky area, ensuring healthy measurements. Therefore, the residual can be regarded as the error attributed to the environment surrounding the receiver location. The double-difference-labelled pseudorange error of the i-th satellite, $\nabla\Delta\rho^i$, can be calculated by,

$$\begin{gathered}\nabla\Delta\rho^i = \rho^i_{rcv} - \rho^m_{rcv} - (\rho^i_{ref} - \rho^m_{ref}) - \nabla\Delta D^i \\ \text{where}\nabla\Delta r^i = r^i_{rcv} - r^m_{rcv} - (r^i_{ref} - r^m_{ref})\end{gathered} \tag{5.10}$$

where $*_rcv$ represents receiver data, while $*_ref$ stands for reference station data. $*^m$ denotes the master satellite's data, selected based on a system-specific pivot satellite approach with the highest elevation angle. ρ and D correspond to pseudorange measurement and geometric distance, respectively. Reference station data for evaluation in New York was sourced from the NYS Spatial Reference Network (NYSNet). For the evaluation of the Hong Kong dataset, reference station data was obtained from the Hong Kong Satellite Positioning Reference Station Network (SatRef) [57].

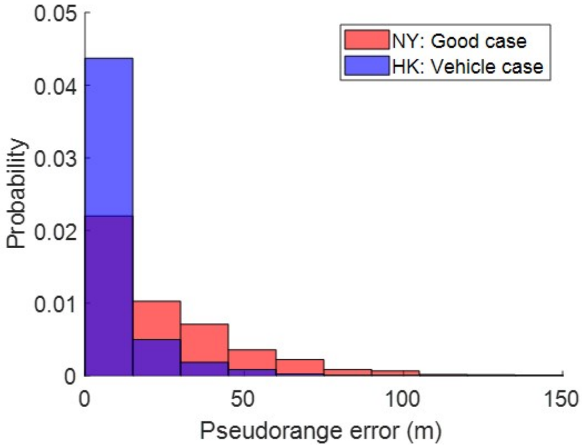

Figure 5.9: Probability density function plot on pseudorange error labelled by double differencing technique. Note that the master satellite is excluded from pseudorange error labelling, e.g., $i \neq m$ in Equation 5.10.

Pseudorange quality is higher in the Hong Kong dataset, suggesting an expectation of a better positioning performance. A comparable inference can be drawn from the outcomes of this vehicle-mounted experiment. 3DMA GNSS and LC-FGO achieve comparable performance in this dataset. However, comparing the positioning error shown in Figure 5.8(b), LC-FGO demonstrates a error reduction capabilities compared to 3DMA, resulting in a smaller standard deviation in positioning error. In other words, LC-FGO offers a smoother and more robust trajectory, a characteristic that also applies to LC-FGO-PP. However, velocity errors can degrade the integration performance. Figure 5.9 illustrates the epoch around 1300 s. Though 3DMA GNSS performing well, incorrect velocity estimates derived from Doppler measurements with WLS lead to inaccurate integrated results.

Consequently, exploring error mitigation or correction methods for Doppler measurements is necessary for future improvements. Therefore, tightly coupling these approaches with Doppler measurements could potentially address the problem.

By doing so, incorrect Doppler measurements can be identified and isolated from the state estimation separately. A sophisticated model could be developed to characterize Doppler errors, ensuring that inaccurate measurements are not used in future estimations. Meanwhile, for future work, a tighter integration of 3DMA GNSS with Doppler measurements could be achieved by representing discrete sampled locations with a continuous mathematical model.

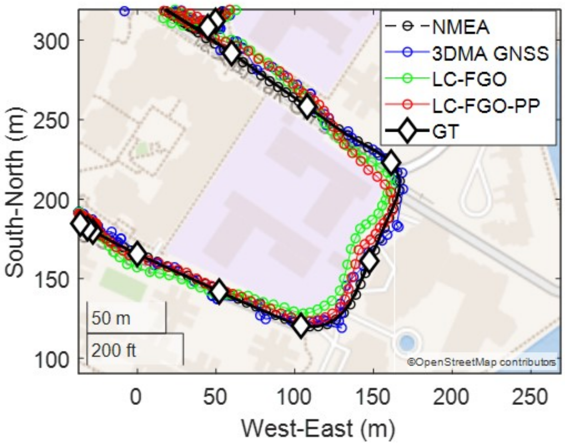

Figure 5.10: Zoom-in map plot of positioning error caused by badly estimated velocity.

5.4.3 Computational Load and Storage Requirements

One of the primary contributions of this study lies in the development of a real-time positioning system. Hence, the processing time for a single epoch solution is important for guiding real-time operations, which require maintaining an output rate of 1 Hz. The computational workload is directly linked to the number of distributed candidates (sampling radius) and available satellites. Based on the results, the average number of total received satellites (including LOS and NLOS) and sampled candidates are 26 and 1,143, respectively. The processing time for a single epoch solution is 0.91 s. This indicates that the implemented system can support real-time operations at a 1 Hz output rate. If a higher output rate is necessary, leveraging GPU technology holds significant potential for accelerating the process in real-time applications, as demonstrated in previous work utilizing GPUs for ray-tracing simulations [101] and correlation-level positioning [77].

Another critical aspect of implementing 3DMA GNSS is the format used to store information about 3D building models. Generating skymasks in real-time or online is impractical for a microcomputer. Therefore, skymasks are pre-generated offline and stored in CSV format. For instance, covering the downtown area of New York (approximately 3.6 km by 2.9 km) would require storing skymasks for a total of 812,403 locations (outside the buildings), with a 4 m separation for each candidate. The total file size for the necessary skymasks would be 1.30 GB. While this storage requirement is manageable for city-scale applications, extending the system to cover larger areas or entire states would necessitate further engineering efforts to develop a sustainable solution for skymask database implementation. Note that for a practical implementation for a large area, such as country-wise coverage, the skymasks may download based on the geofenced tile of a smaller area for better efficiency.

5.5 Summary

This section proposed a real-time positioning system integrating loosely-coupled 3DMA GNSS with Doppler measurements using FGO, alongside skymask context-based candidate sampling. This approach effectively distributes candidates and addresses local minima issues. According to experimental findings, the positioning RMSE of the loosely-coupled 3DMA GNSS with Doppler measurements via FGO averaged around 21 m, with a standard deviation of 15 m. Further performance enhancement was achieved by optimizing in a combined direction, reducing the RMSE to approximately 16 m, with a standard deviation of 13 m. Notably, FGO demonstrated a lower standard deviation error compared to candidate-based 3DMA GNSS, indicating its ability to offer a smoother and more robust solution.

Nevertheless, there is room for improvement in the performance of LC-FGO. The findings indicate that candidate-based 3DMA GNSS outperforms LC-FGO. This occurs because the positioning error of 3DMA GNSS continues to influence the integration with Doppler measurements. The accumulated error impacts subsequent batch optimization. To address this, an adaptive scheme needs to be devised to selectively prioritize high-confidence information within the sliding window.

Additionally, inaccurate Doppler measurements lead to erroneous velocity estimates, which can deteriorate the performance of FGO. Mitigating or correcting Doppler measurement errors is important for enhancing positioning accuracy. In future development, 3DMA GNSS can be more closely integrated with Doppler measurements to deliver robust positioning in urban canyons, particularly for applications in smart health and beyond.

Chapter 6

3DMA GNSS with clustering using FGO

An overview flowchart of the proposed loosely coupled 3DMA GNSS with factor graph optimisation is shown in Figure 6.1.

6.1 Candidates clustering using region growing

Region-growing [102], a technique commonly employed in image segmentation, distributed position candidates evenly across the ground, resembling the distribution of pixels in an image. This section outlines the methodology utilized in this study to detect multimodality by segregating candidates into clusters. A simplified illustration of the region-growing process is depicted in Figure 6.2.

To initiate the region-growing process, initial seed locations are required. Initially, the sampled candidates are arranged in descending order, and their cumulative scores are computed. An illustration of this process is provided in Fig-

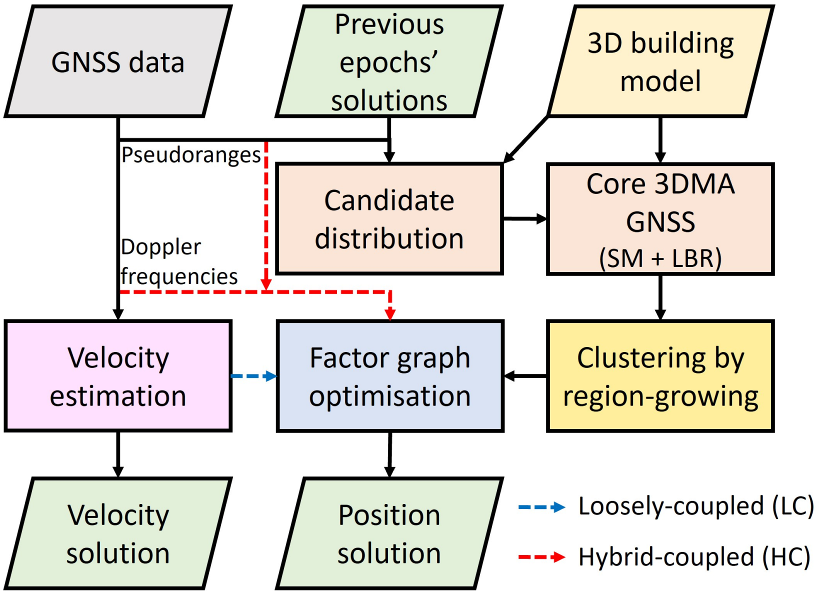

Figure 6.1: Flowchart of the proposed algorithm. (SM: shadow matching; LBR: likelihood-based ranging 3DMA GNSS)

ure 6.2(b) and (c), respectively. The seed locations are selected if the cumulative sum of the score is smaller than the threshold, α_1. Seed location selection and cluster formation occur in ascending order of the cumulative sum of the score until all non-clustered candidates have cumulative scores lower than the threshold, α_2. The threshold α_1 is determined as the sum of the scores, $K = \sum_j \tilde{\Lambda}_j$, multiplied by the constant c_1. Therefore, the selected initial seed locations have cumulative scores within the top $\mathrm{c}_1 \times 100$ percentile. This approach effectively filters out the sampled candidates with low likelihood scores. The valid growing candidates are then selected based on the cumulative sum of the score that is larger than the threshold, α_2, defined as K multiplied by the constant c_2. Similarly, the cumulative scores of the selected growing candidates fall within the top $\mathrm{c}_2 \times 100$ percentile.

In the example illustrated in Figure 6.2(d), the sorted scores represented by

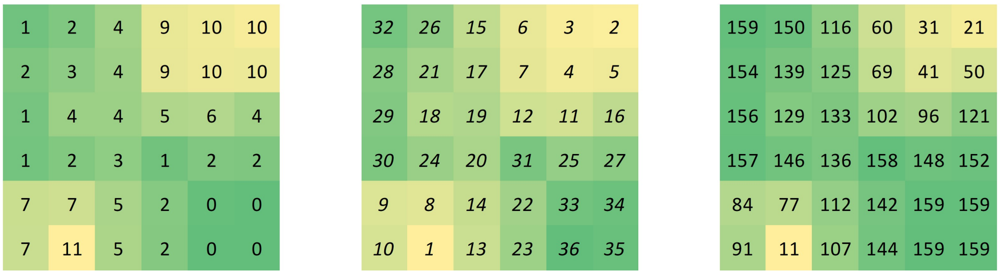

1	2	4	9	10	10
2	3	4	9	10	10
1	4	4	5	6	4
1	2	3	1	2	2
7	7	5	2	0	0
7	11	5	2	0	0

(a) Sampled candidates and scores

32	*26*	*15*	*6*	*3*	*2*
28	*21*	*17*	*7*	*4*	*5*
29	*18*	*19*	*12*	*11*	*16*
30	*24*	*20*	*31*	*25*	*27*
9	*8*	*14*	*22*	*33*	*34*
10	*1*	*13*	*23*	*36*	*35*

(b) Order of the scores in descending order

159	150	116	60	31	21
154	139	125	69	41	50
156	129	133	102	96	121
157	146	136	158	148	152
84	77	112	142	159	159
91	11	107	144	159	159

(c) Cumulative sum of the score in descending order

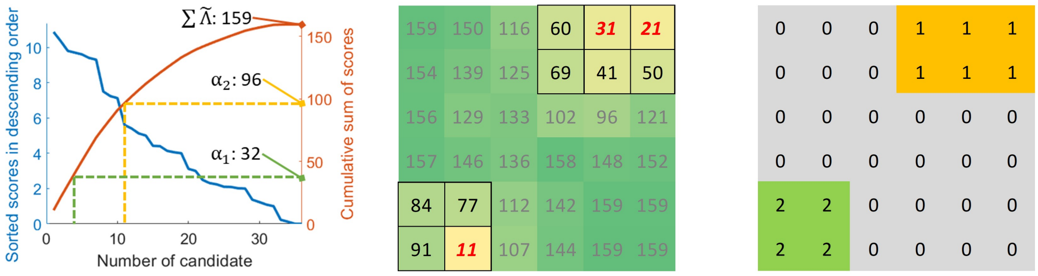

159	150	116	60	***31***	***21***
154	139	125	69	41	50
156	129	133	102	96	121
157	146	136	158	148	152
84	77	112	142	159	159
91	***11***	107	144	159	159

0	0	0	1	1	1
0	0	0	1	1	1
0	0	0	0	0	0
0	0	0	0	0	0
2	2	0	0	0	0
2	2	0	0	0	0

(d) Determined thresholds α_1 and α_2

(e) Labeled seed for region-growing (cell with red text) and valid growing candidates (black framed cells)

(f) Clustering results

Figure 6.2: A simplified example of the region-growing algorithm.

the blue curve are utilized to compute the cumulative scores shown in the brown curve, resulting in a total sum of 159. The constants c_1 and c_2 are defined as 0.2 and 0.6, respectively, while the thresholds α_1 and α_2 are set at 32 and 96, respectively. Consequently, candidates with cumulative scores lower than 96 are chosen for region-growing, as indicated by the black-framed candidates in Figure 6.2(e). On the other hand, candidates with cumulative scores lower than 32 are selected as the seed for region-growing, as denoted by candidates in red text in Figure 6.2(e). Candidates marked in grey text are excluded from subsequent processes as their scores are lower than those of the sampled candidates.

After the initial seed and growing candidates are identified, each initial seed candidate is treated as a cluster and examined to determine whether its neighbors meet two predefined criteria: 1) they are growing candidates, and 2) the distance between them is smaller than the threshold, d_1. The distance threshold, d_1, is determined empirically as 1.5 times the units of separation between the candidates. Neighbors that meet these criteria are then added to the cluster accordingly, and the growing process is iteratively repeated until all valid growing candidates have been examined. In the example depicted in Figure 6.2(f), two seed locations situated at the top right-hand corner are found to be in close proximity to each other, leading to their merger into a single cluster. The outcome reveals the discovery of two clusters.

Finally, for each identified cluster with its position candidates indexed as m, both the position, denoted as $\mathbf{r}_m$, and the covariance matrix, denoted as $\mathbf{\Sigma}_m$, can be established.

$$\mathbf{r}_m = \frac{\sum_{j'} \mathbf{r}_{j'} \times \tilde{\Lambda}_{j'}}{\sum_{j'} \tilde{\Lambda}_{j'}} \quad \text{where } j' = j \in m \tag{6.1}$$

$$\mathbf{\Sigma}_m = \frac{1}{\sum_{j'} \tilde{\Lambda}_{j'}} \sum_{j'} \tilde{\Lambda}_{j'} (\mathbf{r}_{j'} - \mathbf{r}_m)^{\mathrm{T}} (\mathbf{r}_{j'} - \mathbf{r}_m) \quad \text{where } j' = j \in m \tag{6.2}$$

6.1.1 Selection of the Cluster and Visibility Estimation

Choosing the appropriate cluster is important for determining a more accurate position solution, particularly when dealing with multimodal scenarios or solution shifting. In this study, the cluster selection process relies on the estimated position and velocity from the preceding epoch. The selected cluster denoted as m^* is chosen if its position is the nearest to the propagated position from the previous epoch. This selection can be represented as,

$$m^* = \min_{m} \|\mathbf{r}_m - (\mathbf{r}_{k-1} + \mathbf{v}_{k-1} \times \Delta t_{k,k-1})\| \tag{6.3}$$

where $\mathbf{r}_{k-1}$ and $\mathbf{v}_{k-1}$ represent the optimized position and estimated velocity at epoch $k-1$, respectively. $\Delta t_{k,k-1}$ the time difference between epochs k and $k-1$. The chosen cluster serves as a position measurement in both loosely- and hybrid-coupled FGO methods, as detailed in section 6.2.

The determination of satellite visibility can be achieved by computing the weighted average elevation angle difference between the satellite and the building boundary at the corresponding azimuth angle, denoted as β, across all candidates within the selected cluster, m^*. This computation helps determine the satellite visibility flag. If $\beta^i > 0$, LOS is assigned to the visibility flag; otherwise, NLOS is assigned for pseudorange and Doppler measurement factors. This can be formulated as,

$$\beta^i = \frac{1}{\sum_{j'} \tilde{\Lambda}_{j'}} \sum_{j'} \left\{ \tilde{\Lambda}_{j'} \times \left[\theta^i - BB_{j'}(\psi^i) \right] \right\} \quad \text{where } j' = j \in m \tag{6.4}$$

where j' represents the candidates in the selected cluster m^*. ψ^i and θ^i denote the azimuth and elevation angles for satellite i, respectively. $BB_{j'}(\psi^i)$ indicates the highest elevation angle of the building boundary at the corresponding azimuth angle ψ at candidate j'. This determined value influences the satellite visibility flag, which impacts the formulation of pseudorange factors for hybrid-coupled FGO only, as described in subsection 6.2.2, determining whether to apply likelihood-based ranging remapping for measurement innovation. Moreover, only the score from shadow matching is utilized for hybrid-coupled FGO during clustering in section 6.1 and satellite visibility estimation in Equation 6.4 to prevent measurement duplication.

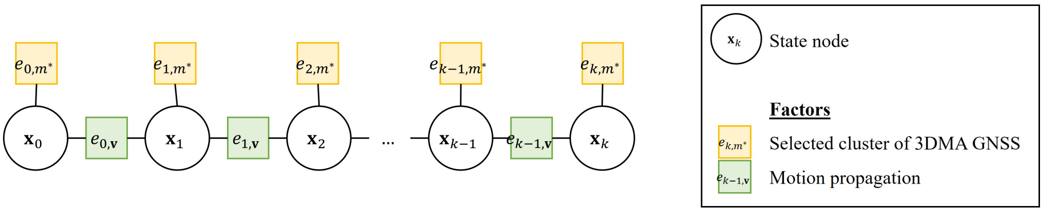

Figure 6.3: Structure of the factor graph for the proposed algorithm on loosely coupled (LC) approach.

6.2 FGO optimization

In this study, the factor graph is divided into two categories: loosely coupled and hybrid-coupled. At each epoch k, the estimated state $\mathbf{x}_k$ comprises the receiver's position $\mathbf{r}_k$ and the receiver clock offset δt_k, forming the state set $\chi = [\mathbf{x}_1, \mathbf{x}_2, \cdots, \mathbf{x}_k]$.

6.2.1 Loosely-coupled (LC)

In the loosely-coupled (LC) FGO, error factors are incorporated for both the position of the selected cluster and motion propagation. The cluster position factors provides constraints on the position solution for the respective epoch, while motion model factors estimate the displacement between consecutive epochs. The factor graph's layout is depicted in Figure 6.3.

The position factor of the chosen cluster loosely estimates the separation between the receiver's position, $\mathbf{r}_k$, and the position of the selected cluster, $\mathbf{r}_{m^*}$. This factor can be formulated as,

$$\|e_{k,m^*}\|^2_{\mathbf{\Sigma}^{-1}_{k,m^*}} = \|\mathbf{r}_k - \mathbf{r}_{m^*}\|^2_{\mathbf{\Sigma}^{-1}_{k,m^*}} \tag{6.5}$$

where Σ_{k,m^*} represents the covariance matrix of the selected cluster computed using Equation 6.2 multiplied by the tuning factor c_3.

The motion propagation factor is integrated into the factor graph. It links the positions of two successive epochs and minimizes the differences between the optimized position displacement and the estimated velocity from Doppler measurements. This factor can be expressed as,

$$\|e_{k,\mathbf{v}}\|^2_{\boldsymbol{\Sigma}^{-1}_{k,\mathbf{v}}} = \|(\mathbf{r}_{k+1} - \mathbf{r}_k) - \Delta t \times \mathbf{v}_k\|^2_{\boldsymbol{\Sigma}^{-1}_{k,\mathbf{v}}} \tag{6.6}$$

where $\boldsymbol{\Sigma}_{k,\mathbf{v}}$ is the covariance matrix of the velocity estimated using WLS.

As a result, the FGO for LC 3DMA GNSS with clustering is formulated,

$$\chi^*_{LC} = \arg\min_{\chi} \sum_k \left\{ \|e_{k,m^*}\|^2_{\boldsymbol{\Sigma}^{-1}_{k,m^*}} + \|e_{k,\mathbf{v}}\|^2_{\boldsymbol{\Sigma}^{-1}_{k,\mathbf{v}}} \right\} \tag{6.7}$$

where χ^*_{LC} represents the optimal estimate of the state set of LC FGO.

6.2.2 Hybrid-coupled (HC)

Hybrid-coupled FGO combines the error factor on the position of the selected cluster in a loose manner and tightly integrates error factors on Pseudorange and Doppler frequency measurements. The factor graph's structure is depicted in Figure 6.4.

Every pseudorange factor estimates the state on position and receiver clock offset by minimizing the residual between the measured pseudorange and the predicted pseudorange with a given state, which is similar to measurement innovations in likelihood-based ranging 3DMA GNSS. Depending on the determined visibility, the pseudorange measurement innovation is remapped by likelihood-

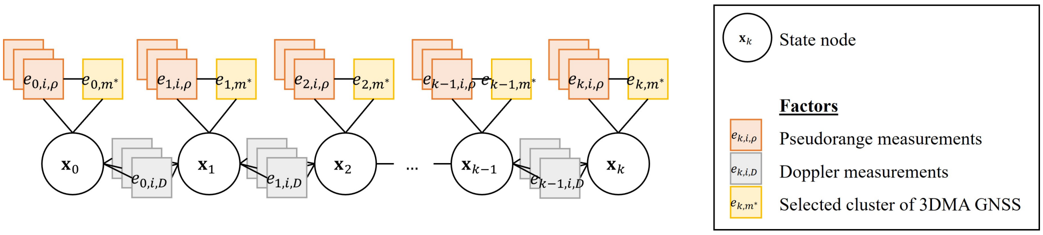

Figure 6.4: Structure of the factor graph for the proposed algorithm on hybrid-coupled (HC) approach.

based ranging 3DMA GNSS, denoted as $\delta z^i(\mathbf{x}_k)$. The pseudorange measurement factor can be represented as,

$$\|e_{k,i,\rho}\|^2_{\sigma^{-1}_{k,i,\rho}} = \left\|\delta z^i(\mathbf{x}_k)\right\|^2_{\sigma^{-1}_{k,i,\rho}} \tag{6.8}$$

where $\sigma^{-1}_{k,i,\rho}$ is the error standard deviation of the corresponding pseudorange measurement which is calculated by Equation 3.15 times the tuning constant c_4. The measurement innovation, $\delta z^i(\mathbf{x}_k)$, is expressed as,

$$\delta z^i(\mathbf{x}_k) = \begin{cases} \tilde{\rho}^i_k - \hat{\rho}^i(\mathbf{x}_k) & LOS \\ \mathrm{LBR}\left(\tilde{\rho}^i_k - \hat{\rho}^i(\mathbf{x}_k)\right) & NLOS \end{cases} \tag{6.9}$$

where $\mathrm{LBR}(\cdot)$ is the function to remap the measurement innovation that is assumed to be NLOS to LOS. The visibility flag, LOS or NLOS, is determined using Equation 6.4. Corrected NLOS included in the FGO structure can preserve an acceptable DOP for positioning. Furthermore, the NLOS-corrected pseudorange is also used as an extra feature in this structure, as it is diverse across different locations.

Similarly, each Doppler frequency measurement factor optimizes the state by minimizing the disparity between the Doppler frequency measurement, represented as $\tilde{\dot{\rho}}^i$, and the modelled Doppler frequency, denoted as $\hat{\dot{\rho}}^i(\mathbf{x}_k)$. However, to model the Doppler frequency for NLOS signals, an accurate reflecting point is needed to estimate the LOS unit vector from the receiver to the reflecting point. Therefore, only the LOS Doppler frequency measurements are employed in the FGO. The LOS Doppler measurements are modelled as,

$$\lambda^i \hat{\dot{\rho}}^i(\mathbf{x}_k) = (\mathbf{v}_k - \mathbf{v}^i) \cdot \mathbf{u}_k^i + \mathrm{c} \times (\dot{\delta} t_k^i - \dot{\delta} t_k) \tag{6.10}$$

where λ^i is the wavelength of the measurement. $\mathbf{v}_k = (\mathbf{r}_{k+1} - \mathbf{r}_k)/\Delta t$ and $\dot{\delta} t_k = (\dot{\delta} t_{k+1} - \dot{\delta} t_k)/\Delta t$ are velocity and clock drift of the receiver, respectively. δt is the time difference between epochs k and $k+1$. $\mathbf{v}^i$ and $\dot{\delta} t_k^i$ are the velocity and clock drift of the satellite provided by the ephemeris. $\mathbf{u}_k^i$ is the LOS unit vector from the satellite to the receiver.

As a result, the error factor of the Doppler frequency measurement is expressed as,

$$\|e_{k,i,\dot{\rho}}\|^2_{\sigma^{-1}_{k,i,\dot{\rho}}} = \left\|\lambda^i \tilde{\dot{\rho}} - \lambda^i \hat{\dot{\rho}}(\mathbf{x}_k)\right\|^2_{\sigma^{-1}_{k,i,\dot{\rho}}} \tag{6.11}$$

where $\sigma^{-1}_{k,i,\dot{\rho}} = 0.01 \times \sigma^{-1}_{k,i,\rho}$ is the error standard deviation of Doppler frequency measurement. This study empirically assumes it is 100 times smaller than that of pseudorange measurement.

Finally, the Hybrid coupled (HC) 3DMA GNSS with clustering is formulated,

$$\chi^*_{HC} = \arg\min_{\chi} \sum_k \left\{ \|e_{k,m^*}\|^2_{\boldsymbol{\Sigma}^{-1}_{k,m^*}} + \sum_i \|e_{k,i,\rho}\|^2_{\sigma^{-1}_{k,i,\rho}} + \sum_i \|e_{k,i,\dot{\rho}}\|^2_{\sigma^{-1}_{k,i,\dot{\rho}}} \right\} \tag{6.12}$$

where χ^*_{HC} denotes the optimal estimate of the state set of hybrid-coupled FGO.

6.2.3 Operation modes of FGO

The optimization results can be delivered in either forward or combined modes, depending on the application requirements. In the forward mode, snapshot optimization is performed, estimating the current states whenever new measurements are fed into the optimizer. It uses historical states and measurements to impose prior constraints. This forward FGO resembles Bayesian estimation algorithms like the grid filter, conducting step propagation and measurement update steps whenever new measurements arrive. Although operating in this mode can decrease the computational burden compared to optimization in combined directions, it may be less robust due to the absence of future measurements to refine the estimation.

On the other hand, the combined mode involves estimating all states by incorporating all input measurements in both forward and backward directions. Each optimizer execution outputs and replaces all historical results. Optimizing in both directions represents the most effective strategy for post-processing, as it uses the states from all available epochs. This approach ensures optimal estimates of the states across all epochs.

6.3 Designed experiment

6.3.1 Experiment setup

Vehicular recorded GNSS data is selected to evaluate the positioning performance of 3DMA GNSS with clustering and hybrid integrated FGO. The experiment setup is identical to the setup introduced in section 3.4.

The recorded datasets are post-processed and the following algorithms are compared:

1. NMEA: Device outputted solution in NMEA formated string
2. WLS: Single-epoch conventional GNSS with outlier detection [34]
3. Single epoch 3DMA GNSS: Single-epoch candidate-based 3DMA GNSS without clustering
4. EKF: loosely-coupled WLS and Doppler frequency estimated velocity using extended Kalman filter (EKF) [16]
5. EKF 3DMA GNSS: loosely-coupled WLS and Doppler frequency estimated velocity using extended Kalman filter (EKF)
6. LC-FWD FGO 3DMA GNSS: Loosely-coupled (LC) forward (FWD) FGO on 3DMA GNSS
7. LC-CMB FGO 3DMA GNSS: Loosely-coupled (LC) combined (CMB) FGO on 3DMA GNSS
8. LC-FWD FGO 3DMA GNSS-C: Loosely-coupled (LC) forward (FWD) FGO on 3DMA GNSS with clustering using region growing
9. LC-CMB FGO 3DMA GNSS-C: Loosely-coupled (LC) combined (CMB) FGO on 3DMA GNSS with clustering using region growing
10. HC-FWD FGO 3DMA GNSS: Hybrid-coupled (HC) forward (FWD) FGO on 3DMA GNSS
11. HC-FWD FGO 3DMA GNSS: Hybrid-coupled (HC) combined (CMB) FGO on 3DMA GNSS

12. HC-FWD FGO 3DMA GNSS-C: Hybrid-coupled (HC) forward (FWD) FGO on 3DMA GNSS with clustering using region growing
13. HC-CMB FGO 3DMA GNSS-C: Hybrid-coupled (HC) combined (CMB) FGO on 3DMA GNSS with clustering using region growing

The 3DMA GNSS with clustering requires temporal information to select the best cluster, so only the multi-epoch positioning methods are involved in the comparison.

6.3.2 Experiment results

Table 6.1 and Figure 6.5(a) presents statistical metrics and histograms illustrating the horizontal radial positioning error, including the root mean square error (RMSE) and errors at the 50th, 90th, and 95th percentiles across all static experiments. Figure 6.5(b) provides visual representations of these errors.

Table 6.1: Statistics of vehicular experiment across different algorithms. RMSE: root mean square error. (Unit: meter)

Algorithm	50^{th} percentile	RMSE	90^{th} percentile	95^{th} percentile
NMEA	2.71	3.87	5.38	7.45
WLS-CC	5.71	12.18	17.75	30.29
Single epoch 3DMA GNSS	5.86	11.47	19.15	23.48
EKF	5.10	10.71	16.29	25.52
EKF 3DMA GNSS	4.92	9.52	15.24	20.43
LC-FWD FGO 3DMA GNSS	4.27	8.62	16.29	17.58
LC-CMB FGO 3DMA GNSS	4.28	7.06	11.31	17.59
LC-FWD FGO 3DMA GNSS-C	5.25	8.58	14.74	16.52

Table 6.1: Statistics of vehicular experiment across different algorithms. RMSE: root mean square error. (Unit: meter)

LC-CMB FGO 3DMA GNSS-C	4.96	6.92	11.29	13.78
HC-FWD FGO 3DMA GNSS	4.19	7.46	13.31	16.08
HC-CMB FGO 3DMA GNSS	4.31	5.79	8.94	11.31
HC-FWD FGO 3DMA GNSS-C	5.22	8.19	13.78	16.21
HC-CMB FGO 3DMA GNSS-C	4.99	6.99	11.29	13.76

In general, the single-epoch conventional approach demonstrates the lowest positioning accuracy, with an RMSE nearing 12 m. Single-epoch 3DMA GNSS observes a slight improvement in positioning accuracy to approximately 11.5 m. The FGO-based approaches notably reduce the RMSE to below 10 m.

Connecting consecutive epoch solutions notably improves positioning performance. By loosely integrating position solutions from WLS with estimated velocity, the RMSE is reduced by nearly 1 m for EKF. Replacing the position solution from 3DMA GNSS, the RMSE decreases to around 9.5 m. Meanwhile, the 95th percentile error decreases from around 23.5 m for single epoch 3DMA GNSS to 20.4 m for EKF 3DMA GNSS. This indicates that while 3DMA GNSS provides more accurate absolute positions, connecting multi-epoch solutions using velocity can enhance robustness. Furthermore, comparing the positioning performance of EKF 3DMA GNSS with forward-optimized FGOs, only forward-optimized FGOs are considered due to their similar estimation strategy to EKF in terms of system propagation and update. Comparing the positioning performance of EKF and FGO-FWD, FGO approaches generally outperform the EKF approach. The RMSE is reduced from around 9.5 m for EKF to 8.5 m or less in FGOs. This demonstrates

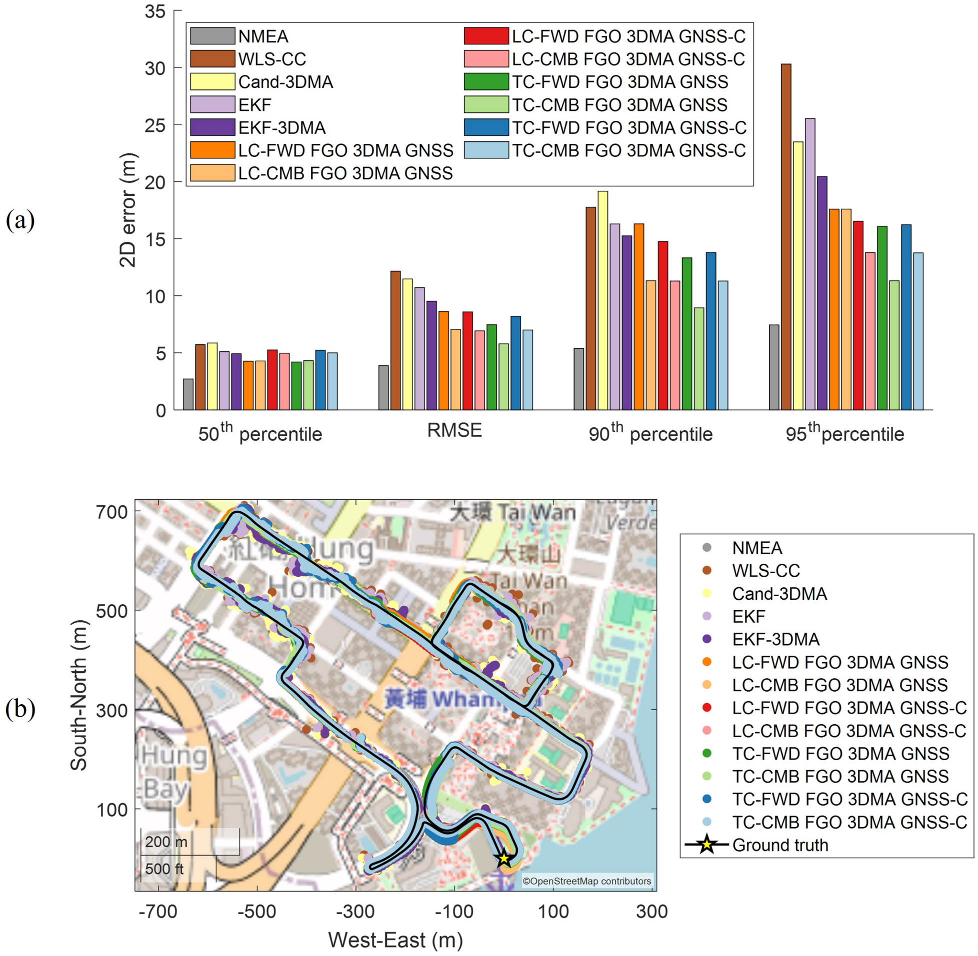

Figure 6.5: (a) Root mean square error (RMSE), 50th, 90th, and 95th percentile of the horizontal radial positioning error for the vehicular experiment across different algorithms. (b) Map plot on the positioning trajectories.

that FGO uses all historical measurements as prior information, thereby enhancing the robustness of the estimation.

Comparing the positioning performance between methods with and without clustering, enhancements are observed in LC FGOs, particularly notable is the nearly 4 m improvement at the 95th percentile error level. However, no positive impact is seen on TC FGOs with clustering; instead, the positioning error increases. This is mainly because clustering misidentifies satellite visibility classification for pseudorange correction using LBR. Therefore, accurate determination of satellite visibility is crucial for pseudorange correction in hybrid coupling, a consideration that applies to tightly coupling as well.

Moreover, comparing the two operational modes of FGO, optimizing in both forward and backward directions tends to yield better positioning performance than only optimizing in the forward direction. The RMSE of FGO in combined directions outperforms that of the forward-optimized approaches. Notably, there is at least a 1.2 m improvement in RMSE observed in FGO-CMB compared to FGO-FWD, highlighting that optimizing in both directions maximizes connections between measurements and states.

6.4 Summary

This study employs FGO to fuse a 3DMA GNSS with clustering and Doppler measurements or velocity estimates derived from them. The clustering procedure aims to segregate individual peaks within a multimodal position likelihood distribution rather than relying on the averaged position. By selecting the most suitable cluster based on the propagated location derived from the position solution and estimated velocity from the previous epoch, a more precise receiver location and position uncertainty can be attained. Consequently, the issue of solution shifting can be alleviated by integrating solutions from multiple epochs. FGO is utilized in this study to integrate the positions of the selected cluster in two modes: a loosely-coupled approach with the estimated velocity, and a hybrid-coupled approach incorporating pseudorange and Doppler measurements.

Segmenting candidate positions into clusters based on their likelihood scores enhances positioning accuracy, especially when the position distribution from the 3DMA GNSS is multimodal. Hybrid integration of GNSS measurements yields more precise positioning compared to a loosely coupled approach. However, the findings show the significance of visibility estimation for TC FGO 3DMA GNSS with clustering. Further investigation is warranted to determine appropriate confidence intervals.

This study employs the predicted position derived from the previous positioning estimate along with the estimated velocity or relative position to identify the most suitable cluster. Accurate cluster selection is important for ensuring the proposed method furnishes the correct information to the optimization processes. Therefore, additional research on cluster selection is imperative.

Chapter 7

Kriging-based 3DMA GNSS using FGO

In addition to loosely integrating the solution from 3DMA GNSS in the position domain, tightly integrating the scoring surface into the optimization process is believed to enhance the identification of multimodality. Consequently, this section introduces a method to mathematically model the scoring surface from candidate-based 3DMA GNSS, aiming to create a differentiable scoring surface. This surface can offer more detailed information on the locations and their scores for FGO.

7.1 An Overview of the Proposed System

Figure 7.1 provides an overview of the proposed Kriging-based 3DMA GNSS employing FGO. The system incorporates a pre-generated skymask database that encompasses the 3D building models relevant to the study area, and The application of 3DMA GNSS is limited to this specific coverage area [12]. The 3D building models utilized in this study were sourced from The Hong Kong Lands Department [57], featuring a level of detail (LoD) 1, and from the Department of Information Technology & Telecommunications' (DoITT) 2014 aerial survey (Department of City Planning) [59], featuring an LoD 2 for the testing scenarios in Hong Kong and New York City, respectively. After acquiring the new incoming pseudorange and Doppler measurements, the initial position can be estimated, and position hypothesis candidates are distributed. After that, the system is modelled, with all candidates sampled, and the integrated score for 3DMA GNSS is obtained. The solution integrates both shadow matching and likelihood-based ranging 3DMA GNSS approaches. Procedures of the system modelling and candidate sampling follow chapter 4 presented. The likelihood scores of candidates, once determined, can be converted and standardized into sampled costs, which denote the residuals. Then, an ordinary Kriging system is set up using the positions of the candidates and their corresponding residuals. This modelled Kriging system, along with Doppler measurements, is fed into the FGO for batch optimization to establish the FGO using Kriging-based 3DMA GNSS. Specifically for Kriging-based 3DMA GNSS, only a single-epoch modelled Kriging system needs to be provided as input for FGO.

The graph problem related to FGO using Kriging-based 3DMA GNSS comprises two primary elements: the 3DMA GNSS modeled by a Kriging system and factors associated with Doppler measurements. These factors encompass Doppler frequency measurements, motion propagation, and motion constraint.

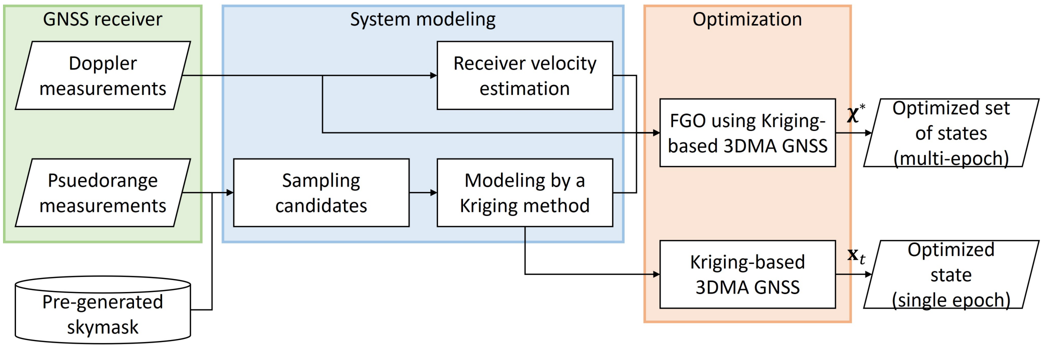

Figure 7.1: System architecture of the proposed multi-epoch Kriging-based 3DMA GNSS using FGO.

7.2 Expressing Likelihood Scoring as Cost

Objective of the candidate-based 3DMA GNSS can be expressed mathematically as a cost function,

$$\mathbf{x}_k^* = \arg\min_{\mathbf{x}} \|\tilde{\boldsymbol{\rho}}_k - \hat{\boldsymbol{\rho}}(\mathbf{x}_k)\| \tag{7.1}$$

where $\mathbf{x}$ is the state, corresponding to the receiver position in ECEF coordinate frame. $\mathbf{x}_k^*$ is the optimized state. $\tilde{\boldsymbol{\rho}}_k$ is a vector of the actual received observations. $\hat{\boldsymbol{\rho}}(\mathbf{x}_k)$ is the sophisticated model predicted measurement with the given state $\mathbf{x}_k$. Hence, the cost function can be formulated as an optimization problem, it can be optimized iteratively if it is differentiable. Therefore, the cost function is formally modelled by the Kriging method.

7.3 Modelling 3DMA GNSS using Ordinary Kriging

Kriging methods are commonly employed in spatial statistics, particularly when dealing with a limited number of sample points [103]. This section uses a Kriging method to mathematically represent the cost function of the optimization problem outlined in Equation 7.1, as shown in Figure 7.2. Initially, the 3DMA GNSS computes the likelihood score for each candidate and transforms it into a sampled cost. Once the samples are obtained, the locations of the candidates are used to interpolate and model the cost function, $\delta(x)$, using an ordinary Kriging method [104]. As the Kriging method estimates the parameters of an assumed function based on the sampled cost data, the function becomes differentiable. This implies that the Jacobian matrix of the cost function can be derived to facilitate iterative NLS optimization. In theory, the kriging method provides the same performance if sampled candidates cover the actual location of the receiver, which can also serve for high dynamic applications, such as vehicular applications.

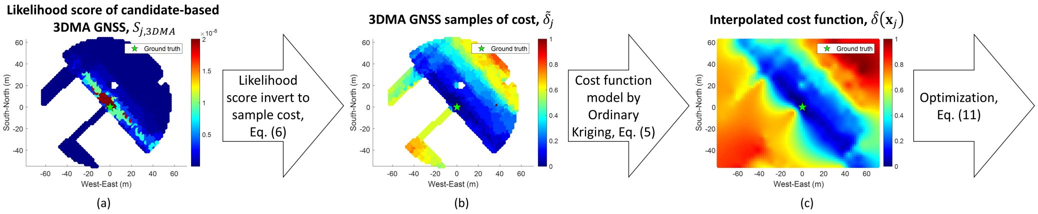

Figure 7.2: Process flow for calculating the cost function in the proposed Kriging-based 3DMA GNSS. (a) Likelihood score of the candidate-based 3DMA GNSS; (b) Sampled cost of the candidates calculated from the likelihood score (Equation 7.3); and (c) Interpolated cost function based on the ordinary Kriging method. Eq.: equation.

Although various types of Kriging methods exist, ordinary Kriging is chosen because it does not require the mean and covariance function of the sampled data to construct the prediction function, simplifying the formation of the cost function. Additionally, the candidate-based 3DMA GNSS with the Kriging method is modeled to compute the Jacobian matrix for NLS and FGO, aiming to predict the unknown values at an unsampled location from the observed data. This approach allows for a relaxation of the separation of the candidate during sampling.

The ordinary Kriging method at the position of interest can be expressed as,

$$\hat{\delta} = \boldsymbol{\omega}(\mathbf{r})^{\mathrm{T}}\tilde{\boldsymbol{\delta}} = [\hat{\boldsymbol{\Gamma}}^{-1}\hat{\gamma}(\mathbf{r})]^{\mathrm{T}}\tilde{\boldsymbol{\delta}} \tag{7.2}$$

where $\hat{\delta}$ is the predicted cost at the given position $\mathbf{r}$. $\boldsymbol{\omega}$ is the ordinary Kriging weighting vector with the Lagrange multiplier, λ. $\tilde{\boldsymbol{\delta}} = [\tilde{\delta}_1, \tilde{\delta}_2, \cdots, \tilde{\delta}_j, 1]^{\mathrm{T}}$ is the normalized sampled cost for candidates $1, 2, \cdots, j$. The proposed Kriging-based 3DMA GNSS aims to minimize the cost function (or residual) that is modelled by ordinary Kriging. Therefore, the likelihood scores are inverted to a cost (which is also known as a residual between the measurement and modelled estimation) for the candidate by,

$$\tilde{\delta}_j = -\log \Lambda_{j,\mathrm{3DMA}} \tag{7.3}$$

As a result, the cost vector $\tilde{\boldsymbol{\delta}}$ is normalized and used as the sample for Kriging interpolation.

The ordinary Kriging weighting vector $\boldsymbol{\omega}$ considers the distance between the desired location and all sampled candidates, also known as the spatial covariance of the sampled candidates. The calculation of $\boldsymbol{\omega}$ can be expressed in the matrix form as,

$$\hat{\mathbf{\Gamma}}^{-1}\hat{\gamma}(\mathbf{r}) = \begin{bmatrix} \gamma(\|\mathbf{r}_1-\mathbf{r}_1\|) & \gamma(\|\mathbf{r}_1-\mathbf{r}_2\|) & \cdots & \gamma(\|\mathbf{r}_1-\mathbf{r}_j\|) & 1 \\ \gamma(\|\mathbf{r}_2-\mathbf{r}_1\|) & \gamma(\|\mathbf{r}_2-\mathbf{r}_2\|) & \cdots & \gamma(\|\mathbf{r}_2-\mathbf{r}_j\|) & 1 \\ \vdots & \vdots & \ddots & \vdots & \vdots \\ \gamma(\|\mathbf{r}_j-\mathbf{r}_1\|) & \gamma(\|\mathbf{r}_j-\mathbf{r}_2\|) & \cdots & \gamma(\|\mathbf{r}_j-\mathbf{r}_j\|) & 1 \\ 1 & 1 & \cdots & 1 & 0 \end{bmatrix} \begin{bmatrix} \omega_1 \\ \omega_2 \\ \vdots \\ \omega_j \\ \lambda \end{bmatrix} = \begin{bmatrix} \gamma(\|\mathbf{r}_1-\mathbf{r}\|) \\ \gamma(\|\mathbf{r}_2-\mathbf{r}\|) \\ \vdots \\ \gamma(\|\mathbf{r}_j-\mathbf{r}\|) \\ \lambda \end{bmatrix} \tag{7.4}$$

where $\|\cdot\|$ is the Euclidean norm distance between two positions. $\gamma(h)$ is the semivariogram model, where the exponential model is selected in this study,

$$\gamma(h) = b[1-\exp{(-\frac{h}{a})}] \tag{7.5}$$

where $h = \|\cdot\|$ is the Euclidean norm distance between two positions, and a and b are constants. These constants are determined by the semivariogram analysis [104], [105], representing parameters on range and sill, respectively.

The semivariogram analysis estimates the average dissimilarity $\gamma^*(h^*)$ of all sampled candidates,

$$\gamma^*(h^*) = \frac{1}{2|N(h^*)|}\sum_{N(h^*)}(\tilde{\delta}_m - \tilde{\delta}_n)^2 \tag{7.6}$$

where $N(h^*) = \{(m,n) : \|\mathbf{r}_m - \mathbf{r}_n\| \in h^* \, \text{for} \, m,n = 1,2,...,j\}$ denotes sets of all pairs of candidates within the set of lag distance, h^*. For example, $h^* = \{5, 10, ..., h_k^*\}$ (in meters), the union $\cup_{k=1}^{K} h^*$ covers all linking distance, h_k^*, up to the maximum distance: $\max_{m,n=1,\cdots,j}\|\mathbf{r}_m - \mathbf{r}_n\|$ in the sampled candidates. The selection of the lag distance depends on the separations of candidates, which

```
Input:
Set of sampled candidates (position $\mathbf{r} = \{\mathbf{r}_1, \cdots, \mathbf{r}_j\}$, cost
$\tilde{\boldsymbol{\delta}} = \{\tilde{\delta}_1, \cdots, \tilde{\delta}_j\}$)
Subset of lagging distance $h^*$, e.g., $h^* = \{5, 10, \cdots, h_k^*\}$ (in metres)
Output:
Range value $a$
Sill value $b$

Initialize: $a \leftarrow 0$; $b \leftarrow 0$
for each element in $h^*$ do
    Initialize temporary variables: $\Lambda_h \leftarrow 0$; $N_h \leftarrow 0$
    for each element in sampled candidates, as $m = 1, \cdots, j$ do
        for each element in sampled candidates, as $n = 1, \cdots, j$ do
            $h \leftarrow \|\mathbf{r}_m - \mathbf{r}_n\|$
            if $h < h_k^*$ then
                $\Lambda_h \leftarrow \Lambda_h + (\tilde{\delta}_m - \tilde{\delta}_n)$
                $N_h \leftarrow N_h + 1$
            end
        end
    end
end
```

Algorithm 1: Pseudocode for the semivariogram calculation

affects the final number of candidates required to facilitate the Kriging interpolation. With a larger lag distance, the interpolation is supported by fewer candidates. Value of two parameters are determined, the sill value, b, is determined by $\gamma^*(\infty) = \lim_{|h| \to \infty} \gamma(h)$, while the range parameter, a, is the distance, h, at which the semivariogram first reaches the sill value. The pseudocode for determining the variogram constant is presented as algorithm 1.

After determining constants a and b for the model, weighting vector of ordinary Kriging, $\boldsymbol{\omega}$ in Equation 7.2, can be expressed as,

$$\boldsymbol{\omega}(\mathbf{r}) = \hat{\boldsymbol{\Gamma}}^{-1} \hat{\gamma}(\mathbf{r}) \tag{7.7}$$

As a result, the cost (residual) can be estimated with the Kriging method, as shown in Equation 7.2, at the given location of interest. The cost function of the 3DMA GNSS based on the Kriging method can be expressed as,

$$\mathbf{r}_k^* = \arg\min_{\mathbf{r}} \hat{\delta}(\mathbf{r}) = \arg\min_{\mathbf{r}} \left[\hat{\mathbf{\Gamma}}^{-1}\hat{\gamma}(\mathbf{r})\right]^{\mathrm{T}} \tilde{\boldsymbol{\delta}} \tag{7.8}$$

The block matrix $\hat{\mathbf{\Gamma}}$ and sampled residual $\tilde{\boldsymbol{\delta}}$ are obtained by the sampled candidates' positions associated with the candidate-based 3DMA GNSS, which are known terms in this function.

Therefore, the error factor of the Kriging-based 3DMA GNSS at epoch k can be formulated,

$$||e_{k,3MDA}||^2_{\mathbf{\Sigma}^{-2}_{k,3DMA}} = ||\hat{\delta}(\mathbf{r}_{k,ECEF})||^2_{\mathbf{\Sigma}^{-2}_{k,3DMA}} = \left|\left|\left[\hat{\mathbf{\Gamma}}^{-1}\hat{\gamma}(\mathbf{r})\right]^{\mathrm{T}} \tilde{\boldsymbol{\delta}}\right|\right|^2_{\mathbf{\Sigma}^{-2}_{k,3DMA}} \tag{7.9}$$

where $||\cdot||^2_Q$ stands for $||\mathbf{y}||^2_{\mathbf{Q}} = \mathbf{y}^{\mathrm{T}}\mathbf{Q}\mathbf{y}$, and $\mathbf{y}$ is a single column array. $\mathbf{\Sigma}^{-2}_{k,3DMA}$ is a diagonal uncertainty matrix of the Kriging-based 3DMA GNSS at the x-, y-, and z-axis, respectively. The variance at each axis is determined by the weighted distance variation between the Kriging-based 3DMA GNSS solution and all sampled candidates. The weighting is determined by the renormalized sampled cost of each corresponding candidate. And it is expressed as,

$$\mathbf{\Sigma}^{-2}_{k,3DMA} = c_1 \times \mathrm{diag}\left[\frac{\sum_j (1-\tilde{\delta}_j)(\mathbf{r}_j - \mathbf{r}_{k,ECEF})}{\sum_j (1-\tilde{\delta}_j)}\right] \tag{7.10}$$

where c_1 is an empirically determined tuning factor for the 3DMA GNSS error factor.

The error function modelled as the Kriging-based 3DMA GNSS can be solved using the LM algorithm implemented in Google Ceres Solver [99]. It's important to note that while the performance of Kriging-based 3DMA GNSS can match that of the candidate-based approach, it only mathematically models the sampled candidates. Consequently, if multimodal or drifting behaviour occurs, as illustrated in scenarios like those depicted in Figure 3.4, similar deviations should be observed in the estimated position. Additionally, the error factor can be utilized in batch optimization, as discussed in the case of FGO using Kriging-based 3DMA GNSS.

7.4 Doppler measurements

Doppler frequencies and velocity serve to connect consecutive GNSS position solution epochs. This study tightly integrates the received Doppler frequencies with the Kriging-based 3DMA GNSS. Within this framework, FGO optimizes the error factor derived from each available Doppler measurement individually. Additionally, the estimated velocity introduces two error factors that bridge two epochs in the FGO process: motion propagation and motion constraint.

7.4.1 Doppler Measurement Modelling

The received Doppler frequency measurement, $\tilde{\dot{\rho}}_k^i$, is compared with the modelled one, $\hat{\dot{\rho}}_k^i$, for all received satellites. Each pair of Doppler frequency differences forms an error factor for FGO to estimate the receiver's velocity at epoch k, $\mathbf{v}_{k,ECEF}$. The modelled Doppler frequency for i-th satellite can be expressed as,

$$\lambda^i \hat{\dot{\rho}}_k^i = \mathbf{v}_{k,ECEF} \cdot \mathbf{a}_k^i - \mathbf{v}_k^i \cdot \mathbf{a}_k^i + c \times (\dot{\delta t}_k^i - \dot{\delta t}_{k,u}) \tag{7.11}$$

where λ^i is the wavelength of the corresponding Doppler frequency. $\mathbf{v}_k^i$ and $\dot{\delta t}_k^i$ are the satellite's clock drift and the velocity of the satellite provided by ephemeris, respectively. $\mathbf{a}_k^i$ is the direct LOS unit vector from the satellite to the receiver. c is the constant of the speed of light. $\dot{\delta t}_{t,u}$ is the clock drift of the receiver to the corresponding constellation.

Therefore, the error factor on Doppler frequency for the i-th satellite at epoch k can be expressed as,

$$\|e_{k,i,\dot{\rho}}\|^2_{\sigma^{-2}_{k,i,\dot{\rho}}} = \|\lambda^i \tilde{\dot{\rho}}_k^i - \lambda^i \hat{\dot{\rho}}_k^i\|^2_{\sigma^{-2}_{k,i,\dot{\rho}}} \tag{7.12}$$

where $\sigma^{-2}_{k,i,\dot{\rho}} = c_2 \tau^i_{k,1}$ is the variance of the Doppler frequency measurement of i-th satellite at epoch k. $\tau^i_{k,1}$ is the uncertainty of the L1-band measurement the same as Equation (7) in [79].

Besides velocity, Doppler measurements also estimate the clock drift of the receiver to the corresponding constellation. The stability of clock drift over a given time span is crucial. Thus, ensuring a stable clock drift factor can help minimize the clock drift observed in the available satellite constellations, $\dot{\delta t}_{t,u}$, between successive epochs, expressed as,

$$\|e_{k,\dot{\delta t}}\|^2_{\mathbf{\Sigma}^{-2}_{k,\dot{\delta t}}} = \|c \times (\dot{\delta t}_{k+1,u} - \dot{\delta t}_{k,u})\|^2_{\mathbf{\Sigma}^{-2}_{k,\dot{\delta t}}} \tag{7.13}$$

where $\mathbf{\Sigma}^2_{k,\dot{\delta t}} = c_3 \times \text{diag}([\sigma^2_{k,GPS}, \sigma^2_{k,GLONASS}, \sigma^2_{k,Galileo}, \sigma^2_{k,BeiDou}])$ is a diagonal matrix of the variance of the clock drift of available constellations. The clock drift variance is assumed to be 1 m in this study, says $\sigma^2_{k,GPS} = \sigma^2_{k,GLONASS} = \sigma^2_{k,Galileo} = \sigma^2_{k,BeiDou} = 1.0$.

7.4.2 Motion Propagation

Motion propagation establishes a temporal link by utilizing the receiver's estimated positions and velocity. It uses the estimated positions from two consecutive epochs, $\mathbf{r}_k$ and $\mathbf{r}_{k+1}$, to compute the error between the estimated velocities, $\mathbf{v}_t$.The error factor can be obtained by,

$$\|e_{k,\mathbf{v}}\|^2_{\Sigma^{-2}_{k,\mathbf{v}}} = \|\Delta t \times \mathbf{v}_{k,ECEF} - (\mathbf{r}_{k+1} - \mathbf{r}_k)\|^2_{\Sigma^{-2}_{k,\mathbf{v}}} \tag{7.14}$$

where Δt is the time difference between epochs k and $k+1$. $\sigma^2_{t,\mathbf{v}} = c_4 \cdot diag([\sigma^2_{\mathbf{v},x}, \sigma^2_{\mathbf{v},y}, \sigma^2_{\mathbf{v},z}])$ is a diagonal covariance matrix associated with the velocity $\mathbf{v}_{k,ECEF}$ at the x-, y-, and z-axis, respectively. c_3 is an empirically determined tuning factor for the motion propagation factor.

7.4.3 Constant Velocity Motion Constraint

Motion constraint assumes a consistent velocity between two epochs [98], implying that users maintain a constant velocity with negligible acceleration. Consequently, the impact of the outlier of estimated velocity can be mitigated, and the optimized trajectory tends to exhibit smoother behaviour. It is worth noting that this thesis only uses the GNSS measurements, specifically Doppler measurement, to estimate the velocity for a practical implementation with an IMU. This factor should be replaced by considering the velocity change between consecutive epochs better. This factor minimizes the error between the positional change over two epochs and the averaged estimated velocity. The error factor can be expressed by,

$$\|e_{t,\bar{v}}\|^2_{\mathbf{\Sigma}^{-2}_{t,\bar{v}}} = \|\frac{\Delta t}{2}(\mathbf{v}_{t,ecef} + \mathbf{v}_{k+1,ECEF}) - (\mathbf{r}_{k+1,ECEF} - \mathbf{r}_{k,ECEF})\|^2_{\mathbf{\Sigma}^{-2}_{t,\bar{v}}} \quad (7.15)$$

where $\mathbf{\Sigma}^{-2}_{t,\bar{v}} = c_5 \times \frac{1}{2}(\mathbf{\Sigma}^2_{k,\mathbf{v}} + \mathbf{\Sigma}^2_{k+1,\mathbf{v}})$ is the averaged diagonal covariance matrix at epochs k and $k+1$. c_4 is an empirically determined tuning factor for the motion constraint factor.

7.5 FGO USING KRIGING-BASED 3DMA GNSS

FGO is applied to integrate the error factors associated with the proposed Kriging-based 3DMA GNSS and Doppler measurements. Instead of employing other filtering techniques like KF or EKF, FGO is chosen for its robust estimation capabilities, as demonstrated in prior research [17]. FGO conducts multiple iterations throughout the estimation process, leading to more accurate results. Moreover, FGO can effectively capture the time correlation between measurements and states, even when the measurements deviate from the Gaussian noise assumption, by using a batch of historical data. Hence, in this study, FGO is utilized as a batch optimization framework to optimize the state set, referred to as Tightly-coupled FGO using Kriging-based 3DMA GNSS (FGO-Krg-Doppler) in the evaluation phase. The proposed graph structure is shown in Figure 7.3.

The receiver's states set estimate, χ, for FGO is expressed as,

$$\chi = [\mathbf{x}_1, \mathbf{x}_2, \cdots, \mathbf{x}_k] \quad (7.16)$$

where state $\mathbf{x}_k = [\mathbf{r}_k, \boldsymbol{\delta t}_{k,u}, \mathbf{v}_k, \dot{\boldsymbol{\delta t}}_{k,u}]^{\mathrm{T}}$ represents the receiver's position $\mathbf{r}_k$ and

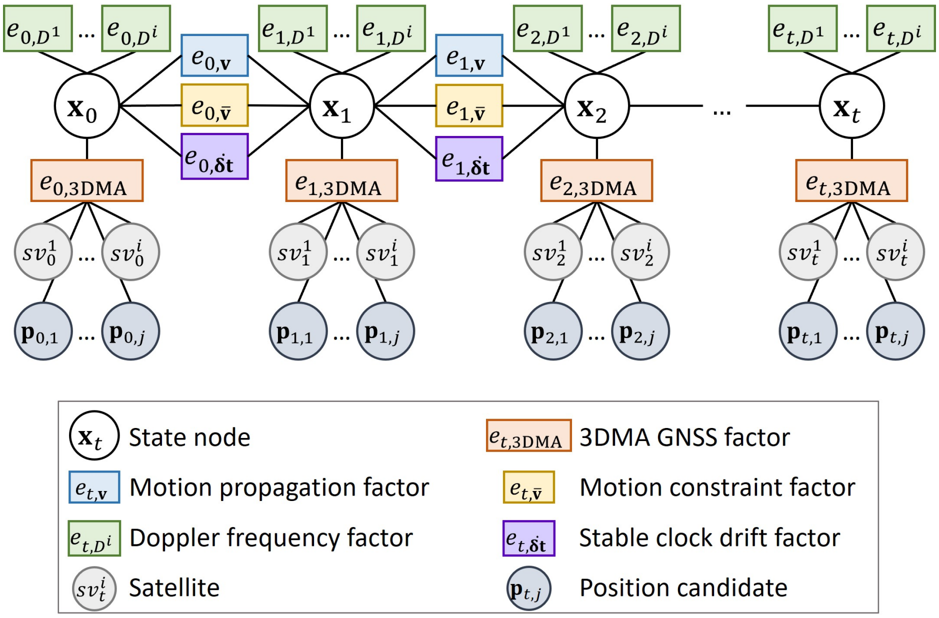

Figure 7.3: Structure of the factor graph of the proposed framework.

velocity $\mathbf{v}_k$ under ECEF coordinates at epoch k. $\boldsymbol{\delta t}_{k,u}$ and $\dot{\boldsymbol{\delta t}}_{k,u}$ are vectors on the clock offset and clock drift of the available satellite constellations, respectively. The Kriging-based 3DMA GNSS provides the initial position value; while velocities and clock drift are initialized using a least-squares (LS) approach based on Doppler measurements [106].

Hence, the formulation of the cost function for the position estimation of the Kriging-based 3DMA GNSS using FGO is as,

$$\chi^* = \arg\min_{\chi} \sum_k \left\{ \|e_{k,3MDA}\|^2_{\boldsymbol{\Sigma}^{-2}_{k,3DMA}} + \sum_i \|e_{k,i,\dot{\rho}}\|^2_{\sigma^{-2}_{k,i,\dot{\rho}}} + \|e_{k,\dot{\delta t}}\|^2_{\boldsymbol{\Sigma}^{-2}_{k,\dot{\delta t}}} + \|e_{k,\mathbf{v}}\|^2_{\Sigma^{-2}_{k,\mathbf{v}}} + \|e_{t,\bar{\boldsymbol{v}}}\|^2_{\boldsymbol{\Sigma}^{-2}_{t,\bar{\boldsymbol{v}}}} \right\} \tag{7.17}$$

where χ^* denotes the optimal estimation of the state set. The empirically determined tuning factors in uncertainty values for each factor, in Equation 7.9 and 7.11 to 7.15, are set as, $c_1 = 0.00053$, $c_2 = 0.0008$, $c_3 = 1.0$, $c_4 = 5.0$, and $c_5 = 0.3$, respectively. FGO is implemented using the LM algorithm through Google Ceres Solver [99].

7.6 Experiment Results and Analysis

7.6.1 Experiment Setup

This section presents three designed experiments: one pedestrian case in New York City (NYC), a vehicular case, and another pedestrian case in Hong Kong (HK). The recorded data comprises constellations and signal types including GPS L1, GLONASS G1, Galileo E1, and BeiDou B1. Details of the experiments are outlined in Table 7.1, and trajectories are shown in Figure 7.4. The average skymask elevation angle, $S\bar{M}$, is determined by averaging the elevation angles of the skymask at ground truth throughout the entire experiment period. It is expressed as,

$$S\bar{M} = \frac{1}{K}\sum_{k}\left(\frac{1}{360}\sum_{\psi} SM_k^{\psi}\right) \tag{7.18}$$

where SM_k^{ψ} is the skymask elevation angle at the corresponding azimuth angle, ψ, of the ground truth at epoch k. And K is the number of epochs in the experiment. As a result, a larger value of $S\bar{M}$ represents a more complex environment of the experiment.

RTKLIB [94], an open-source code, is employed for GNSS data processing, while Google Ceres Solver [99] is used for both the NLS and FGO processes. The optimization framework processes under the ECEF coordinate system. For vehicular cases, the ground truth is sourced from NovAtel SPAN-CPT [93], ensuring centimeter-level accuracy [92]. In pedestrian walking scenarios, the reference trajectory is obtained through post-processing interpolation. Pedestrian subjects carrying smartphones recorded the device's fused location output during data collection. These smartphone-generated locations are leveraged to calculate longitudinal speed and project vectors between starting and ending locations, serving as reference points.

Table 7.1: Environment of designed experiments. Exp: experiment

Exp	Scenario	Receiver	Place	Duration, T (second)	Average skymask elevation angle, $\bar{SM}$ (deg)
1	Pedestrian	Commercial	New York City	607	45.17
2	Vehicular	Commercial	Hong Kong	1538	47.00
3	Pedestrian	Smartphone	Hong Kong	152	45.79

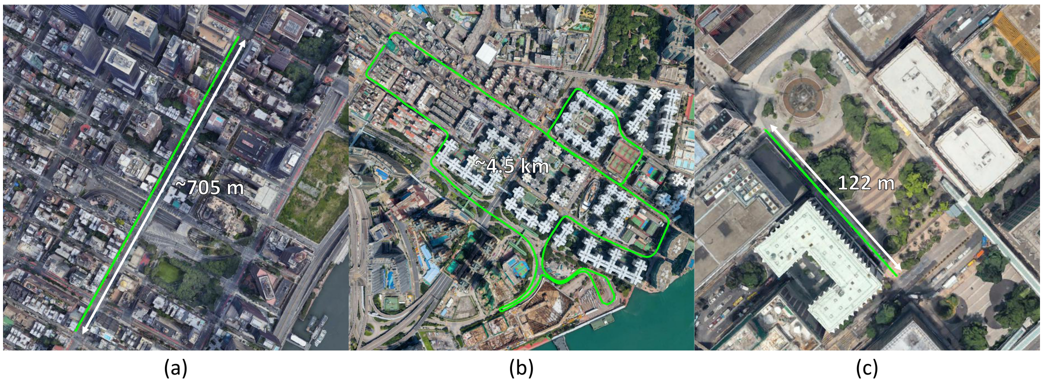

Figure 7.4: Aerial map and ground truth trajectory for Experiment (a) 1, (b) 2, and (c) 3.

7.6.2 Impact on Increasing the Candidate Sampling Separations

One limitation of the candidate-based 3DMA GNSS is the increased computational load associated with candidate sampling. To address this, one strategy involves widening the gap between candidates while maintaining the sampling radius, aiming to enhance the efficiency of the 3DMA GNSS. The kriging-based approach offers a solution by representing discrete candidates as a continuous function. This method allows for the interpolation of cost values at unsampled locations, even with increased gaps, as long as the separation increment does not disrupt the gradient within the sampling space. This section uses Experiment 2, the vehicular case in HK, to explore the relationship between candidate sampling separation, positioning accuracy, and computational load. The vehicular case in HK includes various levels of urbanization complexity, making it suitable for illustrating general scenarios. Figure 7.5 shows the relationship between candidate separations, the additional positioning error introduced by Kriging-based 3DMA GNSS, and the average computational time. It is important to note that the Kriging-based 3DMA GNSS is assumed to achieve identical performance to the candidate-based 3DMA GNSS in this evaluation. Thus, the evaluation utilizes the positioning solution of the candidate-based 3DMA GNSS as the initialization and the evaluation baseline, employing a distribution radius of 40 m with a 2 m separation.

The findings indicate that the separation distance is directly correlated with the positioning accuracy of the Kriging-based 3DMA GNSS. This relationship arises because the overall gradient of the sampled space becomes less distinct, making it challenging for the continuous function to accurately model and interpolate. Conversely, the computational time exhibits an inverse relationship with the separations, decreasing as the gap between candidates increases and thereby reducing the number of sampled candidates under the same distribution radius. Under identical sampled candidate sets (2 m separation), it is evident that the Kriging-based approach introduces approximately 0.1 m additional positioning error compared to

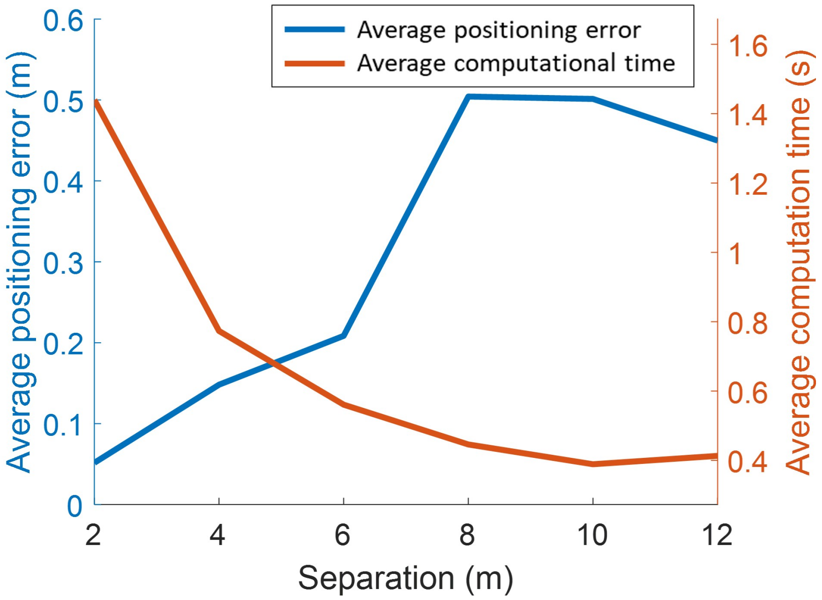

Figure 7.5: Average extra positioning error introduced by Kriging-based 3DMA GNSS and average computation time for one epoch solution. The comparison baseline for positioning error involves assessing the difference between candidate-based 3DMA GNSS and the proposed Kriging-based 3DMA GNSS.

the candidate-based method. This difference can be regarded as the nature of the solutions obtained, particularly in scenarios involving multimodal cases. While the candidate-based approach seeks to find a weighted average position, often falling locations near multiple local optima, the Kriging-based method tends to yield a solution located at one of these local minimum areas. Consequently, if the optimal area is distant from the actual locations, the positioning error of the Kriging-based approach may be smaller than that of the candidate-based method because the former relies on local minimum areas for determination.

As the separation increases, the positioning error demonstrates a consistent rise, whereas the computation time steadily decreases. Upon reaching a separation of 4 m, the Kriging-based 3DMA GNSS introduced an additional 0.2 m of positioning error overall, while the time required for computing a single epoch nearly halved. Saturation appears to occur at approximately 8 to 10 m separations, resulting in an approximate half-meter increase in positioning error and a demand for 0.4 s to compute the solution. Acquiring a balance between positioning accuracy and computational efficiency, a 4 m separation emerges as the optimal choice for the positioning performance evaluation setup. Consequently, the subsequent section uses a sampling configuration with a distribution radius of 40 m and a 4 m separation for the Kriging-based 3DMA GNSS.

7.6.3 Evaluation of the Positioning Performance

This section presents the post-processed results and conducts evaluations to assess the performance of the proposed algorithm, as determined in the preceding section. The evaluation aims to compare the proposed algorithms with several conventional solutions:

1. Device solution, NMEA: position solution outputted by the receiver using the algorithm developed by the manufacturer, for example, the NMEA solution.

2. Weighted least-squares, WLS: conventional weighted least-squares method [94], which uses pseudorange to estimate the receiver location.

3. Candidate-based 3DMA GNSS, Cand-3DMA: single point 3DMA GNSS solution based on the candidate-based approach [79], solution integrated shadow matching and likelihood-based ranging 3DMA GNSS. We evenly spaced sample the candidates in a 40 m radius with a 2 m separation.

4. Kriging-based 3DMA GNSS, KRG-3DMA: single point 3DMA GNSS solution obtained by minimizing the ordinary Kriging-modelled function via the LM method. We evenly spaced sample the candidates in a 40 m radius with a 4 m separation.

5. EKF using candidate-based 3DMA GNSS, EKF-cand-vel: solution based on the integration of Solution 3, Cand-3DMA, and estimated velocity from Doppler measurements through a conventional EKF estimator [16] with adaptive noise.

6. Loosely-coupled FGO using candidate-based 3DMA GNSS, FGO-cand-vel: integrated solution of Solution 3, Cand-3DMA, and estimated velocity from Doppler measurements through FGO [107].

7. Semi-tightly-coupled FGO using Kriging-based 3DMA GNSS, FGO-Krg-vel: integrated solution of Solution 4, KRG-3DMA, and estimated velocity from Doppler measurements through FGO [108].

8. Tightly-coupled FGO using Kriging-based 3DMA GNSS, FGO-Krg-Doppler: proposed solution in Section 5, integrated solution of Solution 4, KRG-3DMA, and Doppler frequency measurements through FGO [109].

The post-processed results of the algorithms are summarized in Table 7.2. Comparing the single-epoch positioning, it is evident that 3DMA GNSS outperforms the conventional WLS. Additionally, as discussed in subsection 7.6.2, Kriging-based 3DMA GNSS is assumed to offer identical performance to candidate-based 3DMA GNSS, a notion confirmed by the actual results. Notably, the integration of multi-epoch positions leads to enhanced positioning accuracy and robustness.

FGO consistently outperforms EKF across all experiments. Furthermore, when integrating with FGO, notable improvement is observed after replacing the 3DMA GNSS error factor with the Kriging-modeled function compared to using loosely coupled positions. Moreover, integrating Doppler frequency measurements further enhances position accuracy compared to using Doppler estimated velocity alone.

Table 7.2: Positioning result statistics. STD: standard deviation; RMSE: root-mean-square-error (Unit: m)

Experiment	Solution	Mean	STD	RMSE
1. Pedestrian	NMEA	13.16	11.08	17.20
	WLS	73.77	54.99	91.98
	Cand-3DMA	16.19	10.62	19.36
	Krg-3DMA	16.37	10.70	19.55
	EKF-cand-vel	13.77	8.83	16.35
	FGO-cand-vel	12.50	7.40	14.52
	FGO-Krg-vel	10.00	6.75	12.06
	FGO-Krg-Doppler	8.79	5.89	10.58
2. Vehicular	NMEA	3.04	2.36	3.84
	WLS	11.75	9.20	14.92
	Cand-3DMA	6.46	4.80	8.04
	Krg-3DMA	6.51	4.84	8.11
	EKF-cand-vel	5.71	3.83	6.88
	FGO-cand-vel	4.78	2.90	5.59
	FGO-Krg-vel	4.42	2.61	5.13
	FGO-Krg-Doppler	4.23	2.66	4.99
3. Pedestrian	NMEA	5.90	2.09	6.26
	WLS	58.79	19.56	61.94
	Cand-3DMA	8.35	6.40	10.50
	Krg-3DMA	8.49	6.56	10.72
	EKF-cand-vel	6.55	3.87	7.61
	FGO-cand-vel	5.28	2.18	5.71
	FGO-Krg-vel	4.00	2.55	4.74
	FGO-Krg-Doppler	3.40	1.78	3.84

The first designed experiment is a pedestrian case conducted in the urban depths of New York City, with the positioning results and statistics depicted in Figure 7.6. Both Cand-3DMA and Krg-3DMA achieve an average positioning accuracy of within 20 meters. Notably, upon integrating the Doppler measurements, an improvement of at least 3 meters was observed. The integration of Kriging-based 3DMA GNSS and Doppler measurements notably reduces the average positioning error to 10 meters.

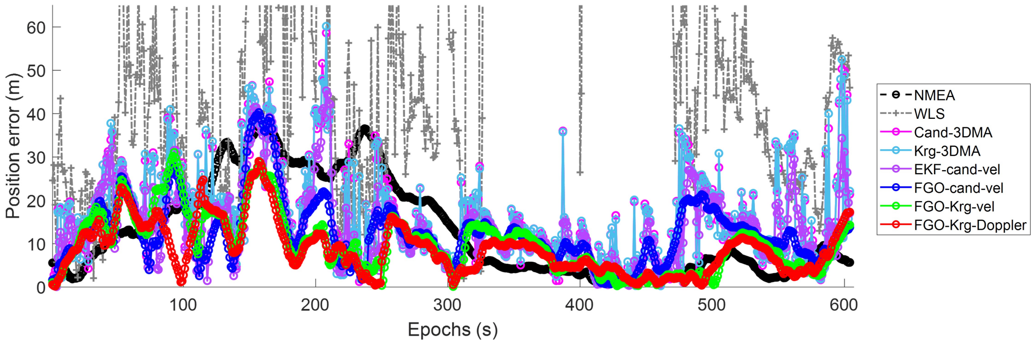

Figure 7.6: 2D positioning errors of Experiment 1.

When comparing candidate-based and Kriging-based 3DMA GNSS, both methods are expected to yield similar positioning performance. However, the latter expresses the sampled candidates mathematically and solves them using the LM method. The overall positioning results validate this assumption, with Kriging-based 3DMA GNSS introducing a positioning RMSE only 0.2 meters more than candidate-based 3DMA GNSS. Nonetheless, two common limitations of candidate-based 3DMA GNSS, namely multimodal and solution shifting, remain unresolved by Kriging-based 3DMA GNSS alone. For further analysis, two snapshot epochs are selected, as shown in Figure 7.7, where Kriging-based 3DMA GNSS demonstrates an error identical to that of candidate-based 3DMA GNSS.

Upon integrating information from Doppler measurements, some algorithms can address the multimodal issue depicted in Figure 7.7(a). Despite this, large po-

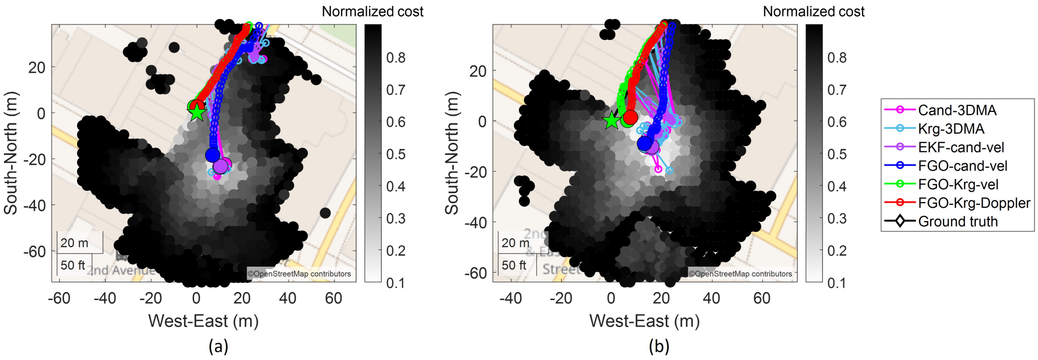

Figure 7.7: Selected cases on (a) multimodal and (b) solution shifting.

sition errors persist in EKF-cand-vel and FGO-cand-vel due to the predominance of errors arising from the single-epoch solution. Conversely, enhancements are shown in FGO-Krg-vel and FGO-Krg-Doppler owing to the higher-resolution information derived from both 3DMA GNSS and Doppler measurements fed into the optimization process. This underscores the advantage of integrating Krg-3DMA GNSS into the solution. While Cand-3DMA determines the solution through candidate averaging, Krg-3DMA follows an optimization approach, converging toward a location with minimal cost. Krg-3DMA is more subjected to multimodal issues, exhibiting a significant bias. Thus, the addition of velocity constraint significantly mitigates this issue, highlighting the advantages of the Krg-3DMA method in identifying the correct minimal cost area.

However, incorporating temporal domain information does not resolve the limitation observed in the solution shifting case shown in Figure 7.7(b). This is because the consistently erroneous information provided by the sampled candidates leads to concentrated candidates with small sampled costs, resulting in a small estimated variance based on Equation 7.10, which fails to accurately bound the actual positioning error. Consequently, the optimization process is compromised, as it mistakenly assumes the accuracy of the 3DMA GNSS, leading to deviations in the determined solution. Notably, for FGO-Krg-vel and FGO-Krg-Doppler, although they are both affected by solution shifting at the snapshot epoch shown, they benefit from providing higher resolution information to the optimization process. However, the solution shifting is slower than that observed in FGO-cand-vel, particularly in the earlier period.

Another important factor influencing the optimization performance is the estimated variance of 3DMA GNSS. The variance should effectively bound the actual positioning error to ensure optimal performance. However, particularly in solution shifting scenarios, the estimated variance tends to be small despite the presence of significant positioning errors. This difference arises from the concentration of candidates with low costs, consistently providing erroneous information. Figure 7.8 shows the actual positioning error and estimated standard deviation (STD) of single-epoch 3DMA GNSS and the FGO-integrated algorithms.

During certain periods characterized by solution shifting, the actual positioning error tends to be large, but the estimated variance is small, as illustrated within the yellow frame in Figure 7.8. In such instances, the optimization process of FGO-Krg-vel erroneously places trust in the 3DMA GNSS, thereby causing the results to be influenced by the errors inherent in the 3DMA GNSS. Conversely, the tight integration of Doppler measurements can offer assistance in some scenarios. By employing Doppler measurements directly, FGO-Krg-Doppler shows a stronger constraints on the temporal domain, leading to improved positioning performance, as shown within the yellow framed period in Figure 7.8.

Nevertheless, tightly integrating Doppler measurements sometimes fails to adequately constrain the position. For instance, considering the period highlighted

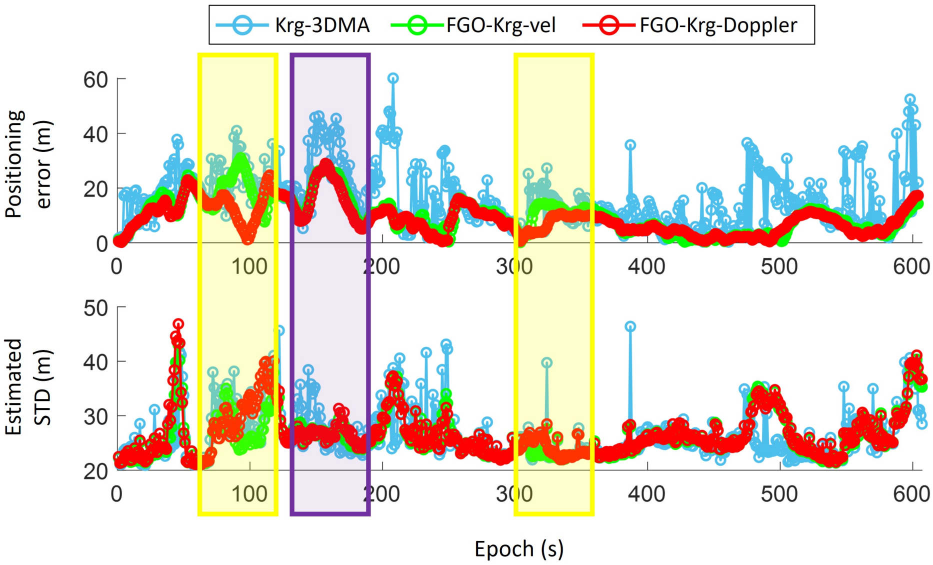

Figure 7.8: Positioning statistic of Experiment 1 on positioning error and Equation (13) estimated standard deviation (STD).

within the purple frame in Figure 7.8, the estimated standard deviation remains similar for both the Kriging-based 3DMA GNSS and the FGO-integrated solution. Although the two FGO results effectively mitigate the positioning error, they exhibit similar trends in positioning error. This reveals the significance of accurate uncertainty estimation in integration and optimization, particularly for identifying cases of solution shifting. Continuous efforts are warranted to detect outliers in 3DMA GNSS as part of ongoing work.

The second experiment involves a vehicular scenario traversing various urban environments in Hong Kong. The positioning results and statistical data are depicted in Figure 7.9. The experiment begins in a relatively open-sky setting, progresses through deep urban areas, and then returns to the starting open-sky location to complete a closed loop. With the aid of the 3D building model, the positioning error is significantly reduced, from an average of 11.75 m with WLS to approximately 6.5 m. For algorithms incorporating temporal continuity, both positioning accuracy and robustness witness an improvement of at least 1 m. In terms of loosely-coupled approaches, FGO outperforms EKF by approximately 1 m in accuracy and deviation. Although there is a slight enhancement of 0.6 m after tightly integrating Kriging-based 3DMA GNSS and Doppler measurements, the receiver's output solution still exhibits superior performance by approximately 1 m on average in this scenario.

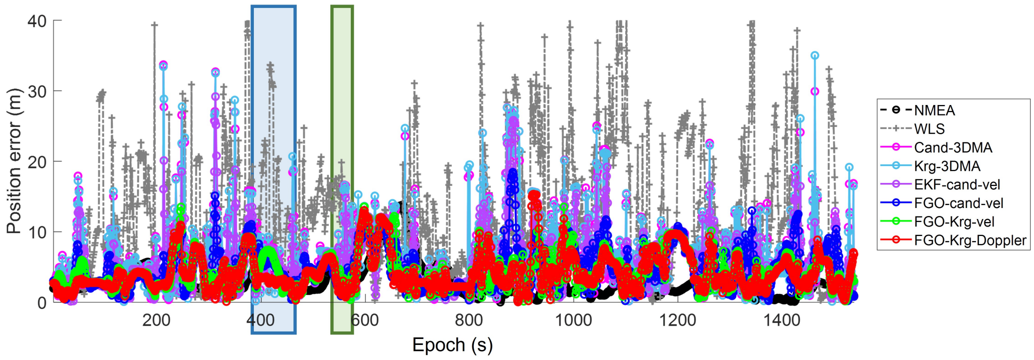

Figure 7.9: 2D positioning errors of Experiment 2.

Two specific scenarios are selected for a detailed comparison of each 3DMA GNSS, as well as the performance of both EKF and FGO. These scenarios include a stationary case during a traffic light wait (blue-framed period in Figure 7.9) and a moving case for a right turn (green-framed period in Figure 7.9), as illustrated in Figure 7.10 and Figure 7.11, respectively. First, the stationary case study at the traffic light is studied. The vehicle remains motionless during epochs 11 s to 64 s while awaiting the traffic light, implying that any changes in position or velocity are attributable to unmodeled noise. Between epochs around 20 to 40, both EKF-cand-vel, FGO-cand-vel, and FGO-Krg-vel are influenced by the positional error of the single-epoch 3DMA GNSS. In contrast, FGO-Krg-Doppler, which tightly couples the Doppler measurements in optimization, exhibits better de-weighting of erroneous or outlier measurements to provide stronger constraints in the zero-velocity scenario.

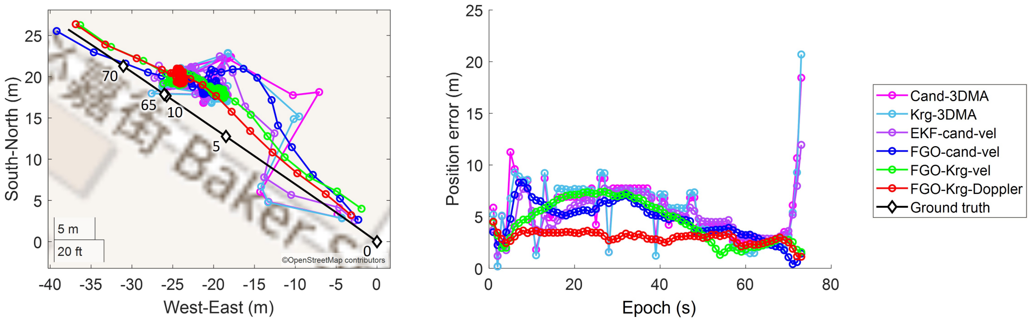

(a) (b)

Figure 7.10: Selected scenario on waiting at the traffic light (blue framed period in Figure 10) on (a) map plot and (b) positioning errors.

The second scenario involves a moving case during a right turn. EKF exhibits a significant error due to the drifting of the 3DMA GNSS result. Among the three FGO approaches, FGO-cand-vel initially demonstrates similar accuracy to FGO-Krg-Doppler before the turn, but its performance worsens after epoch 20. This indicates that only loosely coupling position and velocity cannot provide a strong enough constraint to achieve satisfactory accuracy. Upon replacing the position error factor with a Kriging-modelled one, although the position error can be mitigated when driving straight after the turn at epoch 25, a relatively large positioning error emerges when exiting the turn between epochs 20 and 25. In the integration of Kriging-based 3DMA GNSS and Doppler measurements, a smaller positioning error is observed overall, and the entire trajectory aligns more closely with the reference trajectory. However, some relatively large errors occur during the turn (epoch 18) and after the turn (epoch 28), primarily affecting the longitudinal aspect of the driving direction.

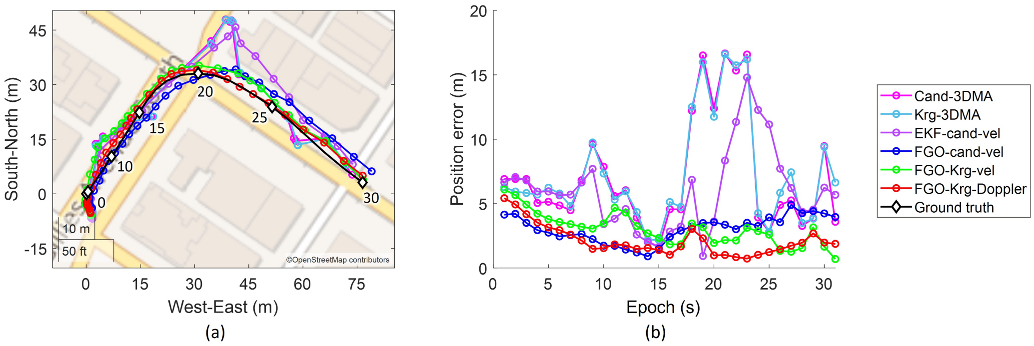

Figure 7.11: Case study on making a right turn (green framed period in Figure 10) on (a) map plot and (b) positioning errors.

The last planned experiment involves a pedestrian scenario in an urban setting in Hong Kong, as shown in Figure 7.12 The pedestrian trajectory follows a straight line parallel to the buildings. The average positioning error of the single-epoch 3DMA GNSS is approximately 8.5 meters. Upon integration with Doppler measurements, the positioning error is reduced to an average of 3.4 meters.

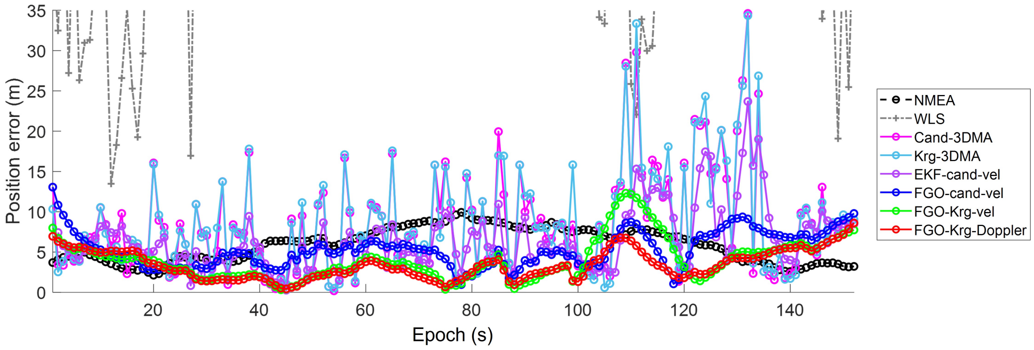

Figure 7.12: 2D horizontal positioning error for Experiment 3.

According to the positioning statistics, FGO-Krg-vel and FGO-Krg-Doppler demonstrate an excellent positioning accuracies, particularly between epochs 30 to 70 and after epoch 120. However, there was a significant positioning error around epoch 110 for FGO-Krg-vel. This poor performance is primarily caused by solution shifting in the lowest sampled cost area along the longitudinal side of the moving direction.

7.7 Summary

This study presents two primary contributions. Firstly, it introduces the modelling of candidate-based 3DMA GNSS using an ordinary Kriging method, enabling iterative estimation of the receiver location via the NLS approach. This method establishes a Kriging system, and the LM method is used to ascertain the receiver location, termed as the Kriging-based 3DMA GNSS. Secondly, it integrates the Kriging-based 3DMA GNSS with Doppler measurements through FGO, enabling the optimization of multi-epoch states via FGO to achieve a more resilient position solution.

Based on the post-processing results derived from real data collected in both Hong Kong and New York City, the performance of the Kriging-based 3DMA GNSS generally matches that of the candidate-based 3DMA GNSS across various scenarios. Furthermore, employing FGO with Kriging-based 3DMA GNSS allows for the optimization of states across multiple epochs, resulting in smoother trajectories. A comparative analysis is conducted among the proposed FGO using Kriging-based 3DMA GNSS, FGO, and EKF using candidate-based 3DMA GNSS with loose coupling. The tightly-coupled FGO with Kriging-based 3DMA GNSS demonstrates better positioning performance by enhanced accuracy and robustness, yielding an average positioning RMSE of approximately 6 meters across all three experimental setups. This study showcases that the proposed approach effectively mitigates the multimodal issue encountered in 3DMA GNSS, thereby improving positioning performance. Moreover, by using fewer position candidates, the proposed method reduces computational load, with an optimal separation setup of 4 meters. Future enhancements could focus on refining candidate sampling efficiency by considering the uncertainty of previous epoch solutions and velocities to determine the sampling area.

However, the findings indicate that solution shifting remains a limitation of 3DMA GNSS, where the adaptive variance estimation outlined in Equation 7.10 fails to detect drifting occurrences. The identification of these outlier epochs still requires further exploration. Additionally, addressing the multimodal limitation in the position domain could involve inputting samples as multi-hypotheses into FGO to better represent Gaussian mixture occurrences. Furthermore, while the proposed Kriging-based 3DMA GNSS builds upon the foundational aspects of candidate-based 3DMA GNSS, future investigations will focus on optimizing the sampling area to achieve optimal performance for the Kriging method. Moreover, mathematically expressing the 3DMA GNSS algorithm or even 3D building models as a differentiable function input to FGO can enhance the contribution of 3DMA GNSS.

Chapter 8

Conclusion

GNSS positioning remains an irreplaceable component in globally referenced positioning for applications such as ITS and LBS. However, accurate GNSS positioning in urban environments continues to present a significant challenge. NLOS receptions introduce a particularly severe threat to the reliability of GNSS positioning. Effectively identifying and mitigating these errors represents a crucial step towards achieving precise and reliable GNSS positioning solutions within urban canyons. The performance of GNSS positioning is greatly influenced by the surrounding environmental conditions; hence, understanding environmental perception can serve as a fundamental predictor of potential degradation in accuracy. In this context, 3D building models come up as invaluable resources that fulfil the necessary functions for enhancing GNSS positioning accuracy in urban settings. This study delves into the significance of 3D building models in enhancing urban positioning by proposing a novel 3DMA GNSS positioning framework. The development and analysis of the proposed algorithm span various stages, from its conceptualization to its practical application in real-world scenarios. This chapter aims to draw conclusions from the study's findings, organized according to five key stages of algorithm development: (1) Identifying the limitations of the basic candidate-based 3DMA GNSS approach in urban environments; (2) Integrating second-frequency GNSS measurements and refining measurement modeling; (3) Effectively selecting sampling candidates based on contextual information and loosely integrating position solutions from 3DMA GNSS with estimated velocity using FGO; (4) Employing clustering techniques on position candidates based on the scoring surface and hybrid integration with estimated velocity; and (5) Tightly integrating the scoring surface into the FGO estimation process. Furthermore, this chapter addresses remaining challenges and potential avenues for future research and development in the field.

8.1 Conclusions of this Research

8.1.1 Baisc Candidate-Based 3DMA GNSS Performance Evaluation

In chapter 3, a basic candidate-based 3DMA GNSS algorithm is introduced. It can mainly divided into three steps; it is first initialed by the WLS position and distributes position hypothesis candidates around. Then each candidates are sampled and scored based on the similarity of modelled and received measurements. After that, the position is determined by weighted averaging of the scoring surface. Based on the actual recorded vehicular data in Hong Kong, integrating shadow matching and ranging-based 3DMA GNSS can improve the overall positioning accuracy in urban canyons, and connecting multiple epoch solutions can improve the positioning accuracy. However, distributed candidates need to cover the actual location of the receiver to provide the best performance. Thus, the initial location and sampling radius are important factors under this circumstance. Besides, multimodal and solution shifting often occur and degrade the positioning performance.

8.1.2 Advanced Candidate-based 3DMA GNSS

Chapter 4 improves the candidate-based 3DMA GNSS by using dual-frequency measurements and improving receiver clock estimation in the pseudorange measurement modelling. Dual-frequency GNSS signals refer to L1- and L5-band signals, where new smartphones are often capable of receiving the L5-band signals. Due to the fundamental nature of the L5-band signal of a higher chipping rate, it can naively prevent multipath effects for the LOS signal. Meanwhile, it can also mitigate the NLOS multipath, which refers to multiple NLOS signals that arrive at the receiver, to isolate the NLOS reflection delays. As a result, 3DMA GNSS can better estimate and correct the ranging delays caused by the reflection. According to the experiments conducted in Hong Kong urban canyons, the proposed candidate-based 3DMA GNSS can provide a more stable positioning performance at an accuracy within 10 m on average. The L5-band measurements can reduce the pseudorange difference through a noticeable improvement in positioning accuracy. With the new smartphones starting to support the L5-band signal, urban positioning will be the future development.

8.1.3 Loosely-coupled (LC) 3DMA GNSS and Velocity

In chapter 5, a context-based candidate distribution approach is proposed, and the position solution from 3DMA GNSS is loosely integrated with Doppler frequency estimated velocity using FGO. Skymask context-based candidate distribution approach distributes candidates in an ellipsoid along the longitudinal direction of the street rather than a circle. Two benefits can be achieved by this method; the first advantage is mitigating the impact of multimodal in the lateral direction of the street. Another benefit is effectively reducing the number of sampling candidates, thus the computational load can be reduced. The estimated position from 3DMA GNSS is then integrated with velocity estimated by Doppler measurements, and a more robust and accurate positioning performance can be provided. Positioning performance is evaluated by the designed experiments conducted in Hong Kong and New York City, more accurate and robust performance can be achieved after integrating with velocity using FGO.

8.1.4 Hybrid-coupled (HC) 3DMA GNSS and Velocity

In chapter 6, the region growing method is applied to the candidates' scoring surface to identify high-score peaks into separate clusters. Therefore, multimodal can be detected, and the cluster is selected based on the position and velocity of the previous epoch. The selected cluster's position and its estimated variance are input to the FGO and integrated with pseudorange and Doppler measurements as a hybrid coupled (HC) approach. Meanwhile, the selected cluster provides the visibility prediction for the integration, pseudorange is corrected by LBR, and Doppler measurement is excluded for NLOS-predicted satellites in the FGO estimation.

Results of the vehicular shows that selecting correct cluster is important for HC FGO to determine the correct satellite visibility, which is believed that also apply to TC as well.

8.1.5 Tightly-coupled (LC) 3DMA GNSS and Doppler measurements

Chapter 7 models the candidate-based 3DMA GNSS using an ordinary Kriging method, allowing the receiver location to be iteratively estimated using the NLS approach. The Kriging system is established, and the LM method is used to determine the receiver location, named the Kriging-based 3DMA GNSS. The Kriging-based 3DMA GNSS is then integrated with Doppler measurements through FGO. In this manner, multi-epoch states could be optimized through FGO to obtain a more robust position solution.

According to the post-processing results of actual data recorded in Hong Kong and New York City, the performance of the Kriging-based 3DMA GNSS is comparable to that of the candidate-based 3DMA GNSS in most cases. Moreover, the FGO using Kriging-based 3DMA GNSS can optimize the states for multiple epochs, and a smoother trajectory can be obtained. A comparison of the proposed FGO using Kriging-based 3DMA GNSS, FGO and EKF using candidate-based 3DMA GNSS as loosely coupling is given. The FGO using Kriging-based 3DMA GNSS achieves superior positioning results with better positioning accuracy and robustness. Moreover, the proposed method uses fewer position candidates and thus corresponds to a decreased computational load.

8.2 Potential Future Developments

The proposed positioning framework successfully suppresses the positioning error, where 95-percent of positioning errors are within 10 m in some situations. However, applications related to the ITS, like autonomous driving, still require the error to be bounded by 3 m or even less. Therefore, plenty of space can be improved in terms of accuracy and robustness for different civil applications. This section summarizes some suggestions for the development as a beacon for future studies.

8.2.1 Incorporating More Sophisticated Model

Developing heuristic models based on quantitative features extracted from the surrounding building environment could potentially result in more adaptable and efficient performance. By quantifying features such as building height, density, and orientation and integrating them into the heuristic models, these algorithms could more effectively adjust to diverse urban environments, thereby offering more precise positioning solutions. Such an approach has the potential to bolster the robustness and reliability of 3DMA GNSS systems across various scenarios, thereby expanding their practical utility in real-world urban settings.

8.2.2 Vertical Positioning Enhancements

Extend 3DMA GNSS algorithms to improve vertical positioning for applications like UAV navigation. By incorporating vertical multipath information and refining elevation weighting strategies, the system can achieve better altitude accuracy.

8.2.3 Introducing Higher Resolution Measurements

To enhance the positioning performance in urban canyons, it is necessary to introduce carrier phase measurements in the algorithm. The introduction of carrier phase measurements can aid positioning, for instance, by integrating the time difference carrier phase (TDCP) measurements with the RTK GNSS. TDCP assumes that no cycle slip occurs between consecutive epochs, and thus, no ambiguity resolution is required. In other words, when TDCP measurements are used, no reference station is required for positioning, and position estimation is not relative to the reference station.

Furthermore, state-of-the-art approaches, such as the PPP-RTK, suffer from the difficulties of integer ambiguity fixing. There is a lack of study on undifferenced ambiguity resolution in urban positioning, which can be a study direction in the future.

8.3 Dynamic 3D Environmental Updates

Traditional 3DMA GNSS relies on static 3D building models, which may not reflect real-time changes in urban environments, such as new construction, demolition, or temporary structures. Incorporating real-time updates from aerial imagery, LiDAR, or crowdsourced data can dynamically enhance the accuracy and relevance of 3D maps.

8.4 Machine Learning for Error Estimation

Implement machine learning models to predict and correct GNSS measurement errors using 3D map features. Models can adaptively learn the relationship between environmental characteristics (e.g., building density, satellite visibility) and GNSS signal quality, improving error correction over time.

8.5 Integration with Multi-Sensor Fusion

Combine GNSS with IMUs, cameras, and LiDAR to mitigate signal degradation in dense urban areas. By fusing data from these sensors with 3D building models, the system can better handle scenarios where GNSS signals are weak or obstructed by tall buildings.

8.6 Crowdsourced and Scalable 3D Mapping

Using crowdsourced GNSS data from users to refine and update 3D building models continuously. Develop scalable methods to manage and process this data, ensuring the mapping system remains current and relevant for various urban landscapes.

8.7 Edge Computing for Real-Time Processing

Deploy edge computing infrastructure to process GNSS and 3D map data locally, reducing latency and improving real-time performance. This is particularly useful for time-critical applications like autonomous vehicles or UAV operations.

8.8 Resilience to GNSS Spoofing and Interference

Incorporate anomaly detection mechanisms using 3D map constraints to identify and mitigate spoofing or interference. By cross-validating positioning data with map-based predictions, the system can enhance security and reliability.

Chapter 9

References

[1] T. Türk, “Location based services (lbs) and related standards,” Sep. 2006.

[2] C. Hegarty and E. Chatre, “Evolution of the global navigation satellite system (gnss),” *Proceedings of the IEEE*, vol. 96, pp. 1902–1917, Jan. 2009. DOI: `10.1109/JPROC.2008.2006090`.

[3] E. D. Kaplan and C. J. Hegarty, *Understanding GPS Principles and Applications, Second Edition*. Boston, London: Artech, 2006.

[4] P. D. Groves, “Multipath vs. nlos signals,” *Inside GNSS*, vol. 8, pp. 40–42, 2013.

[5] P. D. Groves, “It’s time for 3d mapping–aided gnss,” *Inside GNSS Magazine*, pp. 50–56, 2016.

[6] F. v. Diggelen, “End game for urban gnss: Google’s use of 3d building models,” *Inside GNSS Magazine*, pp. 42–49, 2021.

[7] L. Wang, P. D. Groves, and M. K. Ziebart, “Gnss shadow matching: Improving urban positioning accuracy using a 3d city model with optimized

visibility scoring scheme," *NAVIGATION, Journal of the Institute of Navigation*, vol. 60, no. 3, pp. 195–207, 2013, ISSN: 0028-1522. DOI: `10.1002/navi.38`.

[8] L. Wang, P. D. Groves, and M. K. Ziebart, "Smartphone shadow matching for better cross-street gnss positioning in urban environments," *Journal of Navigation*, vol. 68, no. 3, pp. 411–433, 2015, ISSN: 0373-4633. DOI: `10.1017/S0373463314000836`. [Online]. Available: `https://www.cambridge.org/core/article/smartphone-shadow-matching-for-better-crossstreet-gnss-positioning-in-urban-environments/A146E3A7E0F01D777C31B4D93291ECF2`.

[9] L.-T. Hsu, Y. Gu, and S. Kamijo, "3d building model-based pedestrian positioning method using gps/glonass/qzss and its reliability calculation," *GPS Solutions*, vol. 20, no. 3, pp. 413–428, 2016, ISSN: 1080-5370. DOI: `10.1007/s10291-015-0451-7`.

[10] S. Miura, L.-T. Hsu, F. Chen, and S. Kamijo, "Gps error correction with pseudorange evaluation using three-dimensional maps," *IEEE Transactions on Intelligent Transportation Systems*, vol. 16, no. 6, pp. 3104–3115, 2015, ISSN: 1524-9050. DOI: `10.1109/Tits.2015.2432122`.

[11] P. D. Groves, Q. Zhong, R. Faragher, and P. Esteves, "Proceedings of the 33rd international technical meeting of the satellite division of the institute of navigation (ion gnss+ 2020)," pp. 2327–2346, ISBN: 2331-5911. DOI: `10.33012/2020.17767`.

[12] H.-F. Ng, G. Zhang, and L.-T. Hsu, "A computation effective range-based 3d mapping aided gnss with nlos correction method," *Journal of Naviga-*

tion, vol. 73, no. 6, pp. 1202–1222, 2020, ISSN: 0373-4633. DOI: `10.1017/S037346332000003x`.

[13] L.-T. Hsu, "Analysis and modeling gps nlos effect in highly urbanized area," *GPS Solutions*, vol. 22, no. 1, p. 7, 2018.

[14] G. Zhang and L.-T. Hsu, "Performance assessment of the gnss diffraction models in urban areas," *NAVIGATION*, pp. 1–21, 2021, ISSN: 0028-1522. DOI: `https://doi.org/10.1002/navi.417`.

[15] P. J. Huber and E. M. Ronchetti, *Robust Statistics* (Wiley Series in Probability and Statistics). John Wiley & Sons, 2009, ISBN: 9780470129906. DOI: `10.1002/9780470434697`.

[16] P. D. Groves, *Principles of GNSS, inertial, and multisensor integrated navigation systems, Second Edition*, 2nd. Artech House, 2013, ISBN: 1608070050.

[17] W. Wen, T. Pfeifer, X. Bai, and L.-T. Hsu, "Factor graph optimization for gnss/ins integration: A comparison with the extended kalman filter," *NAVIGATION*, vol. 68, no. 2, pp. 315–331, 2021. DOI: `https://doi.org/10.1002/navi.421`.

[18] R. Yozevitch and B. B. Moshe, "A robust shadow matching algorithm for gnss positioning," *Navigation: Journal of The Institute of Navigation*, vol. 62, no. 2, pp. 95–109, 2015, ISSN: 0028-1522. DOI: `10.1002/navi.85`. [Online]. Available: `https://doi.org/10.1002/navi.85`.

[19] T. Suzuki, "Integration of gnss positioning and 3d map using particle filter," in *Proceedings of the 29th International Technical Meeting of the Satellite Division of The Institute of Navigation (ION GNSS+ 2016)*, pp. 1296–1304. DOI: `https://doi.org/10.33012/2016.14857`.

[20] Q. Zhong and P. D. Groves, “Multi-epoch 3d-mapping-aided positioning using bayesian filtering techniques,” *NAVIGATION*, vol. 69, 2022. DOI: `https://doi.org/10.33012/navi.515`.

[21] W. Wen, X. Bai, Y. C. Kan, and L. Hsu, “Tightly coupled gnss/ins integration via factor graph and aided by fish-eye camera,” *IEEE Transactions on Vehicular Technology*, vol. 68, no. 11, pp. 10 651–10 662, 2019, ISSN: 1939-9359. DOI: `10.1109/TVT.2019.2944680`.

[22] W. Wen and L.-T. Hsu, “Towards robust gnss positioning and real-time kinematic using factor graph optimization,” in *2021 IEEE International Conference on Robotics and Automation (ICRA)*, pp. 5884–5890. DOI: `10.1109/ICRA48506.2021.9562037`.

[23] G. Zhang, H.-F. Ng, W. Wen, and L.-T. Hsu, “3d mapping database aided gnss based collaborative positioning using factor graph optimization,” *IEEE Transactions on Intelligent Transportation Systems*, vol. 22, no. 10, pp. 6175–6187, 2021, ISSN: 1558-0016. DOI: `10.1109/TITS.2020.2988531`.

[24] G. Xu, *GPS Theory, Algorithms and Applications*, 2nd ed. Heidelberg, Berlin: Springer-Verlag, 2007, p. 340. DOI: `https://doi.org/10.1007/978-3-540-72715-6`.

[25] R. B. Langley, “Rtk gps,” *GPS World*, vol. 9, no. 9, pp. 70–76, 1998.

[26] P. J. G. Teunissen and A. Khodabandeh, “Review and principles of ppp-rtk methods,” *Journal of Geodesy*, vol. 89, no. 3, pp. 217–240, 2015, ISSN: 0949-7714.

[27] X. Li, M. Ge, X. Dai, *et al.*, "Accuracy and reliability of multi-gnss real-time precise positioning: Gps, glonass, beidou, and galileo," *Journal of Geodesy*, vol. 89, no. 6, pp. 607–635, 2015, ISSN: 1432-1394. DOI: `10.1007/s00190-015-0802-8`. [Online]. Available: `https://doi.org/10.1007/s00190-015-0802-8`.

[28] M. Deo and A. El-Mowafy, "A method for precise point positioning with integer ambiguity resolution using triple-frequency gnss data," *Measurement Science and Technology*, vol. 30, no. 6, p. 065 009, 2019, ISSN: 0957-0233 1361-6501. DOI: `10.1088/1361-6501/ab0945`. [Online]. Available: `http://dx.doi.org/10.1088/1361-6501/ab0945`.

[29] J. Geng, J. Guo, H. Chang, and X. Li, "Toward global instantaneous decimeter-level positioning using tightly coupled multi-constellation and multi-frequency gnss," *Journal of Geodesy*, vol. 93, no. 7, pp. 977–991, 2019, ISSN: 1432-1394. DOI: `10.1007/s00190-018-1219-y`. [Online]. Available: `https://doi.org/10.1007/s00190-018-1219-y`.

[30] T. Suzuki and N. Kubo, "N-los gnss signal detection using fish-eye camera for vehicle navigation in urban environments," *27th International Technical Meeting of the Satellite Division of the Institute of Navigation, ION GNSS 2014*, vol. 3, pp. 1897–1906, 2014.

[31] J. Moreau, S. Ambellouis, and Y. Ruichek, "Fisheye-based method for gps localization improvement in unknown semi-obstructed areas," *Sensors*, vol. 17, no. 1, p. 119, 2017. DOI: `10.3390/s17010119`.

[32] W. Wen, G. Zhang, and L. Hsu, "Exclusion of gnss nlos receptions caused by dynamic objects in heavy traffic urban scenarios using real-time 3d

point cloud: An approach without 3d maps," in *2018 IEEE/ION Position, Location and Navigation Symposium (PLANS)*, pp. 158–165, ISBN: 2153-3598. DOI: `10.1109/PLANS.2018.8373377`.

[33] W. Wen, G. Zhang, and L.-T. Hsu, "Correcting nlos by 3d lidar and building height to improve gnss single point positioning," *NAVIGATION, Journal of the Institute of Navigation*, vol. 66, pp. 705–718, 2019. DOI: `10.1002/navi.335`.

[34] P. D. Groves and Z. Jiang, "Height aiding, c/n0 weighting and consistency checking for gnss nlos and multipath mitigation in urban areas," *Journal of Navigation*, vol. 66, no. 5, pp. 653–669, 2013, ISSN: 0373-4633. DOI: `10.1017/S0373463313000350`. [Online]. Available: `https://www.cambridge.org/core/article/height-aiding-cn0-weighting-and-consistency-checking-for-gnss-nlos-and-multipath-mitigation-in-urban-areas/AD1F8EFE7138F75114175AB26193D8FA`.

[35] L.-T. Hsu, H. Tokura, N. Kubo, Y. Gu, and S. Kamijo, "Multiple faulty gnss measurement exclusion based on consistency check in urban canyons," *IEEE Sensors Journal*, vol. 17, no. 6, pp. 1909–1917, 2017, ISSN: 1530-437X. DOI: `10.1109/JSEN.2017.2654359`.

[36] P. Crosta, P. Zoccarato, R. Lucas, and G. D. Pasquale, "Dual frequency mass-market chips: Test results and ways to optimize pvt performance," *Proceedings of the 31st International Technical Meeting of the Satellite Division of The Institute of Navigation (ION GNSS+ 2018)*, pp. 323–333, 2018. DOI: `https://doi.org/10.33012/2018.15882`.

[37] *Navstar gps space segment/ user segment l5 interfaces (is-gps-705g)*, Web Page, 2020. [Online]. Available: `https://www.gps.gov/technical/icwg/IS-GPS-705G.pdf`.

[38] *Quasi-zenith satellite system interface specification satellite positioning, navigation and timing service (is-qzss-pnt-004)*, Web Page, 2021. [Online]. Available: `https://qzss.go.jp/en/technical/download/pdf/ps-is-qzss/is-qzss-pnt-004.pdf?t=1620986285018`.

[39] *Galileo - open service - signal in space interface control document (os sis icd v2.0)*, Web Page, 2021. [Online]. Available: `https://www.gsc-europa.eu/sites/default/files/sites/all/files/Galileo_OS_SIS_ICD_v2.0.pdf`.

[40] Web Page, 2017. [Online]. Available: `http://en.beidou.gov.cn/SYSTEMS/Officialdocument/201806/P020180608525870555377.pdf`.

[41] Q. Zhang, Z. Chen, F. Rong, and Y. Cui, “Preliminary availability assessment of multi-gnss: A global scale analysis,” *IEEE Access*, vol. 7, pp. 146 813–146 820, 2019, ISSN: 2169-3536. DOI: `10.1109/ACCESS.2019.2946221`.

[42] J. Leclère, J. Landry René, and C. Botteron, “Comparison of l1 and l5 bands gnss signals acquisition,” *Sensors (Basel, Switzerland)*, vol. 18, no. 9, p. 2779, 2018, ISSN: 1424-8220. DOI: `10.3390/s18092779`. [Online]. Available: `https://www.ncbi.nlm.nih.gov/pubmed/30142964%20https://www.ncbi.nlm.nih.gov/pmc/articles/PMC6165328/`.

[43] A. J. V. Dierendonck, “Gps receivers,” in *Global Positioning System: Theory and Applications, Volume I* (Progress in Astronautics and Aeronautics), Progress in Astronautics and Aeronautics. American Institute of Aeronautics and Astronautics, 1996, pp. 329–407, ISBN: 978-1-56347-106-3. DOI: `doi:10.2514/5.9781600866388.0329.0407`. [Online]. Available: `https://doi.org/10.2514/5.9781600866388.0329.0407`.

[44] S. Tabibi, F. G. Nievinski, T. van Dam, and J. F. Monico, “Assessment of modernized gps l5 snr for ground-based multipath reflectometry applications,” *Advances in Space Research*, vol. 55, no. 4, pp. 1104–1116, 2015, ISSN: 0273-1177. DOI: `https://doi.org/10.1016/j.asr.2014.11.019`. [Online]. Available: `https://www.sciencedirect.com/science/article/pii/S0273117714007224`.

[45] A. Leick, L. Rapoport, and D. Tatarnikov, *GPS satellite surveying*. New York, N.Y.: John Wiley & Sons, 2015, ISBN: 0471059307 9780471059301.

[46] H. V. D. MAREL and P. F. D. BAKKER, “Single- versus dual-frequency precise point positioning,” *InsideGNSS*, 2012.

[47] B. Li, Y. Shen, and X. Zhang, “Three frequency gnss navigation prospect demonstrated with semi-simulated data,” *Advances in Space Research*, vol. 51, no. 7, pp. 1175–1185, 2013, ISSN: 0273-1177. DOI: `https://doi.org/10.1016/j.asr.2012.10.031`. [Online]. Available: `https://www.sciencedirect.com/science/article/pii/S0273117712006825`.

[48] A. El-Mowafy, “Advanced receiver autonomous integrity monitoring using triple frequency data with a focus on treatment of biases,” *Advances in*

Space Research, vol. 59, no. 8, pp. 2148–2157, 2017, ISSN: 0273-1177. DOI: `https://doi.org/10.1016/j.asr.2017.01.037`. [Online]. Available: `https://www.sciencedirect.com/science/article/pii/S0273117717300844`.

[49] P. R. R. Strode and P. D. Groves, "Gnss multipath detection using three-frequency signal-to-noise measurements," *GPS Solutions*, vol. 20, no. 3, pp. 399–412, 2016, ISSN: 1521-1886. DOI: `10.1007/s10291-015-0449-1`. [Online]. Available: `https://doi.org/10.1007/s10291-015-0449-1`.

[50] H.-F. Ng, G. Zhang, K.-Y. Yang, S.-X. Yang, and L.-T. Hsu, "Improved weighting scheme using consumer-level gnss l5/e5a/b2a pseudorange measurements in the urban area," *Advances in Space Research*, vol. 66, no. 7, pp. 1647–1658, 2020, ISSN: 0273-1177. DOI: `https://doi.org/10.1016/j.asr.2020.06.002`. [Online]. Available: `http://www.sciencedirect.com/science/article/pii/S027311772030404X`.

[51] J. F. Zumberge, M. B. Heflin, D. C. Jefferson, M. M. Watkins, and F. H. Webb, "Precise point positioning for the efficient and robust analysis of gps data from large networks," *Journal of Geophysical Research: Solid Earth*, vol. 102, no. B3, pp. 5005–5017, 1997. DOI: `https://doi.org/10.1029/96JB03860`. eprint: `https://agupubs.onlinelibrary.wiley.com/doi/pdf/10.1029/96JB03860`. [Online]. Available: `https://agupubs.onlinelibrary.wiley.com/doi/abs/10.1029/96JB03860`.

[52] M. Deo and A. El-Mowafy, “Triple-frequency gnss models for ppp with float ambiguity estimation: Performance comparison using gps,” *Survey Review*, vol. 50, no. 360, pp. 249–261, 2018. DOI: `10.1080/00396265.2016.1263179`.

[53] F. Guo, X. Zhang, J. Wang, and X. Ren, “Modeling and assessment of triple-frequency bds precise point positioning,” *Journal of Geodesy*, vol. 90, no. 11, pp. 1223–1235, 2016, ISSN: 1432-1394. DOI: `10.1007/s00190-016-0920-y`. [Online]. Available: `https://doi.org/10.1007/s00190-016-0920-y`.

[54] J. J. Spilker Jr and A. J. Van Dierendonck, “Proposed new l5 civil gps codes,” *Navigation*, vol. 48, no. 3, pp. 135–143, 2001, ISSN: 0028-1522. DOI: `10.1002/j.2161-4296.2001.tb00237.x`. [Online]. Available: `https://doi.org/10.1002/j.2161-4296.2001.tb00237.x`.

[55] H. Qin, P. Liu, L. Cong, and W. Ji, “Triple-frequency combining observation models and performance in precise point positioning using real bds data,” *IEEE Access*, vol. 7, pp. 69 826–69 836, 2019. DOI: `10.1109/ACCESS.2019.2918987`.

[56] X. Luo, S. Li, and H. Xu, “Results of real-time kinematic positioning based on real gps l5 data,” *IEEE Geoscience and Remote Sensing Letters*, vol. 13, no. 8, pp. 1193–1197, 2016. DOI: `10.1109/LGRS.2016.2575062`.

[57] H. K. L. Department, Government Document, n.d. [Online]. Available: `https://www.landsd.gov.hk/en/spatial-data/open-data.html`.

[58] S. Ji, W. Chen, X. Ding, Y. Chen, C. Zhao, and C. Hu, “Potential benefits of gps/glonass/galileo integration in an urban canyon–hong kong,” *The Journal of Navigation*, vol. 63, no. 4, pp. 681–693, 2010.

[59] D. of City Planning, Web Page. [Online]. Available: `https://www1.nyc.gov/site/planning/data-maps/open-data/dwn-nyc-3d-model-download.page`.

[60] Y. Suh and R. Shibasaki, “Evaluation of satellite-based navigation services in complex urban environments using a three-dimensional gis,” *IEICE transactions on communications*, vol. 90, no. 7, pp. 1816–1825, 2007.

[61] A. Steed, “Supporting mobile applications with real-time visualisation of gps availability,” in *International Conference on Mobile Human-Computer Interaction*, 2004.

[62] F. Kleijer, D. Odijk, and E. Verbree, “Prediction of gnss availability and accuracy in urban environments case study schiphol airport,” *Location based services and telecartography II: from sensor fusion to context models*, pp. 387–406, 2009.

[63] C. C. J. M. Tiberius and E. Verbree, “Gnss positioning accuracy and availability within location based services: The advantages of combined gps-galileo positioning,” *2nd ESA/Estec workshop on Satellite Navigation User Equipment Technologies, GS Granados (Ed), ESA publications division, Noordwijk*, pp. 1–12, 2004.

[64] H.-I. Kim, K.-D. Park, and H.-S. Lee, “Development and validation of an integrated gnss simulator using 3d spatial information,” *Journal of the Ko-*

rean Society of Surveying, Geodesy, Photogrammetry and Cartography, vol. 27, no. 6, pp. 659–667, 2009.

[65] G. Sohn and I. Dowman, "Data fusion of high-resolution satellite imagery and lidar data for automatic building extraction," *ISPRS Journal of Photogrammetry and Remote Sensing*, vol. 62, no. 1, pp. 43–63, 2007, ISSN: 0924-2716. DOI: `10.1016/j.isprsjprs.2007.01.001`.

[66] R. Wang, "3d building modeling using images and lidar: A review," *International Journal of Image and Data Fusion*, vol. 4, no. 4, pp. 273–292, 2013, ISSN: 1947-9832. DOI: `10.1080/19479832.2013.811124`.

[67] M. Haklay and P. Weber, "Openstreetmap: User-generated street maps," *IEEE Pervasive Computing*, vol. 7, no. 4, pp. 12–18, 2008. DOI: `10.1109/MPRV.2008.80`.

[68] Survey and H. K. L. D. Mapping Office, *Explanatory notes on geodetic datums in hong kong*, Government Document, 1995.

[69] M. Obst, S. Bauer, and G. Wanielik, "Urban multipath detection and mitigation with dynamic 3d maps for reliable land vehicle localization," in *Proceedings of the 2012 IEEE/ION Position, Location and Navigation Symposium*, 2012, pp. 685–691, ISBN: 2153-3598. DOI: `10.1109/PLANS.2012.6236944`.

[70] S. Peyraud, D. Bétaille, S. Renault, *et al.*, "About non-line-of-sight satellite detection and exclusion in a 3d map-aided localization algorithm," *Sensors*, vol. 13, no. 1, pp. 829–847, 2013. DOI: `10.3390/s130100829`.

[71] L. Wang, P. D. Groves, and M. K. Ziebart, "Multi-constellation gnss performance evaluation for urban canyons using large virtual reality city models," *Journal of Navigation*, vol. 65, no. 3, pp. 459–476, 2012, ISSN: 0373-4633. DOI: `10.1017/S0373463312000082`. [Online]. Available: `https://www.cambridge.org/core/article/multiconstellation-gnss-performance-evaluation-for-urban-canyons-using-large-virtual-reality-city-models/7DCC8FC0C2F81222413E9A69FE409C24`.

[72] R. Sun, L.-T. Hsu, D. Xue, G. Zhang, and W. Y. Ochieng, "Gps signal reception classification using adaptive neuro-fuzzy inference system," *Journal of Navigation*, vol. 72, no. 3, pp. 685–701, 2019, ISSN: 0373-4633. DOI: `10.1017/S0373463318000899`. [Online]. Available: `https://www.cambridge.org/core/article/gps-signal-reception-classification-using-adaptive-neurofuzzy-inference-system/77EB454066500EA568F5F5E95C095152`.

[73] H.-F. Ng, G. Zhang, and L.-T. Hsu, "Robust gnss shadow matching for smartphones in urban canyons," *IEEE Sensors Journal*, vol. 21, no. 16, pp. 18 307–18 317, 2021, ISSN: 1558-1748. DOI: `10.1109/JSEN.2021.3083801`.

[74] T. Suzuki and N. Kubo, "Gnss positioning with multipath simulation using 3d surface model in urban canyon," *Proceedings of the 25th International Technical Meeting of the Satellite Division of The Institute of Navigation (ION GNSS 2012)*, pp. 438–447, 2012.

[75] T. Suzuki and N. Kubo, "Correcting gnss multipath errors using a 3d surface model and particle filter," *Proceedings of the 26th International Technical Meeting of the Satellite Division of The Institute of Navigation (ION GNSS+ 2013)*, pp. 1583–1595, 2013.

[76] X. Liu, S. Nath, and R. Govindan, "Gnome: A practical approach to nlos mitigation for gps positioning in smartphones," in *Proceedings of the 16th Annual International Conference on Mobile Systems, Applications, and Services*, Association for Computing Machinery, pp. 163–177. DOI: `10.1145/3210240.3210343`. [Online]. Available: `https://doi.org/10.1145/3210240.3210343`.

[77] L. Xu, N. I. Ziedan, X. Niu, and W. Guo, "Correlation acceleration in gnss software receivers using a cuda-enabled gpu," *GPS Solutions*, vol. 21, no. 1, pp. 225–236, 2017, ISSN: 1521-1886. DOI: `10.1007/s10291-016-0516-2`. [Online]. Available: `https://doi.org/10.1007/s10291-016-0516-2`.

[78] P. Gegout, P. Oberlé, C. Desjardins, J. Moyard, and P.-M. Brunet, "Ray-tracing of gnss signal through the atmosphere powered by cuda, hmpp and gpus technologies," *IEEE Journal of Selected Topics in Applied Earth Observations and Remote Sensing*, vol. 7, no. 5, pp. 1592–1602, 2014.

[79] H.-F. Ng, G. Zhang, Y. Luo, and L.-T. Hsu, "Urban positioning: 3d mapping-aided gnss using dual-frequency pseudorange measurements from smartphones," *NAVIGATION, Journal of the Institute of Navigation*, vol. 68, no. 4, pp. 727–749, 2021, ISSN: 0028-1522. DOI: `10.1002/navi.448`. [Online]. Available: `https://doi.org/10.1002/navi.448`.

[80] G. Zhang, W. Wen, B. Xu, and L.-T. Hsu, "Extending shadow matching to tightly-coupled gnss/ins integration system," *IEEE Transactions on Vehicular Technology*, vol. 69, no. 5, pp. 4979–4991, 2020, ISSN: 0018-9545. DOI: `10.1109/TVT.2020.2981093`.

[81] N. I. Ziedan, "Optimized position estimation in multipath environments using machine learning," in *Proceedings of the 34th International Technical Meeting of the Satellite Division of The Institute of Navigation (ION GNSS+ 2021)*, pp. 3437–3451. DOI: `https://doi.org/10.33012/2021.17880`.

[82] R. Furukawa, N. Kubo, and A. El-Mowafy, "Prediction of rtk-gnss performance in urban environments using a 3d model and continuous los method," in *Proceedings of the 2020 International Technical Meeting of The Institute of Navigation*, pp. 763–771.

[83] R. Furukawa, N. Kubo, and A. El-Mowafy, "Verification of gnss multipath and positioning in urban areas using 3d maps," *IEICE Communications Express*, vol. advpub, 2020. DOI: `10.1587/comex.2020XBL0096`.

[84] H.-F. Ng and L.-T. Hsu, "3d mapping database-aided gnss rtk and its assessments in urban canyons," *IEEE Transactions on Aerospace and Electronic Systems*, vol. 57, no. 5, pp. 3150–3166, 2021, ISSN: 1557-9603. DOI: `10.1109/TAES.2021.3069271`.

[85] F. Zimmermann, C. Eling, L. Klingbeil, and H. Kuhlmann, "Precise positioning of uavs - dealing with challenging rtk-gps measurement conditions during automated uav flights," *ISPRS Annals of Photogrammetry, Remote Sensing and Spatial Information Sciences*, vol. 42W3, p. 95, 2017. DOI:

`10.5194/isprs-annals-IV-2-W3-95-2017`. [Online]. Available: `https://ui.adsabs.harvard.edu/abs/2017ISPAn42W3...95Z`.

[86] H.-F. Ng, G. Zhang, and L.-T. Hsu, "Gnss nlos pseudorange correction based on skymask for smartphone applications," *Proceedings of the 32nd International Technical Meeting of the Satellite Division of The Institute of Navigation (ION GNSS+ 2019)*, pp. 109–119, 2019. DOI: `10.33012/2019.17121`.

[87] P. D. Groves, "Shadow matching: A new gnss positioning technique for urban canyons," *Journal of Navigation*, vol. 64, no. 3, pp. 417–430, 2011, ISSN: 0373-4633. DOI: `10.1017/S0373463311000087`.

[88] J. A. Klobuchar, "Ionospheric time-delay algorithm for single-frequency gps users," *IEEE Transactions on Aerospace and Electronic Systems*, vol. AES-23, no. 3, pp. 325–331, 1987, ISSN: 0018-9251. DOI: `10.1109/TAES.1987.310829`.

[89] J. Saastamoinen, "Contributions to the theory of atmospheric refraction," *Bulletin Géodésique (1946-1975)*, vol. 107, no. 1, pp. 13–34, 1973, ISSN: 0007-4632. DOI: `10.1007/BF02522083`. [Online]. Available: `https://doi.org/10.1007/BF02522083`.

[90] T. Walter, J. Blanch, R. Eric Phelts, and P. Enge, "Evolving waas to serve l1/l5 users," *NAVIGATION*, vol. 59, no. 4, pp. 317–327, 2012, ISSN: 0028-1522. DOI: `10.1002/navi.21`. [Online]. Available: `https://doi.org/10.1002/navi.21`.

[91] E. Realini and M. Reguzzoni, "Gogps: Open source software for enhancing the accuracy of low-cost receivers by single-frequency relative kine-

matic positioning," *Measurement Science and technology*, vol. 24, no. 11, p. 115 010, 2013, ISSN: 0957-0233. DOI: `10.1088/0957-0233/24/11/115010`.

[92] L.-T. Hsu, F. Huang, H.-F. Ng, *et al.*, "Hong kong urbannav: An open-source multisensory dataset for benchmarking urban navigation algorithms," *NAVIGATION: Journal of the Institute of Navigation*, vol. 20, no. 4, 2023. DOI: `doi.org/10.33012/navi.602`.

[93] S. Kennedy, J. Hamilton, and H. Martell, "Architecture and system performance of span -novatel's gps/ins solution," in *2006 IEEE/ION Position, Location, And Navigation Symposium*, 2006, pp. 266–. DOI: `10.1109/PLANS.2006.1650612`.

[94] T. Takasu, "Rtklib: Open source program package for rtk-gps," in *FOSS4G 2009 Tokyo*, 2009.

[95] M. Meurer, S. Erker, S. Tholert, O. Montenbruck, A. Hauschild, and R. B. Langley, "Gps l5 first light: A preliminary analysis of svn49's demonstration signal.(innovation)," *GPS World*, vol. 20, no. 6, p. 49, 2009, ISSN: 1048-5104.

[96] E. S. Lohan and K. Borre, "Accuracy limits in multi-gnss," *IEEE Transactions on Aerospace and Electronic Systems*, vol. 52, no. 5, pp. 2477–2494, 2016, ISSN: 0018-9251. DOI: `10.1109/TAES.2016.150241`.

[97] B. Xu, Q. Jia, Y. Luo, and L. T. Hsu, "Intelligent gps l1 los/multipath/nlos classifiers based on correlator-, rinex- and nmea-level measurements," *Remote Sensing*, vol. 11, no. 16, p. 1851, 2019, ISSN: 20724292. DOI: `10.3390/rs11161851`.

[98] W. Li, X. Cui, and M. Lu, "A robust graph optimization realization of tightly coupled gnss/ins integrated navigation system for urban vehicles," *Tsinghua Science and Technology*, vol. 23, no. 6, pp. 724–732, 2018, ISSN: 1007-0214. DOI: `10.26599/TST.2018.9010078`.

[99] S. Agarwal and K. Mierle, "Ceres solver: Tutorial & reference," *Google Inc.*, vol. 2, no. 72, p. 8, 2012.

[100] T. Suzuki, K. Matsuo, and Y. Amano, "Rotating gnss antennas: Simultaneous los and nlos multipath mitigation," *GPS Solutions*, vol. 24, no. 3, p. 86, 2020, ISSN: 1521-1886. DOI: `10.1007/s10291-020-01006-w`. [Online]. Available: `https://doi.org/10.1007/s10291-020-01006-w`.

[101] N. I. Ziedan, "Urban positioning accuracy enhancement utilizing 3d buildings model and accelerated ray tracing algorithm," *Proceedings of the 30th International Technical Meeting of The Satellite Division of the Institute of Navigation (ION GNSS+ 2017)*, pp. 3253–3268, 2017. DOI: `10.33012/2017.15366`.

[102] R. Adams and L. Bischof, "Seeded region growing," *IEEE Transactions on pattern analysis and machine intelligence*, vol. 16, pp. 641–647, 1994.

[103] G. Matheron, "Principles of geostatistics," *Economic Geology*, vol. 58, no. 8, pp. 1246–1266, 1963, ISSN: 0361-0128. DOI: `10.2113/gsecongeo.58.8.1246`. [Online]. Available: `https://doi.org/10.2113/gsecongeo.58.8.1246`.

[104] H. Wackernagel, *Multivariate geostatistics: An introduction with applications (3rd ed.)* Berlin, Heidelberg: Springer, 2003.

[105] R. Webster and M. Oliver, *Geostatistics for environmental scientists*. Wiley, 2007, ISBN: 9780470517260.

[106] B. Hofmann-Wellenhof, H. Lichtenegger, and E. Wasle, *GNSS–global navigation satellite systems: GPS, GLONASS, Galileo, and more*. Springer Science & Business Media, 2007, ISBN: 3211730176.

[107] H.-F. Ng, L.-T. Hsu, M. J. L. Lee, *et al.*, "Real-time loosely coupled 3dma gnss/doppler measurements integration using a graph optimization and its performance assessments in urban canyons of new york," *Sensors*, vol. 22, no. 17, p. 6533, 2022, ISSN: 1424-8220. DOI: `https://doi.org/10.3390/s22176533`. [Online]. Available: `https://www.mdpi.com/1424-8220/22/17/6533`.

[108] H.-F. Ng, "Multi-epoch kriging-based 3d mapping aided gnss using factor graph optimization," in *Proceedings of the 35th International Technical Meeting of the Satellite Division of The Institute of Navigation (ION GNSS+ 2022)*, 2022, pp. 1706–1720. DOI: `https://doi.org/10.33012/2022.18497`.

[109] H.-F. Ng, L.-T. Hsu, and G. Zhang, *Multi-epoch kriging-based 3d mapping-aided gnss and doppler measurement fusion using factor graph optimization*, Dataset, 2023. DOI: `https://doi.org/10.33012/navi.617`.